Passive Ammonia SCR and Filtration Modeling for Fuel-neutral Engine Aftertreatment Systems

by

Jian Gong

A dissertation submitted in partial fulfillment of the requirements for the degree of

Doctor of Philosophy

(Mechanical Engineering)

at the

UNIVERSITY OF WISCONSIN-MADISON

2014

Date of final oral examination: 5/19/2014

The dissertation is approved by the following members of the Final Oral Committee:
Rutland, Christopher J., Professor, Mechanical Engineering
Reitz, Rolf, Professor, Mechanical Engineering
Ghandhi, Jaal, Professor, Mechanical Engineering
Rothamer, David, Associate Professor, Mechanical Engineering
Graham, Michael, Professor, Mechanical Engineering

www.manaraa.com

UMI Number: 3624280

All rights reserved

INFORMATION TO ALL USERS
The quality of this reproduction is dependent upon the quality of the copy submitted.

In the unlikely event that the author did not send a complete manuscript
and there are missing pages, these will be noted. Also, if material had to be removed,
a note will indicate the deletion.

UMI 3624280

Published by ProQuest LLC (2014). Copyright in the Dissertation held by the Author.

Microform Edition © ProQuest LLC.
All rights reserved. This work is protected against
unauthorized copying under Title 17, United States Code

ProQuest LLC.
789 East Eisenhower Parkway
P.O. Box 1346
Ann Arbor, MI 48106 - 1346

www.manaraa.com

Abstract

Passive ammonia SCR system models including a TWC model and a SCR model are developed. The TWC kinetic model is developed based on the engine dynamometer data collected on a lean burn spark ignition direct injection (SIDI) engine. Ammonia and nitrous oxide formation kinetics are included in the TWC model. A global SCR model including ammonia storage, ammonia oxidation, NO oxidation, three SCR reactions (standard SCR, fast SCR and NO_2 SCR) and N_2O formation is developed on a Cu-chabazite (CHA) NH_3-SCR catalyst. An improve ammonia storage model is developed to model the ammonia storage at different temperatures. Experimental data collected on a flow bench SCR reactor based on a well-designed experimental SCR protocol at Oak Ridge National Lab (ORNL) are used for SCR model calibrations and validations. The TWC and SCR models are found to be able to predict the $DeNO_x$ performance over a wide range of engine exhaust conditions.

Motivated by modeling of gasoline particulate filters (GPFs), a PDF based heterogeneous multi-scale filtration (HMF) model is developed to calculate filtration efficiency of particulate filters. The HMF model overcomes the limitations of classic mean filtration models which rely on tuning of the mean collector size. The HMF model is validated on various scales of filter samples and is found to give better predictions of filtration efficiencies compared to the mean filtration model. A dynamic version of HMF model is developed as well to study the dynamic filtration process. Filtration experimental data from exhaust filtration analysis (EFA) system are used for model validations. The dynamic HMF model is found to be able to capture the dynamic filtration process. Finally, filtration characteristics of fuel neutral particulates are studied by using the dynamic HMF model. Particulate penetration length is found to be influenced by the interactions between the

www.manaraa.com

filter and particulates. The change of the filter structure and the shape of the particulate size distribution play important role on particulate filtration. It is found that the HMF model is a useful diagnostic tool for filtration investigation.

www.manaraa.com

Acknowledgement

There are many people I should appreciate since I have been at ERC for about six years. First, I would like to express sincere gratitude to my advisor Professor Christopher Rutland. Thanks for offering me this great opportunity working at ERC. His constant advice and deep insight inspired me throughout my work. He is patient and always supports me to do what I found is interesting. I also appreciate that he brought me into the aftertreatment modeling community through tele-conferences with industry and national labs. I learned a lot from the talent folks in the community.

I appreciate Professor David Foster and Professor David Rothamer for valuable and helpful discussion about the filtration work. I would also like to thank Professor Jaal Ghandhi, Professor Rolf Reitz and Professor Michael Graham for taking the time to be my committee members. I am very proud to have studied in the presence of such inspiring individuals who taught me combustion and transport fundamentals.

I would further like to thank General Motors for their funding support to this project. Special thanks to Kushal Narayanaswamy and Paul Najt for their guidance and advice. Thanks Craig Marriot and Yangbing Zeng offering me the summer internship opportunity at GM powertrain. Thanks to Todd Toops, James Parks, Stuart Daw, Vitaly Prikhodko, Zhiming Gao, Josh Pihl at ORNL for valuable discussions about the $DeNO_x$ modeling work during our monthly tele-conferences. I also appreciate Mark Stewart and Alla Zelenyuk-Imre at PNNL for their valuable insights on particulate filtration modeling.

Thanks to all the ERC students and fellows. Chi-Wei, Nitiya Animesh and Noah are very nice officemates and it is a pleasure to work with them and lean from them. Thanks Yangdongfang and

www.manaraa.com

previous student Soolyoul for valuable discussion of the DPF and SCR work. Thank Sandeep for his valuable inputs and daily discussion on the filtration modeling and EFA experiments. Also, thanks Stephen, Mitchell and Yizhou for taking the fuel-neutral particulates measurements to support the filtration work. I also would like to thank Josh Leach for his help to get through all the computer problems.

Finally, I would like to express my gratitude to my parents, Daoxin Gong and Piyan Wu, my young brother Jun Gong and my fiancé Mingwei Yuan, who have given me endless support and encouragement during my study at UW-Madison.

www.manaraa.com

Table of Contents

www.manaraa.com

www.manaraa.com

www.manaraa.com

List of Figures

www.manaraa.com

www.manaraa.com

www.manaraa.com

www.manaraa.com

www.manaraa.com

www.manaraa.com

www.manaraa.com

List of Tables

www.manaraa.com

Nomenclature

ABBREVIATION

CI	Compression ignition
SI	Spark ignition
SIDI	Spark ignition direct injection
EPA	Environmental protection agency
CRAB	California air resources board
LEV	Low emission vehicles
NMOG	Nonmethane organic gas
GHG	Greenhouse gas
PM	Particulate matter
PN	Particulate number
NO_x	Nitrogen oxides
CO	Carbon monoxide
HC	Total hydrocarbon
NH_3	Ammonia
N_2O	Nitrous oxide
FTP	Federal testing procedure
NEDC	New European driving cycle
TWC	Three way catalyst
LNT	Lean NO_x trap
SCR	Selective catalyst reduction
PASS	Passive ammonia SCR system
LH	Langmuir-Hinshelwood
GWP	Global warming potential
ORNL	Oak ridge national laboratory
PGM	Platinum group metal
OSC	Oxygen storage component
PDF	Probability density function

DEFINITIONS

T_g	Gas temperature [°C]
T_s	Catalyst surface temperature [°C]
k_s	Permeability of PM [m^2]
k_w	Permeability of wall [m^2]
w_s	Thickness of PM [m]
w_w	Thickness of wall [m]
ρ_i	Gas density [kg/m^3]
u_i	Gas velocity [m/s]
v_w	Wall velocity [m/s]
μ	Gas viscosity [kg/m/s]
f	Friction coefficient [-]
a	Channel side length [m]
k_0	Clean filter permeability [m^2]
k	Filter permeability [m^2]
ε_0	Clean filter porosity [-]
ε	Filter porosity [-]
β	Filter solidity [-]
d_{pore}	Clean filter pore diameter [m]
d_{c0}	Initial "unit collector" diameter [m]
d_c	"unit collector" diameter [m]
b	Diameter of the "unit cell" [m]
λ	Mean free path of the gas [m]
D_p	Particle diffusion coefficient [m^2/s]
Pe	Peclet number [-]
Kn	Knudsen number [-]
$m_{soot,collect}$	Mass of PM collected at a single "unit cell"[kg]
$\rho_{soot,w}$	Density of PM trapped inside the filter wall [kg/m^3]
V_{cell}	Volume of a computational cell[m^3]
V_{uc}	Volume of a "unit cell" [m^3]
N_{uc}	Number of "unit cell" in a computational cell [-]
E_D	Diffusion efficiency [-]
E_R	Interception efficiency [-]
E_t	Total collection efficiency [-]
Δy	Discretized length in y direction [m]
η_f	Total filtration efficiency [-]
p_1	Inlet channel pressure [Pa]
p_2	Outlet channel pressure [Pa]
Δp	Pressure drop across the filter wall [Pa]
C_i^g	Bulk gas concentration of species i [$mole/m^3$]

www.manaraa.com

C_i^s	Bulk surface concentration of species i [mole/m^3]
$k_{m,i}$	Mass transfer coefficient of species i [m/s]
A_e	Effective flow area [m^2]
h	Heat transfer coefficient [W/m^2-K]
$C_{p,g}$	Specific heat of exhaust gas [J/kg/K]
$C_{p,s}$	Specific heat of substrate[J/kg/K]
ρ_g	Density of exhaust gas [kg/m^3]
ρ_s	Density of substrate[kg/m^3]
k_s	Conductivity of substrate [W/m/K]
ΔH_i	Enthalpy change of reaction i [J]
Nu	Nussel number [-]
k_g	Conductivity of exhaust gas [W/m/K]
d_h	Hydrodynamic length [m]
Sh	Sherwood number [-]
$D_{g,i}$	Diffusivity of species i [m^2/s]
a_i	Active site density of catalyst [mole-site/m^3]
r_i	Specific reaction rate [mole/mole-site/s]
R_i	Total reaction rate [mole/m^3/s]
$f(G_i)$	Inhibition function [-]
θ_i	Surface coverage of catalyst [-]
c_i	Concentration of species i [mole/m^3]
α	Conversion rate of NH_3 or N_2O from NO_x [-]

www.manaraa.com

Chapter 1 - Introduction

1.1 Background

Lean-burn spark ignition direct injection (SIDI) gasoline engines have shown potential to significantly increase vehicle fuel economy and decrease CO_2 emissions by combining the positive qualities of compression ignition (CI) and spark-ignition (SI) engines. In the late 1990s, interest in lean gasoline engines is due to fuel economy improvement [1,2,3]. Better fuel economy is mainly achieved by lower throttling as well as higher compression ratios [4]. In early 2000s, a large focus is on diesel engine technology and development of lean aftertreatment systems, due to more stringent emission regulations on diesel engines [5,6,7]. As a fact that U.S. passenger car fleet is dominated by gasoline-fueled vehicles [8], in late 2000s, attention is brought about on lean-burn gasoline engines again due to their higher fuel efficiency, higher power output and lower CO_2 emission. By downsizing displacement, coupling a turbocharger and an advanced injection system, the fuel efficiency of gasoline engines can be further improved. Above all, lean operations offer the most significant benefits of fuel economy.

However, SIDI engines tend to make relatively higher nitrogen oxides (NO_x) and more PM than their PFI counterparts [9,10,11]. It was reported by Flynn et al. [12] that high product gas temperatures are required and relatively high NO_x production rates are the inevitable result under conditions of pressure and temperature in combustion engines. It is impossible to reduce NO_x production to very low levels if flame propagation at high pressures is involved, and it will be necessary to provide aftertreatment to reduce NO_x emissions to legislated levels. NO_x emission challenges present significant technological hurdle for SIDI engines. Particulate matter (PM) emissions may also be of concern with respect to particle number regulations.

www.manaraa.com

For light duty vehicles, SIDI engines are subjected to further worldwide tightening of the emission regulations specifically aiming at reducing NO_x and PM. The federal Tier 2 for NO_x emission is 70 mg/mile averaged at a full useful life (120,000 miles) and 10 mg/mile for PM (EPA, Emission Standards Reference Guide). California air resources board (CARB) finalized LEV III light-duty emission standards in 2012 with a 30 mg/mile fleet average NMOG+NO_x by 2025. The PM standards are tightened as well in LEV III from 10mg/mile on the FTP today to 3mg/mile phasing in 2017~2021 and 1mg/mile phasing in 2025~2028 [13]. The Euro V and VI regulation for NO_x is 96 mg/mile and for PM is 7.2 mg/mile [14]. Euro VI also uses the same particulate number (PN) limit (6E11 #/km) for gasoline direction injection engines, which is the same PN limit for diesel engines introduced in Euro 5 [15]. Moreover, a 163 g/mile CO_2 industry fleet average emission limit in 2025 was proposed by California's greenhouse gases (GHG) program with US EPA, nominally equivalent to a 54.5 mpg. Furthermore, 10mg/mile N_2O and 30mg/mile CH_4 caps over the FTP cycle have been started in 2012 [13].

On the other hand, depletion of petroleum resources and increasing automotive emissions have prompted the automotive industry to look towards new renewable sources of energy. Flexible fuel engines are important for exploiting the possibilities of using various types of alternative, renewable or synthetic fuels in the future that could reduce dependency on conventional fuels. Fuels like biodiesel, ethanol and methanol and their blends are being considered as future fuels for their comparable performance to diesel and gasoline, and their availability from natural sources [16]. It is necessary for fuel neutral engines, which have different combustion characteristics and levels of emissions [17] still meet the emissions standards.

www.manaraa.com

Another significant challenge for SIDI engine is to reduce the cost of aftertreatment devices, particularly the high amount of precious metals, which are currently needed to meet emission regulations under a wide range of operating conditions. Therefore, there is definitely a huge demand to develop high efficiency, fuel neutral, and cost-effective aftertreatment systems.

1.2 Motivation

The flexibility of the fuel posts a great challenge to develop a robust and effective aftertreatment system for fuel neutral engines. Engine exhaust conditions such as exhaust temperature, species concentrations, in particular the NO_x and PM emissions vary significantly among a specific engine that is running on different fuels. Most of $DeNO_x$ models were developed for a particular engine running with a particular fuel. Some of these models were validated at a few conditions under a flow bench reactor [18]. Some of them were validated directly at a few transient engine cycles e.g. FTP, US06, NEDC [19,20]. However, none of these models were validated among a large temperature window with various exhaust concentrations, which could be resulted from fuel neutral engines. There is a great opportunity to develop computational models for fuel neutral aftertreatment systems.

One of the major stumbling blocks in the commercial application of lean-burn SIDI engines is the lack of effective and affordable methods to remove NO_x. Since lean-burn engines operate with excess oxygen, it is hard to sufficiently reduce NO_x in the exhaust with the traditional three-way catalyst (TWC) used in stoichiometric gasoline engines. Therefore, additional $DeNO_x$ aftertreatment devices maybe needed to meet the NO_x emission regulations. Recently, a novel concept of the passive ammonia SCR system (PASS) coupled with a conventional three way catalyst (TWC) was demonstrated [21,22]. The close-coupled TWC functioned as an effective and

www.manaraa.com

a tunable NH_3 generator, which is able to produce NH_3 over a broad temperature window. However, the TWC in PASS needs to be optimized to have an optimal ammonia generation with minimum fuel penalty and maintain high efficiency for hydrocarbons and carbon monoxide oxidation reduction simultaneously. Similarly, a downstream NH_3-SCR should have NH_3 storage capability and NO_x conversion efficiency at a wide temperature range without NH_3 and NO_x slip. Engine control strategies need to be calibrated, for instant, lean and rich operation timing. The interactions among the engine, TWC and SCR system need to be well understood. There is a great challenge to minimize the fuel penalty by operating the $DeNO_x$ aftertreatment systems while meet the NO_x emission regulations.

Another challenge for SIDI engines is particulate matter reduction to meet tightening PM mass and number regulations. Diesel particulate filters (DPFs) have been successfully applied to diesel engines to remove particulate emissions. The collection of particles from diesel engines is primarily through surface or cake filtration, which occurs when particles are too large to penetrate into the porous media. However, small particles may penetrate into the filter wall. As a result, conventional particulate filters may break down below a certain size range, which also means the filtration efficiency would drop significantly. Therefore it is important to understand the fundamental filtration process for ultrafine particles.

Another concern is the impact of a filter on engine exhaust backpressure and the potential for higher CO_2 emissions, especially for high horsepower SIDI gasoline engines. There is a trade-off between higher filtration efficiency and lower pressure drop. In addition to providing sufficient filtration efficiency for particles to meet PM mass and number regulations, minimizing the pressure drop is equally a primary focus on filter development.

www.manaraa.com

1.3 Objective and outline

The long term objective of this project is to develop system level computational models capable of simulating engine and aftertreatment devices performance at transient conditions. In this study, the objective is to develop passive ammonia SCR and particulate filtration models for fuel neutral SIDI engines.

Rather than developing detailed microkinetic models for a particular $DeNO_x$ aftertreatment device, the focus is to develop a TWC and a SCR model with global kinetics, which has reasonable accuracy to predict catalyst performance over a wide range of engine exhaust conditions. In particular, understanding the kinetics of NH_3 formation in TWCs is another of interest. The capability of NH_3 generation in TWCs is the key to the success of the "PASS".

Another focus is development of fundamental filtration models for gasoline particulate filters (GPFs) on fuel neutral engines.

Once the aftertreatment models are developed and validated, they can be used to simulate the engine and aftertreatment system at transient conditions. The interactions among the engine and aftertreatment devices can be investigated. Eventually, the system models can be used to explore optimal engine control strategies and guild aftertreatment system design.

In this report, a literature review on engine aftertreatment modeling and discussion is given in Chapter 2, which includes NO_x reductions and particulate filtration. In Chapter 3, a TWC model and a LNT model are presented. Model validations using experimental data from an SIDI engine dynamometer as well as a flow bench reactor will be discussed. A Cu based SCR model will be developed in Chapter 5. Ammonia storage model as well as SCR kinetics are validated from a

www.manaraa.com

bench SCR reactor. A heterogeneous multi-scale filtration model is introduced in Chapter 5.. Finally, a summary of the present work and future research direction are given in Chapter 6.

www.manaraa.com

Chapter 2 - Literature Review

This chapter gives a literature review on aftertreatment devices for automotive engines including $DeNO_x$ catalysts and particulate filters. The $DeNO_x$ catalysts including TWCs, LNTs and SCRs are similar. Most of them are flow-through (channel flow) aftertreatment devices. However, the kinetics involved in these devices are different and are highly dependent on the catalysts. Particulate filters are wall flow aftertreatment devices. Flow distribution in the particulate filter is more important and resulted in a significant pressure drop.

2.1 Overview of $DeNO_x$ Catalyst

Lean-burn exhaust catalyst systems must typically provide extremely high NO_x conversion efficiency (>90%) over a wide temperature window (200-550°C) to be considered as potential aftertreatment candidates for vehicle applications. The reduction of NO_x at low temperatures (<200°C) is of particular importance for meeting stringent future emission standards.

NO_x can be removed from lean-burn exhaust mainly by three ways: (1) direct decomposition of NO; (2) NO_x storage and reduction (NSR); and (3) selective catalytic reduction (SCR). Direct decomposition of NO occurs without any reductant, however the decomposition reaction requires a relatively high activation energy [23].

NSR catalysts (also called lean NO_x traps, LNT) consist of a cordierite monolith washcoated with a porous alumina on which an alkali-earth oxide (e.g. BaO) and a noble metal (Pt) are deposited [24]. These catalysts operate alternatively under lean and rich conditions. During the lean period, when oxygen is in excess, some of NO is oxidized by platinum. A mixture of NO and NO_2 is

www.manaraa.com

adsorbed on Ba as various species (nitrite and nitrate). Before an unacceptable amount of NO_x slips through the catalyst, engine exhaust is switched to rich condition for a short period where the stored NO_x is released and reduced into N_2 over Pt. Different types of reducing agents such as HCs, CO and H_2 have been used in NSR catalyst studies [25], and H_2 has been found to be the most effective. Although LNT technology is regarded as the most practical technology for lean-burn gasoline engines, LNTs are weakly resistant to sulfur poisoning and thermal treatment and require high PGM loading [26].

SCR was originally developed for stationary emission sources, mainly power plants [26]. However, it soon turned out to be a promising technology for the NO_x removal in automobile applications as well. Similarly to LNT catalysts, SCR catalysts require reducing agents for NO_x reduction. Depending on the type of reductants, SCRs can be classified as HC-SCR and urea/NH_3 SCR. In HC-SCR the NO_x is reduced by a selective reaction with hydrocarbons [27]. On the other hand, urea/NH_3 SCR is the most commonly used aftertreatment system for lean burn engines [28]. There are many catalysts can be used as urea/NH_3 SCR. Non-noble metals like vanadium, copper, iron supported ZSM-5 and Beta zeolites, are among the most active catalysts for the urea/NH_3-SCR process [29,30,31].

2.1.1 Three way catalyst

The development of three-way catalysts (TWC) over the last 30 years has been a remarkable technical achievement. Current catalytic converters, based on the precious group metal (PGM) catalysts with various combinations of Pt, Pd and Rh as the active ingredients, provide a very high level of emission control for the removal of CO, NO_x and unburned hydrocarbons.

www.manaraa.com

The most widely used global kinetic model in $DeNO_x$ aftertreatment devices was developed by Voltz et al. with a Langmuir-Hinshelwood (LH) structure. They studied oxidation and reduction reactions under an exhaust gas containing CO, C_3H_6, NO, O_2, CO_2, H_2O and N_2 using a Pt/Al_2O_3 shell catalyst [32]. Many authors have used the same structure for TWC modeling [33, 34,35]. This structure is flexible and is easy to introduce competition between surface reactions by adding an empirical function in the denominator. Botas et al. used a full synthetic exhaust gas including CO_2 and H_2O and found that the oxidation of CO occurs at much lower temperature in the presence of water. The water gas shift (WGS) and steam reforming reactions were therefore added into their kinetic models [36].

Cerium is normally present in high quantities in the washcoat as a "promoter" and has multiple functions [37]: promoting the noble metal dispersion; stabilization of the washcoat layer; improvement of thermal resistance; promoting the water gas shift and steam reforming reactions; enhancement of precious metal catalytic activity, store and release oxygen under lean and rich conditions respectively. Koltskis et al. added oxygen storage to the kinetic models and simulated CO, NO and HC conversion for the NEDC driving cycle by fine tuning the parameters from transient measurements [38].

Nitrogen compounds formation in TWC systems was reported in the late 1990s [39,40]. However, it is recently that researchers pay more attention to nitrogen compounds (e.g. NH_3 and N_2O). It was found that NH_3 can be generated from a TWC or a LNT on board and used by SCR to reduce NO_x emissions [41,42].

Takei et al. [40] found that NH_3 formation exceeded the reduction of NO_x into N_2 at the temperature of 500°C in a metal-honeycomb-supported $Pt/Rh/Al_2O_3$ TWC catalyst in the

www.manaraa.com

$NO/H_2/Ar$ flow bench reactor system. NH_3 is produced in the TWC under certain conditions [43] when NO is reduced by H_2. However, the formed NH_3 can be oxidized by the NO and the O_2 present in a LNT catalyst [44,45]. Additionally, it has been observed that any source of O-atoms in the system (not necessarily limited to O-atoms from NO or O_2) can oxidize the formed NH_3 to N_2 or N_2O [46]. Moreover, NH_3 oxidation reactions with NO and O_2 are active at high temperatures [45,47]. Among the NH_3 formation and oxidation reactions, it has been observed that the formation reaction is much faster than the oxidation with NO [48]. DiGiulio et al. [49] recently found that the Pd-only TWC is a very efficient catalyst for NH_3 generation. Moreover, the Pd-only TWC shows a broad range of temperature and a very high efficiency (above 80%) for NH_3 generation, which is shown in Figure 2-1. Figure 2-2 shows that NH_3 generation is favored at higher temperatures with richer mixtures for the Pd-only TWC. However, N_2O formation was observed under lean conditions and varies with PGM content.

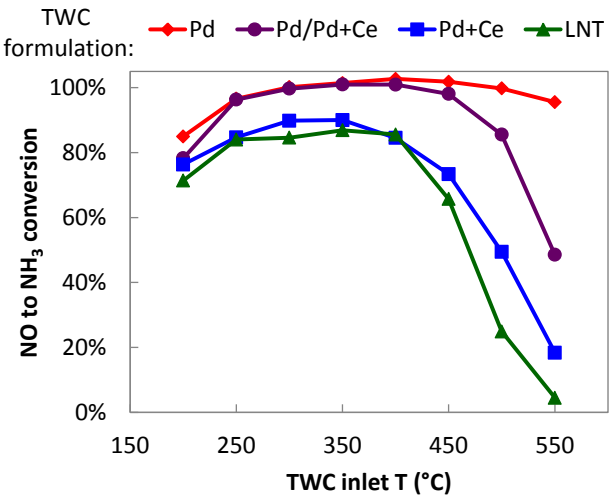

Figure 2-1: NH_3 generation from multiple upstream TWC catalyst formulations [49]

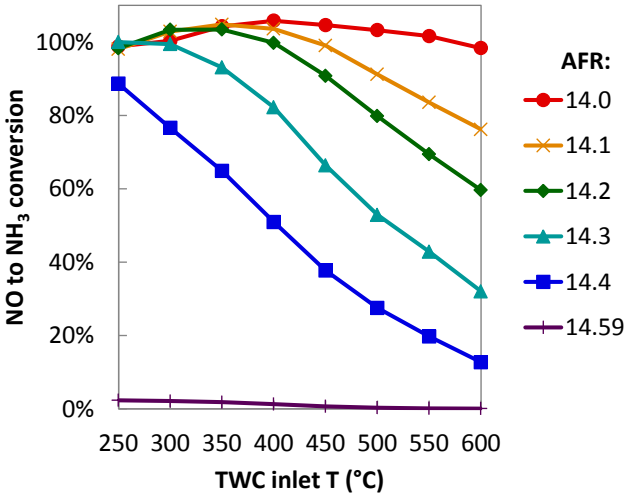

Figure 2-2: NH_3 generation over Pd only TWC at different AFRs [49]

N_2O was included in the recent Greenhouse Gas (GHG) regulations, which started counting N_2O as CO_2 equivalents as a greenhouse gas [13]. As a fact, N_2O has a long lifetime of approximately 120 years in the atmosphere and a Global Warming Potential (GWP) of 310 (310 times more

www.manaraa.com

powerful than CO_2 on heat trapping effects) (EPA website). N_2O was found to be predominately formed at low temperatures in various aftertreatment systems through incomplete reduction of NO_x by various reductants [44,50,51]. Odaka et al. found that N_2O formation was dominant (up to 200 ppm) at relatively low temperature in $NO/H_2/Ar$ and NO/CO/Ar systems. The amount of N_2O emission goes up with the noble metal quantity [39]. Cant et al. reported that rhodium, platinum and palladium differ significantly to produce N_2O from a simulated exhaust gas under near stoichiometric conditions [52]. The absolute amount is largest with rhodium but it falls off with temperature. Palladium is unique in that N_2O production persists through to 500°C. It was observed by Mejía-centeno et al. [53,54] that a large amount of N_2O (up to 700 ppm) was formed on a commercial Pd-only TWC during the light-off at low temperatures (200~400°C). The amount of N_2O was almost independent of the air-to-fuel ratio. O_2 promoted the formation of N_2O at high temperature (400~600°C).

2.1.2 Lean NO_x trap

One of the main differences for a LNT that differs from a TWC is the NO_x storage component. By introducing a NO_x storage materials (like Barium), NO_x can be stored during lean operating in a LNT.

The NO_x storage and reduction process during lean and rich cycles can be described by five steps [55]: (I) NO oxidation to NO_2; (II) NO_x (NO and NO_2) adsorption on the surface in the form of nitrites or nitrates; (III) reductants (e.g. H_2, CO, hydrocarbons) evolution when the exhaust is switched from lean to rich; (IV) NO_x release from the nitrite or nitrate sites; (V) NO_x reduction to N_2. The magnitude NO_x release (the peak NO_x) right after the lean to rich transition is determined by the NO_x storage capacity.

www.manaraa.com

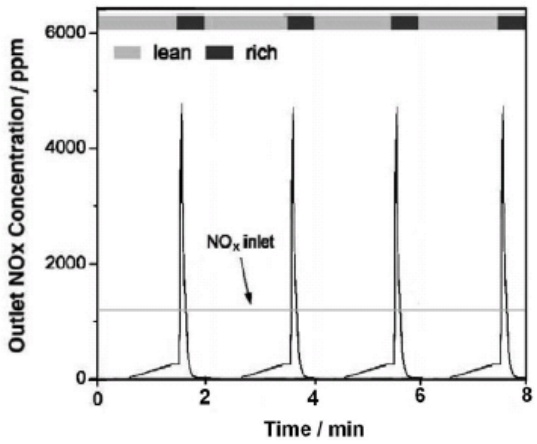

Figure 2-3: A representative NO_x breakthrough and release during the lean-rich cycles [55]

Kodama and Wong investigated NH_3 generation over a Ba based LNT catalyst in a flow bench reactor over a wide range of flow rates, temperatures to investigate the mechanism and appropriate conditions on ammonia generations [56]. It was found that NH_3 generation increases as reductant H_2 increases even though only a small fraction of H_2 was used in NH_3 production. O_2 concentration in the rich mixture has a significant impact on NH_3 generation, primarily due to the effects of O_2 on reductants oxidation and NH_3 oxidation. For a fixed cycle, addition of NO_x storage in the LNT significantly increases NH_3 formation compared to TWC [49]. Figure 2-4 shows the cycle averaged ratio of produced NH_3 and effluent NO_x using different catalysts.

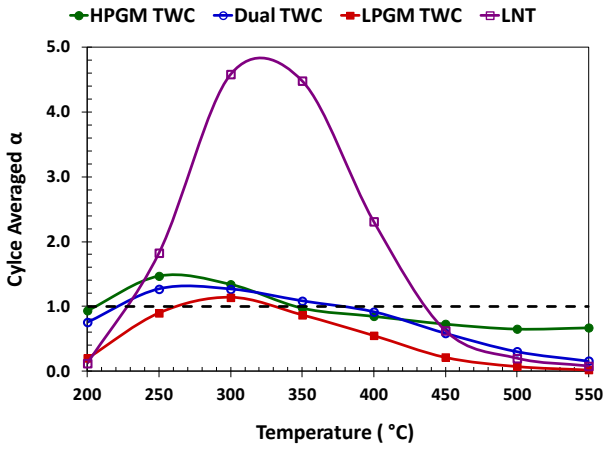

Figure 2-4: Cycle averaged α (NH_3/NO_x) for different TWC formulations and a LNT [49]

www.manaraa.com

Actually, most of the reaction kinetics studies on NH_3 formation and oxidation on PGM catalyst have been carried on a Lean NO_x Trap (LNT) system. There are detailed microkinetic models for a LNT system, which include NH_3 formation and oxidation [57,58]. Votsmeier et al. presented a rate mapping approach that can predict ammonia oxidation reactions [59].

One of the objectives in this project is to have a global kinetic model for NH_3 formation and oxidation. There are global kinetic models for LNT catalysts which include NH_3 formation and oxidation reactions but the reaction parameters were not mentioned [60,61,62] and the actual kinetic parameters are likely to be different between a commercial LNT catalyst and a commercial TWC. Olsson et al. found that adding NO_x storage material to the surface lowers the amount of PGM dispersion. This has the effect of lowering the overall conversion capabilities of the catalyst which suggests lower pre-exponential factors [63].

2.1.3 Selective catalytic reduction

One of the challenges for SCR model development is accurate description of ammonia storage. The accurate description of NH3 adsorption/desorption from the catalyst surface is the basis for the correct description of the NH_3-SCR catalytic performance. Temkin-type kinetics were widely and successfully used to describe the NH_3 adsorption/desorption process over V-based and metal-promoted zeolite catalysts [28,29,30,31]: In this approach, the heterogeneity of the catalytic surface is taken into account considering the activation energy of the desorption process as a linear function of the adsorbed species surface coverage. Recently, a dual site approach was developed by Colombo et al. [64]. At least two families of acid sites for ammonia adsorption are indeed present on zeolites surfaces, namely Brønsted acids sites, where ammonia is strongly adsorbed, and Lewis acid sites, where ammonia is weakly adsorbed. The dual site storage model resulted in

www.manaraa.com

the accurate description of NH_3 adsorption/desorption in the whole 50–550 °C temperature window. Moreover, a detailed kinetic was developed by Olsson et al. [65] in combination with flow reactor experiments to investigate the NO_x adsorption/desorption and NO oxidation over Cu-ZSM-5.

A good SCR catalyst should have a high selectivity of NO_x reduction to N_2 over a wide range of temperatures and excellent hydrothermal stability at high temperatures. Among the various catalysts developed for NH_3 SCR, zeolite based base metal (e.g., Cu, Fe) catalysts are currently being used for meeting diesel NO_x emission standards. Significant research efforts have concentrated on Cu^{2+} ion-exchanged zeolites to study its SCR activity [65,31,66].

High thermal durability is required for the SCR catalyst to remain effective for NO_x emission control. The base metal exchanged zeolite catalysts, Cu-zeolite and Fe-zeolite catalysts have been found to be more thermally stable (exhibit high NO_x conversion efficiency at high temperatures without losing catalytic activity) than vanadium based catalyst formulations at temperatures typical of diesel engine conditions [67,68]. In Figure 2-5, Cu and Fe based catalysts possesses outstanding hydrothermal stability compared to vanadium based SCR.

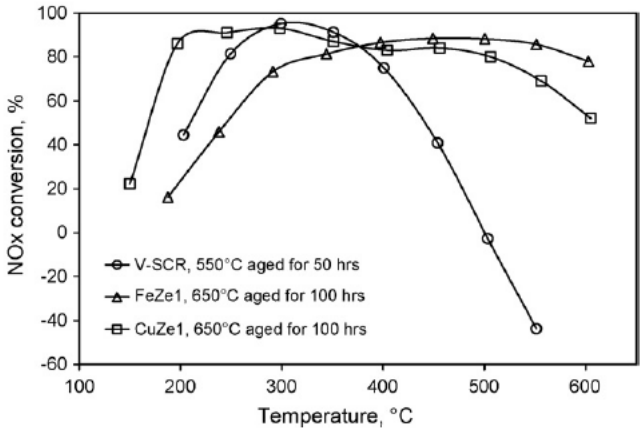

Figure 2-5: Steady-state NO_x conversion efficiency maps of three SCR catalysts with 200ppm NO and 200ppm NH_3 [31]

www.manaraa.com

Recently, a Cu^{2+} ion-exchanged SSZ-13 zeolite with the Chabazite (CHA) structure was reported to be more active and selective in reducing NO with NH_3 compared to Cu-ZSM-5 and Cu-beta [69]. It can be found in Figure 2-6, Cu-SSZ-13 showed essentially no change in NO reduction activity after hydrothermal aging while both Cu-ZSM-5 and Cu-beta were found to lose NO reduction activity primarily at low catalyst temperatures.

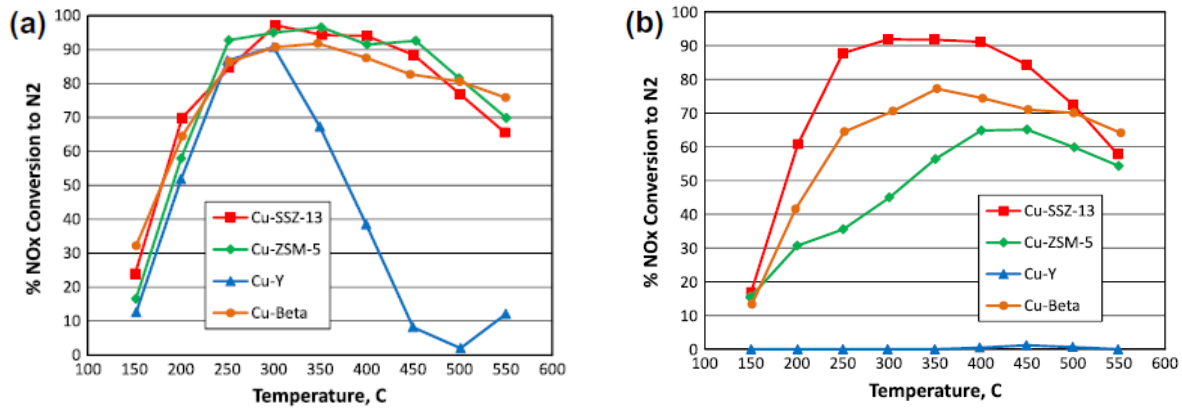

Figure 2-6: NO conversion to N_2 over Cu/zeolites (Feed: 350 ppm NO, 350 ppm NH_3, 14% O_2, 10% H2O in balance N_2) (a) fresh catalyst and (b) after hydrothermal aging (10% H2O in air at 800 °C for 16 h) [69]

2.2 Catalytic kinetics modeling

In the $DeNO_x$ aftertreatment systems, the kinetics associated with a particular catalyst formula play a very important role in the aftertreatment modeling. Basically, there are no general accepted models for CO and HC oxidation and NO_x reduction in automotive catalysis. Many factors affect the observed kinetics, e.g. the catalyst preparation method, the composition of the exhaust gases, mass and heat transfer and all the reaction conditions that the catalyst has been exposed to prior to an experiment.

Mean field modeling is the most used assumptions in developing kinetic models, which assumes that the average coverage of the surface can be used to model the surface reactions. In many cases,

www.manaraa.com

this assumption is questionable. Polycrystalline catalysts, which can be very heterogeneous, consist many exposed crystal planes with different sticking probabilities [70]. However, the good thing is that the deviation from the assumed mean field has less influence at high temperature when the surface mobility and the rate change of the catalyst structure are high [71].

Most kinetic models have been fitted to a Langmuir-Hinshelwood (LH) structured rate equation

$$r_i = \frac{A_i e^{-\frac{E_A}{RT}} C_i^{\alpha_i} C_j^{\beta_j}}{\left(1 + K_i e^{-\frac{\Delta H_i}{RT}} C_i + K_j e^{-\frac{\Delta H_j}{RT}} C_j\right)^{n_i} \left(1 + K_k e^{-\frac{\Delta H_k}{RT}} C_k\right)^{n_k}} \qquad \textit{Eq. 2-1}$$

or a power law model (Olsson and Andersson 2006)

$$r_i = A_i e^{-\frac{E_{Ai}}{RT}} \prod_j C_j^{\alpha_j} \qquad \textit{Eq. 2-2}$$

The power law rate equation is very simple. Theoretically, the power law rate equation can fit almost any reactions but over a small range of conditions. The LH equation has better theoretical foundation for catalytic reactions, which is highly nonlinear.

Detailed microkinetic models of $DeNO_x$ systems were widely documented in the literatures (For TWC, Kwon et al. [72,73]; for LNT [74, 75,76]; for SCR [65,77]). In the detailed microkinetic model, all the surface coverages are calculated. The kinetic parameters are described as functions of coverage as well as temperature. The activation energy and heat of adsorption are affected by other molecules adsorbed on the surface [78]. All of these increase the complexity of kinetic modeling. On the other hand, in most cases, detailed microkinetic models are developed based on simpler catalysis, e.g. Pt/Al_2O_3, $Pt/CeO_2/Al_2O_3$. However, commercial catalysts used for

www.manaraa.com

automotive engine aftertreatment systems consist more complicated catalyst components and structures, where detailed microkinetic models can not be directly applied.

Depending on the objective the kinetic models will be different. For designing of an exhaust system, only the predictions must be accurate, the models and the parameters in the models are of minor importance. For development of a catalyst, it is necessary to identify the rate limiting steps. In this study, our objective is to develop system level exhaust aftertreatment models, which will be used for aftertreatment system optimization and design. Therefore, the accuracy of the model predictions is the first priority.

2.3 Particulate filter

Particulate filters were initially developed in the 1980s for controlling particulate emission from diesel engines in order to meet tightening emission regulations [79]. Diesel particulate filters (DPFs) are widely used in diesel engines as standard aftertreatment devices and give very high efficiency (>90%) to remove diesel particulates [80].

The state-of-art particulate filtration modeling has a multi-scale nature. There are four coexisting scales [81]: entire filter scale (10cm), filter channel scale (mm), filter wall scale (100μm) and pore scale (10μm). The realistic description of the porous structure significantly increases the complexity of the mathematics involved. This is due to the coupling between the physic-chemical mechanisms and geometric complexity of the porous media.

www.manaraa.com

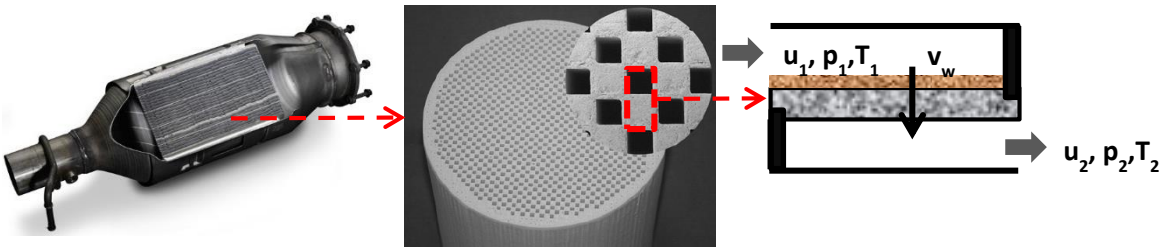

Figure 2-7: Multi-scales of particulate filters

On the largest scale (entire filter scale), most of study is focused on control strategies [82,83,84] of filter operation and interactions among other emission control devices [85,86,]. On the smallest scale (pore scale), advanced simulation tools may need to study the local flow distribution in the porous media as well as the particle deposition mechanisms.

2.3.1 Gasoline particulate filters

In the last decade, SIDI gasoline engines show great benefits on fuel economy and CO_2 reduction compared to port fuel injection (PFI) gasoline engines. However, SIDI engines generate relatively higher particulate emissions than PFI engines [4]. Moreover, the characteristics of the particulate emission vary greatly for SIDI engines fueled with gasoline ethanol blends [87,88,89]. It was reported that higher ethanol content reduces the number concentration of particulates in the region near the peak of the particulate distribution [88].

For compression ignition engines, as advanced combustion strategies (PCCI and RCCI [90]) were introduced and applied, the particulates were greatly reduced compared to conventional diesel combustion engines. It was found that the particle number concentration of dual-fuel RCCI [90] engines was much less than that of conventional diesel and PCCI diesel engines for the entire size range [91].Traditional DPFs that work for conventional diesel engines may fail to work. Since there is significantly less PM emission generated for advanced diesel combustion engines, there is

www.manaraa.com

less likelihood of forming a "soot cake", which traditional DPFs rely on. Therefore, there is a great challenge to develop advanced filters to meet future PM regulations.

Gasoline particulate filters (GPFs) [92,93,94] were already being introduced on SIDI engines in order to meet particulate emission regulations on light-duty gasoline engines. It was reported that GPFs generally have relatively lower filtration efficiency compared to traditional DPFs [92]. Another concern for GPFs is their impact on back pressure and increase in fuel consumption and CO_2 emission.

Some researchers have shown that current DPFs are able to give about 70~80% filtration efficiency for SIDI engines. Rubino et al. [95] used a cordierite wall-flow DPF with a cell density of 200 and wall thickness of 0.43 mm to study the filtration of artificially generated ultrafine carbon particles. It was found that filtration efficiency decreased with particle size (from ~80% at 20 nm to ~70% at 100 nm) and the filtration efficiency did not change much with time (up to 20 hours). Chan et al. [92] reported that the averaged GPF filtration efficiency is 82% and 76% for FTP-75 and US06 cycle respectively. Shimoda et al. [94] modified the cell density and wall thickness of their DPFs to reduce back pressure. They obtained a PN efficiency of roughly 75%. Saito et al. [96] studied the impact of mean pore size on filtration efficiency of GPFs. It was found that smaller pore diameter showed higher filtration efficiency, which gave approximately 78% for the smallest mean pore size filter compared to 60% for the larger mean pore size filter. This indicates that the structure of the porous filter is very critical on filtration efficiency for GPFs.

Effects of pressure drop across GPFs on engine performance were evaluated by some researchers. The work done by Rubino et al. [95] showed that the pressure drop across a GPF increased with the particle mass loaded, with a value of 200 Pa for a clean filter to about 800 Pa after an exposure

www.manaraa.com

of 10 hours to a total carbon particle mass of about 35 mg. Saito et al. [96] showed that a pressure drop increase by 10 KPa resulted in an engine power reduction by approximately 1% on a 1.6L SIDI engine at full load conditions, which is 0.7 kW at 3000 rpm and in 1.3 kW at 6000 rpm. Pressure drop can be significantly reduced by changing the GPF location in the exhaust system from close coupled (CC) position to the under floor (UF). The UF-GPF showed 25% lower pressure drop than the CC-GPF in the extra-urban driving cycle (EUDC) [96]. In the UF position, due to lower temperature and lower gas flow, pressure drop can be minimized.

Regeneration characteristics are also very important for development of particulate filters. For DPFs, lots of efforts have been put into DPF regeneration strategies and control. However, the situation is different for GPFs. SIDI engines have lower soot emission with higher percentage of organic components. Engine exhaust temperature is higher compared to diesel engines. The soot retained in a GPF can be easier burned if oxidation catalysts are coated. Shimoda et al. [94] found that utilizing a GDI lean burn engine, soot combustion in a catalyzed GPF at λ=1 (1.0~1.6% O_2) begins at 500°C. At λ=1.16 (3.2~5.2% O_2), soot combustion begins at 400 °C. Another experimental study of a close coupled three-way catalyst (TWC) and a catalyzed GPF was conducted on two modern SIDI engines by Richter et al. [92]. He found that the precious metal containing washcoat accelerated the regeneration of a filter when loaded with artificial soot. Saito et al. [96] showed that the accumulated PM was regenerated in a uncoated prototype GPF with soot loading of 2.0g/L during NEDC in a close-coupled position but less change was observed at under-floor position. The temperature needed for GPF regeneration seems to be around 400 °C. Similarly, Chan et al. [97] found that limited soot regeneration in the uncoated under-floor GPF was observed at cold ambient temperatures over the FTP-75 drive cycle. However, multiple

www.manaraa.com

spontaneous soot regenerations were observed over the US06 drive cycle. Therefore, under-floor GPF may still need active regenerations but with a much less frequency.

2.4 Filtration modeling

Filtration can be defined as the process of separating dispersed particles from a dispersing fluid by means of a porous media [98]. Essentially, the filtration process is a problem of multiphase flow through porous medium. Three objects take part in the filtration process: dispersed particles, dispersing fluid and the porous medium. Filter efficiency describes the deposition of particles in a porous media. Theoretically, the filtration efficiency is dependent on characteristics of the dispersed particles, the dispersing fluid and the porous medium. The objective of this paper is to develop a computational model to predict initial (or clean) filtration efficiency of particulate filters.

Numerous methods have been used to study the filtration by simulating flow through porous media. These methods can be classified as: microscopic and macroscopic. Microscopic approach tries to explain the physics of the deposition process within the filter from trajectory analysis, while the macroscopic approach considers the filter media as a "black box".

The classical filtration theory uses the "unit-cell" approach [2,3]. The "unit-cell" approach is based on the flow field solution derived by Kuwabara [99] and Happel [100] for low speed laminar flow in randomly packed bed. By solving convection-diffusion equation numerically and conducting analysis of the trajectory of particles, single collector efficiency of different individual collection mechanisms can be theoretically derived. The analysis treats the particles as if they are diffusion "points" since the particles are small compared to the collectors. Friedlander [101] calculated the diffusion efficiency by solving the boundary layer form of the steady state convective diffusion

www.manaraa.com

equation considering the particle capture process occurs near the surface of the collector. By applying Friedlander's analysis to packed beds, Lee et al. [102] derived a single collector efficiency due to diffusion and interception based on Kuwabara's flow [99]. This "unit-cell" filtration model has been widely used in DPF modeling [103,104,105]. Some correlations for predicting single collector efficiency were proposed later. Rajagopalan and Tien [106] developed a correlation for single collector efficiency by using the "unit-cell" approach based on the Happel's flow solution [100]. Tufenkji and Elimelech [107] then developed a correlation for a single collector efficiency which considers van der Waals forces and hydrodynamic interactions. These researchers attempted to obtain theoretical formulas that express particle capture in terms of porosity without firm commitment to a particular flow field. That is because agreement between theoretical predictions and experiments would seem to be the proper criterion for choice among flow fields.

The microscopic approach is very helpful to understand the local flow near the pores and particle movement. One of the microscopic approaches is the Lattice Boltzmann method (LBM). Essentially, LBM is a mesoscopic approach for simulating computational fluid dynamics by solving discretized Boltzmann equations. An attractive feature of LBM is the ease of addressing complex boundary conditions by implementing a very simple scheme [108]. However, one of the main challenges of LBM is the reconstruction of the porous structure of the filter [109].

The pore-scale flow analysis conducted by Hayashi et al. using LBM method showed that the dominant filtration mechanism is Brownian diffusion for particles less than 300 nm and the direct interception for particles over 300 nm [110]. Recently, Long et al. [111] developed a correlation for the clean bed filter coefficient for Brownian particles (50 nm<dp< 300 nm) based on Lattice

www.manaraa.com

Boltzmann (LB) simulations in random packing of spheres of uniform diameter. Later, a similar correlation with different dependent coefficients on diffusion and interception was proposed through regression analysis for a set of numerical breakthrough simulations of flow through a filter consisting of non-spherical collectors [112]. These two LB correlations were based on simulations in packing with porosities around 0.3~0.43. Additional investigations are necessary to test the model over a wide range of porosities.

Generally, filtration efficiency correlations developed based on the "unit-cell" approach can be classified as "mean" models. This approach uses a representative mean pore size and mean porosity to model the porous medium. The porous medium is assumed to be homogeneous. The flow field and the capture efficiency are dependent on the mean properties of the porous medium. However, in most realistic filters, this assumption does not hold. The porous medium has heterogeneous micro-structure, which spans a wide range of scales. For particulates from advanced combustion sources such as GDI with small particulate sizes, the filtration characteristics are more dependent on the porous wall structure [113]. Therefore, one of the challenges for filtration modeling is how to incorporate the filter micro-structure information into the model.

Different mechanisms of filtration are described in Appendix B. For small particles, diffusion, interception and inertia mechanisms are the main filtration mechanisms. The trajectories of small particles are shown in Figure 2-8 for these three mechanisms.

www.manaraa.com

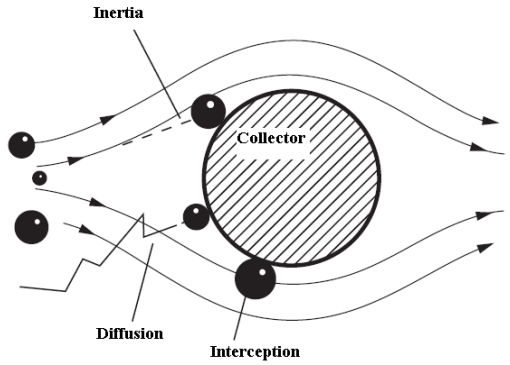

Figure 2-8: Trajectories for diffusion, interception and inertia deposition

Moreover, the filtration mechanisms are very complicated for nano-scale particles. Kim et al. found that the filtration efficiencies were independent of humidity and affected by the particle charge in the case of particles below 100 nm in size [114]. Wang et al. reported that the thermal impact velocity of a particle may exceed the critical sticking velocity for particles in the size range between 1 and 10 nm and particle may rebound from the filter surface [115]. Further complication of the flow resistance arises when the diameter of fiber or sphere is comparable with the mean free path of air molecules. At normal atmospheric pressure, the mean free path of air molecules is about 0.06 μm and is inversely proportional to the pressure [116]. As a result, there is a decrease in the pressure drop across the filter due to the gas slip pass the fiber or sphere.

Some widely used classic filtration efficiency models including diffusion and interception are summarized in Table 2-1.

www.manaraa.com

Table 2-1: Summary of filtration models

Model expression	Notes	Investigator(s)
$E_D = 2\left(\frac{3\pi}{4}\right)^{(2/3)}\left(\frac{\varepsilon}{K_s}\right)^{1/3} Pe^{-2/3}$ $E_R = \frac{3}{2}\frac{1-\varepsilon}{K_s}\frac{N_R^2}{(1+N_R)^m}$ $K_s = 1-\frac{9}{5}\beta^{1/3}-\frac{1}{5}\beta^2+\beta;\ m=\frac{1+2\varepsilon}{3(1-\varepsilon)}$	spherical "unit cell" using Kuwabara flow field	Lee et al. 1979, Konstandopoulos et al 2000, Lee et al. 1980
$E_D = 2\left(\frac{3\pi}{4}\right)^{(2/3)}\left(\frac{1-\beta^{5/3}}{H_s}\right)^{1/3} Pe^{-2/3}$ $E_R = \frac{3}{2}\frac{(1-\beta^{5/3})}{H_s}N_R^2$ $H_s = 1-\frac{3}{2}\beta^{1/3}+\frac{3}{2}\beta^{5/3}-\beta^2$	spherical "unit cell" using Happel flow field	Lee et al. 1981 Yao et al. 1971
$E_D = \frac{2.9}{K_c^{1/3}}Pe^{-2/3}+0.624Pe^{-1}$ $E_R = \frac{1}{2K_c}\left[(1+N_R)^{-1}-(1+N_R)+2(1+N_R)\ln(1+N_R)\right]$ $K_c = -0.75-0.5\ln\beta+\beta-\frac{1}{4}\beta^2$	cylindrical "unit cell" using Kuwabara flow field	Stechkina et al. 1966 Kirsch et al. 1973 Matteson et al. 1987
$E_D = \frac{2.9}{H_c^{1/3}}Pe^{-2/3}+0.624Pe^{-1}$ $E_R = \frac{1}{2H_c}\left[(1+N_R)^{-1}-(1+N_R)+2(1+N_R)\ln(1+N_R)\right]$ $H_c = -0.5-0.5\ln\beta+\beta-\frac{1}{4}\beta^2$	cylindrical "unit cell" using Happel flow field	Stechkina et al. 1966 Kirsch et al. 1973 Matteson et al. 1987
$E_D = (15.56\pm0.21)\frac{(1-\varepsilon)^3}{\varepsilon^2}Pe^{-0.65\pm0.023}N_R^{\ 0.19\pm0.03}$	LB simulation correlation (spherical collectors)	Long et al. 2009
$E_D = c_1\frac{(1-\varepsilon)^3}{\varepsilon^2}Pe^{c_2}N_R^{\ c_3}$ $E_D = (8.34\pm0.75)\frac{(1-\varepsilon)^3}{\varepsilon^2}Pe^{-0.53\pm0.015}N_R^{\ 0.03\pm0.0175}$	LB simulation correlation (non-spherical collectors) c_1, c_2, c_3 are obtained by multivariate regression analysis	Long et al. 2010

www.manaraa.com

Chapter 3 - TWC Modeling with NH_3 and N_2O Kinetics

In this chapter, a TWC and a LNT model are developed. Three different types of experimental data were used to validate the models. Most effort was taken to validate the TWC model, in particular for the ammonia kinetics in the TWC.

3.1 Model description

The $DeNO_x$ aftertreatment models including a TWC and a LNT are part of the emission and aftertreatment system models [117,118,119] developed in Engine Research Center (ERC). In order to reduce model development process and focus on validations using raw exhaust data, the model was developed by commercial package of GT-Power (GT-SUTE manual). One of the reasons for selecting GT-Power as a modeling tool rather than developing in-house code is the simplicity of the 1-D channel flow in typical TWCs and LNTs.

A single-channel, one-dimensional model used to describe the monolith converter has been developed with the following assumptions: 1) steady state, 2) axisymmetric geometry, 3) neglect axial diffusion of mass and heat (Axial Peclet number, defined as the ratio of axial diffusion time to the axial convection time, is about 1000 for heat and mass transport, indicating the dominance of the convective heat and mass transfer [120]). However, a quasi-steady diffusion model was used to account for mass transfer between bulk gas and washcoat by assuming that the reaction rate is equal to the diffusion rate. The governing equations of the model under these simplifications and assumptions are given below:

Mass balance for the gas phase:

www.manaraa.com

$$-u\frac{\partial C_i^g}{\partial x}+k_{m,i}A_e(C_i^g-C_i^s)=0 \qquad \textbf{Eq. 3-1}$$

Mass balance for the solid phase:

$$k_{m,i}A_e(C_i^g-C_i^s)=R_i \qquad \textbf{Eq. 3-2}$$

Energy balance for the gas phase:

$$\rho_g C_{p,g}u\frac{\partial T_g}{\partial x}=hA_e(T_s-T_g) \qquad \textbf{Eq. 3-3}$$

Energy balance for the solid phase:

$$\rho_s C_{p,s}\frac{\partial T_s}{\partial t}=k_s\frac{\partial^2 T_s}{\partial^2 z}+hA_e(T_g-T_s)+\sum(-\Delta H_i)R_i \qquad \textbf{Eq. 3-4}$$

The heat and mass transfer coefficients, h and $k_{m,i}$ are calculated from the following correlations:

$$h=\frac{Nu\cdot k_g}{d_h} \qquad \textbf{Eq. 3-5}$$

$$k_{m,i}=\frac{Sh\cdot D_{g,i}}{d_h} \qquad \textbf{Eq. 3-6}$$

A constant Nusselt number of 3 is used, which is accurate for fully developed laminar flow in square channels [121]. The Sherwood number is assumed to be equal to the Nusselt number. Considering heat loss to the ambient environment, external heat transfer between the catalyst shell and ambient was modeled by introducing a heat transfer coefficient (combining convection and radiation), which was calibrated to match the catalyst wall temperatures.

The TWC and LNT model developed in GT-Power were integrated into the system aftertreatment models by Simulink. The schematic of the TWC model is shown in Figure 3-1.

www.manaraa.com

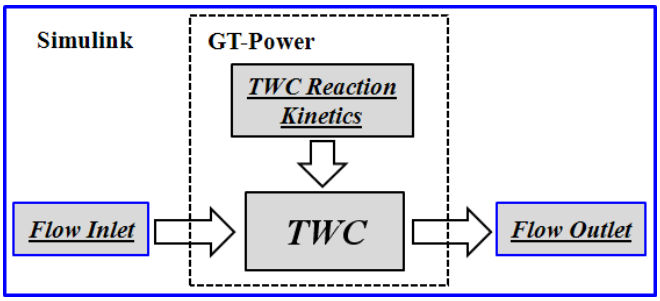

Figure 3-1: Schematic of the TWC model in GT-Power integrated with Simulink

The current study is not aimed to pursuing a reaction network consisting of truly elementary reactions. The objective is to develop a kinetic model that contains a minimum number of reaction steps and species yet is comprehensive enough to explain all the important experimental trends. In this work, a global macro-kinetic modeling approach is used to model surface reactions in a TWC and a LNT under the mean field assumption. The kinetic models have LH structured rate equations. For oxygen or NO_x storage, a variable describing the degree of storage was used.

The specific reaction rate (turnover rate) is expressed in [mole/mole-site/s], where the mole-site refers to the active sites which actually participate in the catalytic reactions. The active sites (a_i) depend on the active PGM or storage loading level and dispersion. By multiplying the specific reaction rate by the active site density of catalyst in [mole-site/m^3], the total reaction rate in [mole/m^3/s] can be obtained as below:

$$R_i = r_i \cdot a_i \qquad \textit{Eq. 3-7}$$

The specific reaction rate expression in the kinetic model is shown as:

$$r_i = k_i \cdot [c_i][c_j] \cdot f(G_i) \cdot \theta_i \qquad \textit{Eq. 3-8}$$

where r_i is the reaction rate coefficient, which is in the Arrhenius form

$$k_i = A_i \cdot T^{b_i} \exp(-\frac{E_i}{R_u T}) \qquad \textit{Eq. 3-9}$$

www.manaraa.com

Here $[c_i]$ and $[c_j]$ are the concentration of reactants; $f(G_i)$ is the inhibition function; θ_i is the surface coverage ($0 \le \theta_i \le 1$) if adsorption and desorption are considered.

3.2 TWC kinetics

The TWC kinetics from [120] were used as base kinetics in this study. The kinetics include carbon monoxide and hydrocarbon oxidation, NO reductions, water-gas shift, steam reforming and oxygen storage. In addition to these, ammonia and nitrous oxide formation mechanisms in TWC were also added into the current mechanism. Overall, the TWC global kinetics have 20 surface reactions. All the kinetic parameters and reaction rate expressions are tabulated in Appendix C.

The base kinetics in [120] were obtained from different vehicle data based on different catalysts. However, none of these catalysts are the same as the one used in this study. Therefore, this base set of kinetics was tested first and then modified manually by calibrating the reaction constants of HC and CO oxidation and NO reduction reactions so as to get a quantitative match of temperatures, CO and HC concentrations from experiments.

Species adsorption and desorption to and from PGM sites are so fast that they can be considered to be in equilibrium. Reactions 1-14 in TWC kinetics are therefore modeled as global reactions without considering storage, but dependent on the number of PGM sites. However, oxygen storage is modeled. A variable of surface coverage describing the degree of oxygen storage is introduced. The coverage parameter θ is the ratio of the oxygen storage component in the higher oxidation state to the total available oxygen storage capacity, which is defined as:

$$\theta = \frac{\text{moles of } CeO_2}{\text{moles of } CeO_2 + 2 \cdot \text{moles of } Ce_2O_3} \qquad \textit{Eq. 3-10}$$

www.manaraa.com

The equation for surface coverage parameter θ is shown in Eq. 3-11. The initial coverage site of OSC θ is set to zero.

$$\frac{d\theta}{dt} = r(T_s, c_s, \theta) = (4r_{15} + 2r_{16}) - (2r_{17} + 12r_{18} + 14r_{19} + 2r_{20}) \qquad \textit{Eq. 3-11}$$

3.2.1 Ammonia kinetics

It was found that a large amount of NH_3 can be formed during rich operations in a TWC [41]. During rich operations, there is a high concentration of H_2 due to water gas shift and steam reforming reactions. NH_3 is produced when NO is reduced by H_2. However, NH_3 oxidation with NO and O_2 at is active at high temperatures [46,127].

Three new reactions [129] were added into the global reaction mechanism to capture NH_3 formation and NH_3 oxidation with NO and O_2. These new reactions are described in Table 3-1.

Table 3-1: NH_3 kinetics in the TWC model

Description	Reaction
NH_3 oxidation with O_2	$NH_3+1.25O_2 \rightarrow NO+1.5H_2O$
NH_3 formation	$NO+2.5H_2 \rightarrow NH_3+H_2O$
NH_3 oxidation with NO	$NH_3+1.5NO \rightarrow 1.25N_2+1.5H_2O$

3.2.2 Nitrous oxide kinetics

The pathways for N_2O formation include incomplete NO_x reduction by various reductants (CO, HCs and H_2), interaction of NH_3 and NO and non-selective NH_3 oxidation. N_2O can be further reduced to N_2 by various reductants at high temperatures [53]. N_2O formation in TWC systems varies greatly in different catalysts, reductants, temperatures and drive cycles. The main characteristics of N_2O formation [39,52,122] in TWC systems are summarized below:

- a partial reduction product of NO_x
- formed in a narrow temperature window for hydrocarbons reductants

www.manaraa.com

  - preferably formed at low temperatures
  - peaks at around 200 ~ 250°C
  - appears at around 150°C and very little beyond 400°C
- the temperature window of N_2O formation depends on types of reductants
- generally produced during rich to lean transients
- increases with aged catalysts

Considering the exhaust temperature window of SIDI engines (>400°C), only NO_x reduction by hydrocarbons was considered. C_3H_6 was selected as a representative of hydrocarbons. Therefore new N_2O kinetics in TWC systems are shown in Table 3-2.

Table 3-2: N_2O kinetics in the TWC model

Description	Reaction
N_2O formation	$NO+1/18C_3H_6 \rightarrow 0.5N_2O+1/6CO_2+1/6H_2O$
N_2O destruction	$N_2O+1/9C_3H_6 \rightarrow N_2+1/3CO_2+1/3H_2O$

Based on the characteristics of N_2O formation, N_2O formation in TWC systems is highly dependent on temperature. In order to capture the temperature dependence of N_2O into the kinetics, an inhibition function for N_2O is introduced and shown in Equation (1). Essentially, the inhibition function is a Gaussian type (non-symmetric) probability density function (PDF) for N_2O formation at different temperatures.

$$f(G) = f_0 + \exp\left(-\frac{(T_s - T_{m1})^2}{\sigma_1^2}\right) \cdot \exp\left(-\frac{(T_s - T_{m2})^2}{\sigma_2^2}\right) \qquad \textit{Eq. 3-12}$$

f_0 is a small constant (0.05), which makes the reaction equations not too stiff and easy to be solved. T_{m1}, T_{m2}, σ_1 and σ_2 are inhibition constants. Their values are chosen to be 400°C, 550°C, 280, and 90 respectively in order to make the inhibition function fit the general characteristics of N_2O formation. The inhibition function with respect to TWC surface temperature is shown in Figure 3-2.

www.manaraa.com

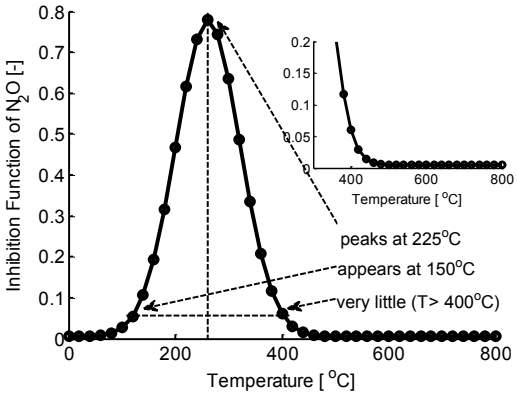

Figure 3-2: Inhibition function of N_2O

3.3 TWC model validation

Experimental data used to validate the model were collected on a BMW 120i lean gasoline engine vehicle. The vehicle was operated on a chassis dynamometer at Oak Ridge National Laboratory (ORNL) [123]. The engine is a 2.0 liter, four cylinder gasoline engine with a compression ratio of 12.0. The engine is equipped with a 200 bar direct injection, a dual variable valve timing (VVT) and an EGR system.

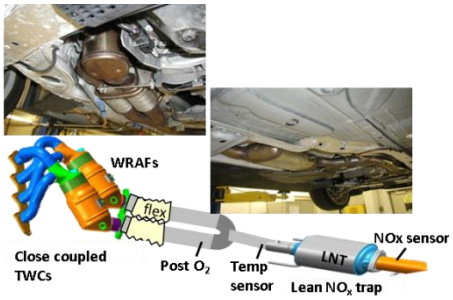

Figure 3-3: Configuration of aftertreatment system on a BMW 120i lean gasoline engine vehicle [123]

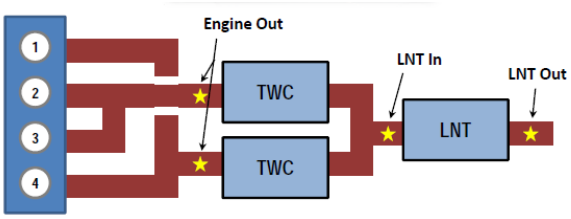

Figure 3-4: Sampling locations in the exhaust system [123]

The vehicle's exhaust system is composed of two three-way catalysts (TWCs) which were close coupled with two exhaust manifolds (one for each pair of cylinders: 1-4 and 2-3). A LNT was placed in an under-floor position downstream of the merge point of the two TWCs. Emission species, temperature and pressure were measured at engine exhaust manifolds (upstream of

www.manaraa.com

TWCs), downstream of TWCs and downstream of the LNT. The schematic of engine exhaust and sampling positions is shown in Figure 3-4. In this study, only one TWC brick was simulated.

The vehicle had previously accumulated sufficient mileage to de-green the catalysts. The catalyst is a production TWC catalyst sold in a lean stratified vehicle. The geometry of one TWC brick is shown in Table 3-3.

Table 3-3: Specification of the TWC brick

Catalyst	*Value*
Volume [liters]	0.62
Length [inch]	4
Diameter [inch]	3.47
Cell density [cells per square inch]	600
Wall thickness [inch]	4.7e-3

There are three different types of data for model validations. Five time-resolved data sets were collected at steady state (with the engine operating at fixed load and speed). A mass spectrometer [124] with high temporal resolution was used to conduct time-resolved measurements of emission transients. A large set of time-averaged steady state data were collected at various speeds and loads for the purpose of collecting emissions data in a wide range of engine operating conditions. In addition to steady state operation, the vehicle was operated at a transient US Federal Test Procedure (FTP) drive cycle with cold start conditions.

The experimental data collected upstream of the TWC were used as the inlet conditions for the model. Predicted temperatures as well as exhaust species at the TWC outlet were compared with the measurements downstream of the TWC.

www.manaraa.com

3.3.1 Time-resolved Steady State validation

Two sets of time-resolved steady state data were shown in this report to validate the TWC kinetics. The first set of time-resolved data were taken at a constant speed of 3500 RPM and 30% load and the other one were taken at at a constant speed of 4000 RPM and 50%.

Since most of reactions are taking place at the wall surfaces of a TWC, wall temperature is very critical to the TWC performance. Therefore, the catalyst wall temperature and the TWC outlet gas temperature are compared with the experimental data in Figure 3-5 and Figure 3-6. The predicted TWC outlet gas temperature and catalyst temperatures capture the data fairly well.

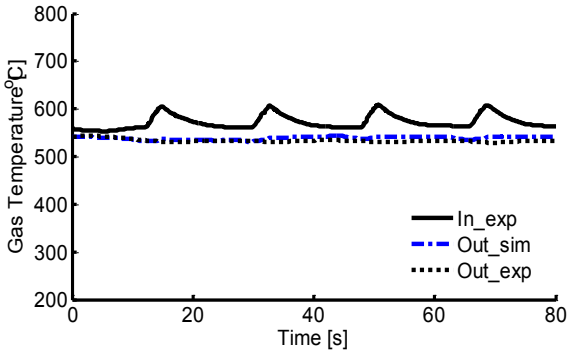

Figure 3-5: TWC gas temperature comparison at 3500 rpm, 30% load

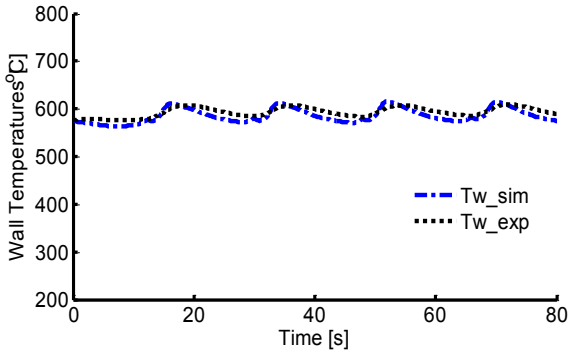

Figure 3-6: TWC wall temperature comparison at 3500 rpm, 30% load

Exhaust emissions comparisons are shown in Figure 3-7 to Figure 3-14. The oxygen concentration comparison is shown in Figure 3-7. There is some oxidation during rich periods even through the oxygen concentration is very low, which is captured by the model. The NO_x prediction in Figure 3-8 is good at lean and rich periods with a total conversion rate of 27.13% compared to 21.3% from experimental data.

www.manaraa.com

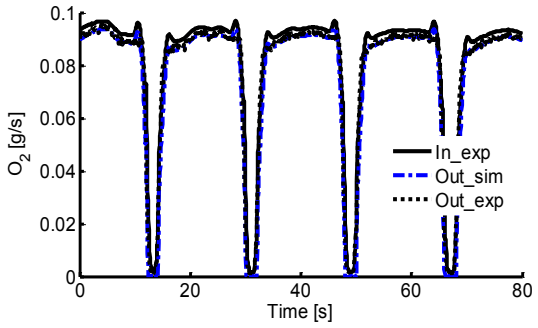

Figure 3-7: TWC oxygen concentration comparison at 3500 rpm, 30% load

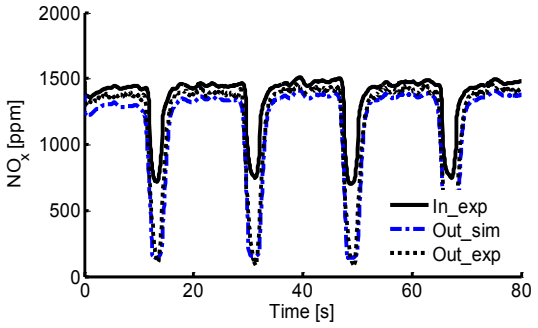

Figure 3-8: TWC NO_x concentration comparison at 3500 rpm, 30% load

CO and HCs comparisons are shown in Figure 3-9 and Figure 3-10 respectively. Significant reductions of CO and HCs at rich period are captured. Even though the magnitudes of CO and HCs at rich periods are slightly higher, the total conversion rates for CO and HCs are very comparable to the data.

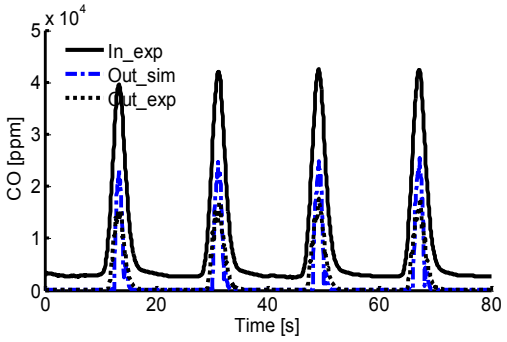

Figure 3-9: TWC CO concentration comparison at 3500 rpm, 20% load

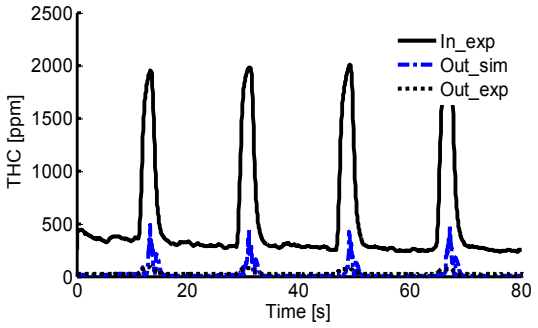

Figure 3-10: TWC HCs concentration comparison at 3500 rpm, 20% load

CO levels drop over TWCs while H_2 levels increase suggests that TWC is converting CO to H_2 via the water gas shift (WGD) reaction. Analysis of H_2 before and after TWCs shows that TWC is affecting mixture of reductants. Predicted N_2O in Figure 3-12 agrees with the experimental N_2O very well at lean, even though the data show that N_2O is a little bit noisy at lean periods. The model predicted almost zero N_2O at rich periods, which is indicated by the experimental data as well. In

www.manaraa.com

addition to that, the model successfully predicted the sharp N_2O peak, which appears at the transients from lean to rich due to the increase of hydrocarbons.

In Figure 3-13, a large amount of NH_3 is generated during the rich periods, which is also shown by the model. The magnitudes of predicted NH_3 peaks at rich periods are slightly lower than the data. However, the locations of the peaks are well predicted.

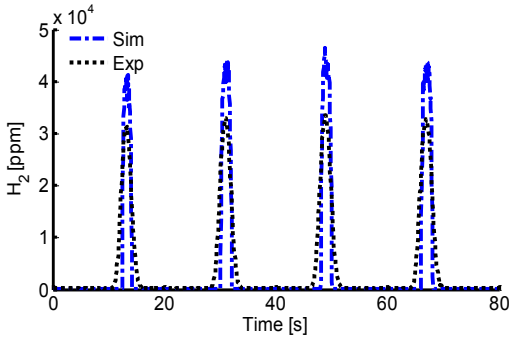

Figure 3-11: TWC hydrogen concentration comparison at 3500 rpm, 20% load

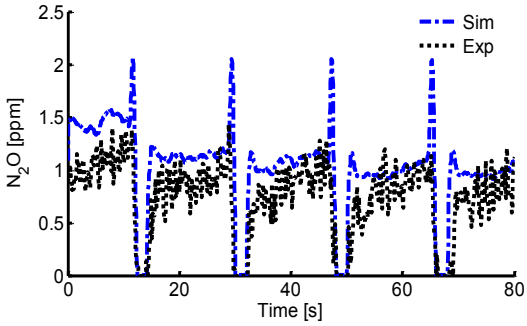

Figure 3-12: TWC nitrous oxide concentration comparison at 3500 rpm, 20% load

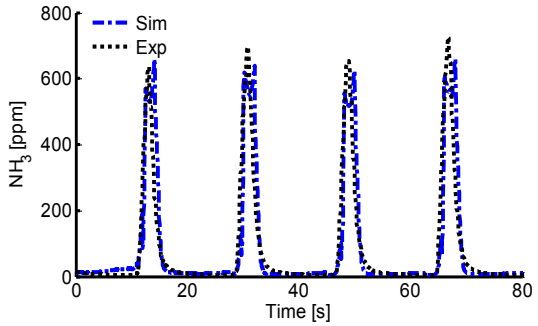

Figure 3-13: TWC ammonia concentration comparison at 3500 rpm, 20% load

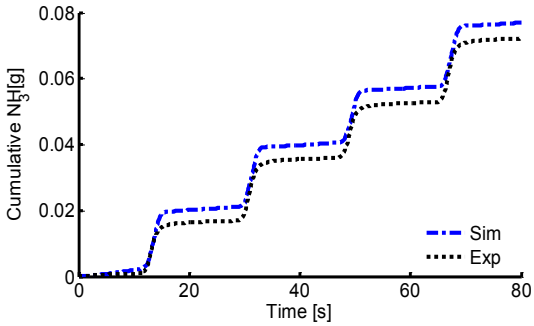

Figure 3-14: TWC cumulative ammonia concentration comparison at 3500 rpm, 20% load

Another set of time-resolved steady state data validations, which were taken at a constant speed of 4000 RPM and 50% load, were shown in Figure F 1and Figure F 2 in Appendix F. The model shows a large quantity of NH_3 during rich periods as well as in Figure 3-13. This indicated that

www.manaraa.com

most of NH_3 is formed during rich periods, when high concentrations of reductants are available. Very little NH_3 formation is observed in lean periods.

3.3.2 Time-averaged Steady State Results

Time-averaged data were time averaged over lean or rich period at each operating condition (a specific speed and load). Time-averaged data may not provide detailed simultaneous species concentrations like the time-resolved data. However, Time-averaged data are very useful to examine the kinetics in a wide window of exhaust conditions and show the accuracy and limitations of the model.

At each steady state engine operating condition, the engine was switched between lean and rich at a specific speed and load. The engine speed was varied from 1500 rpm to 4500 rpm. The load was varied from 5% to 60% maximum load at each speed. There are totally 1550 steady state operating points including lean and rich conditions. Each steady-state point was simulated. Table 3-4 shows the range of engine controlled AFR, exhaust mass flow rate, exhaust temperature and emission concentrations we studied at lean and rich periods.

Table 3-4: Engine and exhaust conditions of time-averaged steady state data

Conditions	*Lean*	*Rich*
Engine controlled ϕ [-]	0.46 ~ 0.75	1.15 ~ 1.25
Mass flow rate [g/s]	6.7 ~ 72	7.0 ~ 46.8
Space velocity [1/s]	246.5 ~ 3737	291 ~ 2483
Exhaust temperature [°C]	337~ 716	413 ~ 682
NO_x [ppm]	156 ~ 2528	483 ~ 1533
CO [ppm]	265 ~ 4126	13937 ~ 34680
HC [ppm]	20 ~ 871	295 ~ 1176

Figure 3-15 shows an example of time-averaged steady state oxygen mass flow rate. The black dotted line represents TWC inlet oxygen, which was from experimental measurement and used as the input of the model. The TWC inlet oxygen is a constant during lean period and changes to a

www.manaraa.com

lower constant during rich period. The circle and square symbols are time-averaged TWC outlet experimental data at steady-state lean and rich conditions respectively.

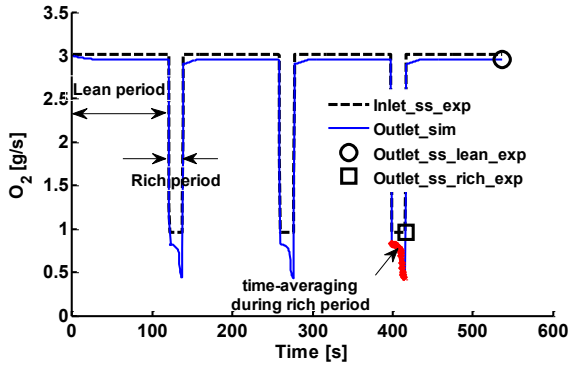

Figure 3-15: Example of time-averaged steady state oxygen mass flow rate

In order to compare the model results with experimental data and to make sure that simulated TWC outlet exhaust achieved steady state conditions, three lean/rich cycles were simulated. Simulation results were compared with time-averaged experimental data at lean and rich conditions separately. At lean condition, simulated TWC outlet results at the end of the lean period were picked for comparisons. At rich condition, simulated TWC outlet results were integrated with time and averaged over the rich period for comparisons because of the transient nature of TWC performance at rich conditions.

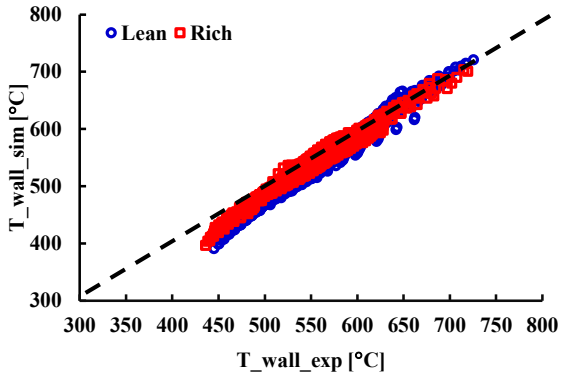

Figure 3-16: Comparison of time-averaged TWC wall temperature at lean (blue) and rich (red) periods

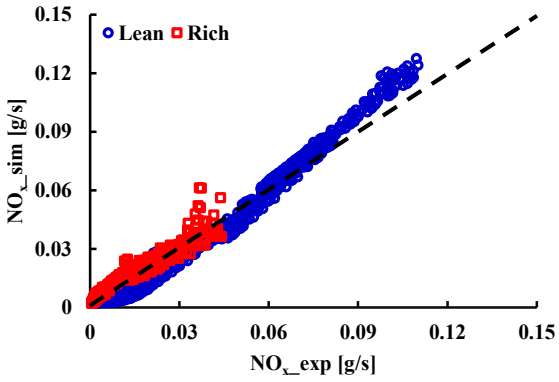

Figure 3-17: Comparison of time-averaged NO_x emission at lean (blue) and rich (red) periods

www.manaraa.com

Comparisons of TWC wall temperatures at lean and rich conditions are shown in the scatter plot in Figure 3-16. Predicted TWC wall temperatures match very well with the data at lean and rich conditions. However, there are still some under-predictions for low temperature cases. To further explore where the wall temperatures were under-predicted, a phasing comparison was carried out. The phasing comparison of the wall temperature at rich conditions is shown in Figure 3-18. Though comparing the wall temperatures with the experimental data in a 2-D (speed and load) space, it is readily to see that the wall temperature is under-predicted at low speeds and low loads and slightly over-predicted at high speeds and high loads. Overall, the temperature distribution in the speed and load space is very similar to the experimental data. The comparisons of CO and HC are shown in Figure F 3 and Figure F 4 respectively. Higher CO was predicted at rich conditions, which is consistent with calculated wall temperatures.

The NO_x comparisons at lean and rich conditions are shown in Figure 3-17. There is a good agreement between predicted NO_x and experimental data. However, the predicted NO_x is slightly higher than the data for higher NO_x cases at lean conditions. Similarly, through the phasing comparison of NO_x in Figure 3-19 at lean conditions, it can be seen that the NO_x is over-predicted at high speed and high load conditions.

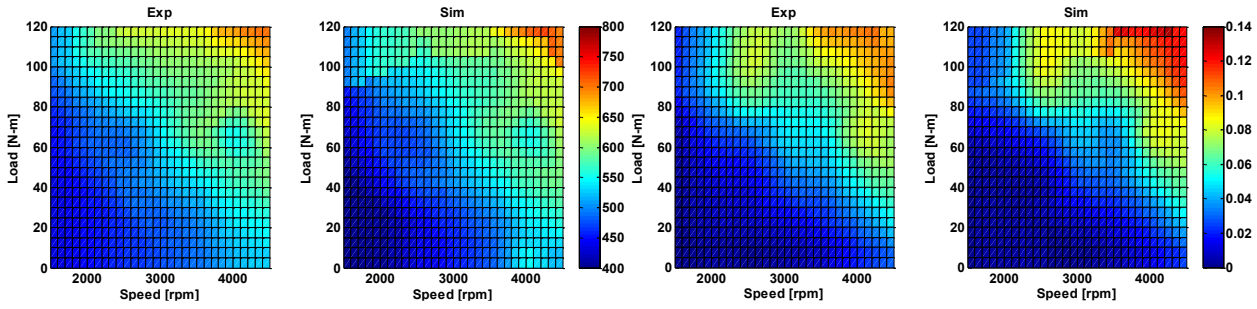

Figure 3-18: Phasing comparison of time-averaged TWC wall temperature at rich period

Figure 3-19: Phasing comparison of time-averaged NO_x at lean period

www.manaraa.com

In order to examine NH_3 and N_2O kinetics in the model by using the time-averaged steady state data, the amount of NH_3 and N_2O produced in TWC systems were plotted in $\alpha - T$ space. T is the engine out exhaust temperature. α is defined as the percentage of yield NH_3 or N_2O in TWC from the engine out NO_x in Eq. 3-13.

$$\alpha = \frac{\text{yield } NH_3 \text{ or } N_2O}{\text{engine out } NO_x} \times 100\% \qquad \textit{Eq. 3-13}$$

By definition, $\alpha - T$ plot shows the yield NH_3 or N_2O in TWC from the engine out NO_x emission at corresponding engine out exhaust temperatures. Essentially, $\alpha - T$ plot indicates the temperature dependence of the conversion rate of selected species from NO_x and is very helpful to examine the NH_3 and N_2O kinetics.

Figure 3-20 shows the comparison of NH_3 at lean and rich conditions between experimental data and simulation results in $\alpha - T$ space. The model and experimental data show that much less NH_3 (less than 5%) is produced at lean conditions. However, there is some discrepancy at low exhaust temperatures (less than 400 °C). At rich conditions, the NH_3 data show a single "peak" in the $\alpha - T$ space. The peak of NH_3 formation is around 500 °C. In other words, the conversion rate of NH_3 increases with temperature when the temperature is less than 500°C and starts to decrease with temperature when the temperature is higher than 500°C. The model successfully predicted the peak. Unfortunately the kinetics did not predict NH_3 formation very well at low temperatures under rich operations. If we look at the amount of NH_3 produced in the TWC with the engine out temperature in Figure 3-21, it is readily to see a single "peak" characteristic from the data is captured by the model.

Comparison of N_2O at lean and rich conditions between experimental data and simulations in $\alpha - T$ space is shown in

www.manaraa.com

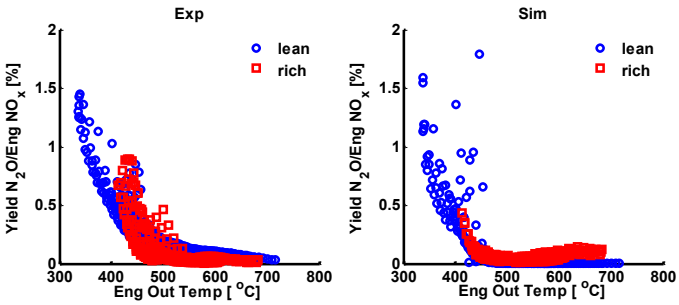

Figure 3-22: Comparison of time-averaged αN_2O at lean (blue) and rich (red) periods

. The data and model show that the conversion rate of N_2O from NO_x is significantly dependent on exhaust temperature. It is interesting to see that the lean and rich data collapsed into a single curve, which shows an inversely proportional relationship with temperature. It is good to see that the model fits the curve very well. The model and data also indicate that N_2O formation favors at low temperatures either at lean or rich, which was also observed by other researchers [39].

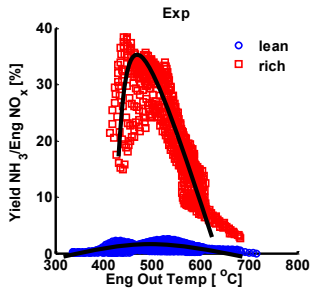

Figure 3-20: Comparison of time-averaged αNH_3 at lean (blue) and rich (red) periods

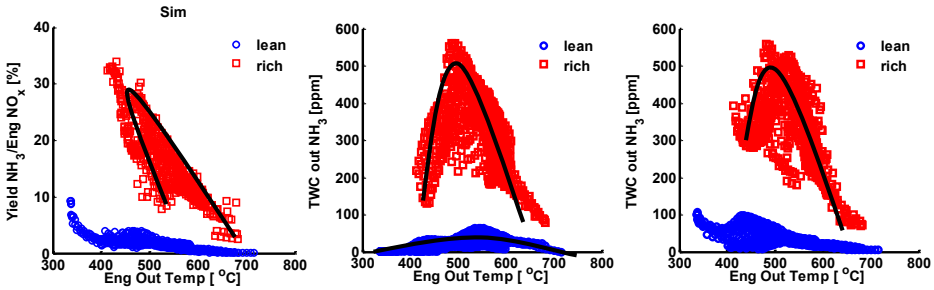

Figure 3-21: Comparison of time-averaged NH_3 (ppm) at lean (blue) and rich (red) periods

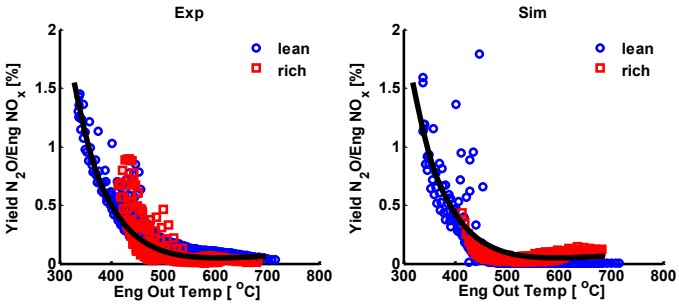

Figure 3-22: Comparison of time-averaged αN_2O at lean (blue) and rich (red) periods

www.manaraa.com

3.3.3 Transient FTP Cycle Results

TWC performance at cold start conditions is very critical and important. Therefore, transient data of FTP drive cycle with cold start were selected to further validate the TWC model, especially NH_3 and N_2O kinetics.

The TWC wall temperature comparison is shown in Figure 3-23. The model matches the data in the first 400 seconds. After 400 seconds, the peaks of wall temperature are captured by the model even though the predictions are slightly higher.

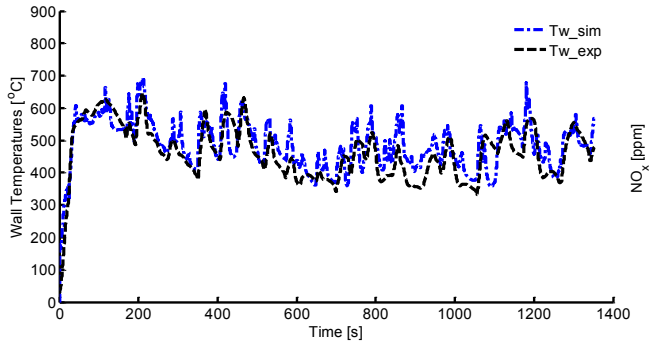

Figure 3-23: TWC wall temperature comparison under FTP cold cycle

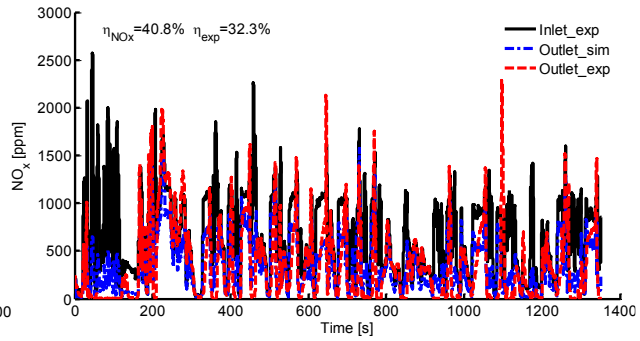

Figure 3-24: NO_x comparison under FTP cold cycle

NO_x emission at TWC outlet is higher than the data in the first 200 seconds, which is shown in Figure 3-24. This might be due to some NO_x absorption functionality designed in the TWC devices for high conversion rate of NO_x at cold start conditions, which was not modeled in current kinetics. It also might be specially commanded AFR adjustments during the first 200 seconds. Basically, the model gives a good prediction of NO_x with an overall conversion rate of 40.8% compared to 32.3% from the data.

NH_3 and N_2O comparisons are shown in Figure F 5 and Figure F 6 in Appendix F. In Figure F 5, at the first 200 seconds, the model shows moderately high NH_3, which was not observed from

www.manaraa.com

experiments. After 200 seconds, predicted NH_3 matches the data and captures the NH_3 peaks. In Figure F 6, higher N_2O is predicted at the first 400 seconds. At the first 50 seconds, very high N_2O was observed from the data because of low exhaust temperatures. Unfortunately, the model did not capture the N_2O peaks in the middle of cycle very well. This might be due to the incompleteness of the N_2O kinetics.

3.4 LNT kinetics modeling

The LNT kinetics used in this study involves CO, H_2 and hydrocarbons oxidation, NO and NO_2 conversion, NO reduction by CO and hydrocarbon, NO_x absorption and desorption, NH_3 and N_2O kinetics. The reaction rates were taken from Olsson's global LNT kinetic model [125,126] and were calibrated based on the experimental data. The global LNT reactions considered in this study as well as the reaction rate constants are shown in Appendix D.

Time-resolved steady state data were used to validate the LNT model. Experimental data collected upstream of the LNT (downstream of the TWCs) were used as the inlet boundary conditions of the model. Model validations at 3500 RPM and 30% load are shown below. Predicted temperatures as well as exhaust species at catalyst outlet are compared with the measurements downstream of the LNT.

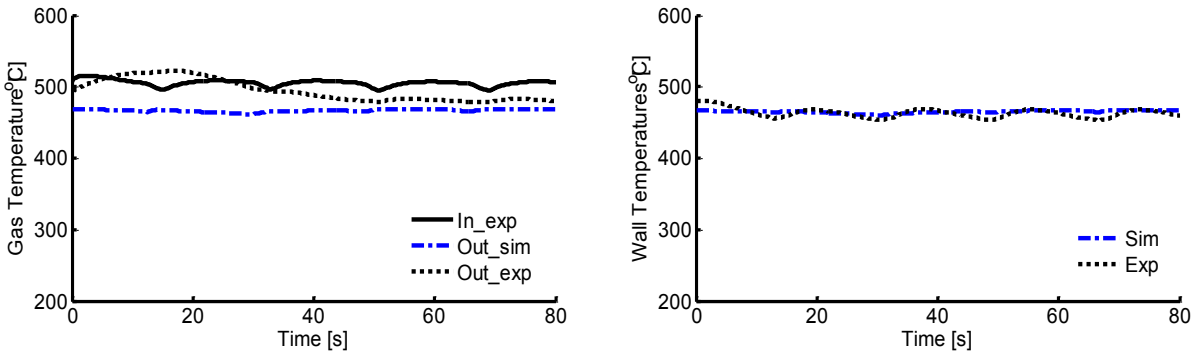

www.manaraa.com

Figure 3-25: LNT gas temperature comparison at 3500 rpm, 30% load

Figure 3-26: LNT wall temperature comparison at 3500 rpm, 30% load

Comparisons of gas temperature and catalyst temperature at the LNT outlet are shown in Figure 3-25 and Figure 3-26. The gas temperature at the LNT outlet is lower than the inlet temperature. This is probably due to limited exothermic reactions and relatively high heat transfer. Predicted gas temperature and catalyst temperature are fairly close to the data.

Predicted instantaneous NO_x at the LNT outlet is shown in Figure 3-27. NO_x is adsorbed or stored in the LNT at lean period, which is well captured. The amount of NO_x being stored is the integration of the differences between the inlet NO_x and outlet NO_x with time. When the engine is switched from lean to rich, a large amount of NO_x is released, which is well-known as NO_x breakthrough during lean to rich transition. Released NO_x is then converted to nitrogen and ammonia as a presence of reductants in the rich period, which is usually referred as LNT regeneration. NO_x release and reduction during rich period resulted in a sharp peak of NO_x in the LNT outlet, which is captured by the model as well even though the magnitude of the peak is larger than the experimental data. However, cumulative NO_x matches the data very well, which is shown in Figure 3-28.

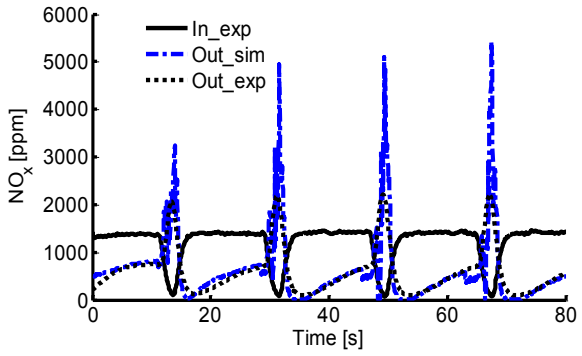

Figure 3-27: LNT NO_x comparison at 3500 rpm, 30% load

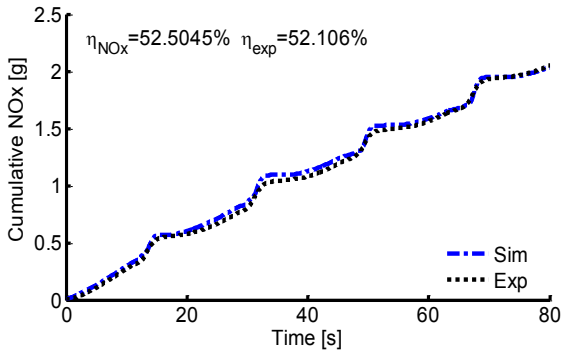

Figure 3-28: LNT cumulative NO_x comparison at 3500 rpm, 30% load

www.manaraa.com

Comparisons of instantaneous and cumulative CO and total HCs are shown in Figure 3-29 to Figure 3-32. Most of CO and HCs are oxidized during lean periods due to excess oxygen, which can be seen in Figure 3-29 and Figure 3-31. During rich periods, a significant amount of CO is consumed during LNT regenerations. Even through there is some differences in the cumulative CO in Figure 3-30, the overall CO conversion rate is very comparable to the data. HC breakthroughs are observed during rich periods in Figure 3-31, which are not observed from the model. This phenomena may be due to some HC storage functionality in the LNT, which is not included in our model.

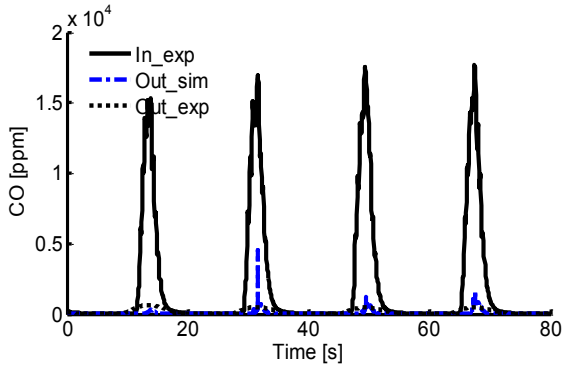

Figure 3-29: Instantaneous CO comparison at 3500 rpm, 30% load

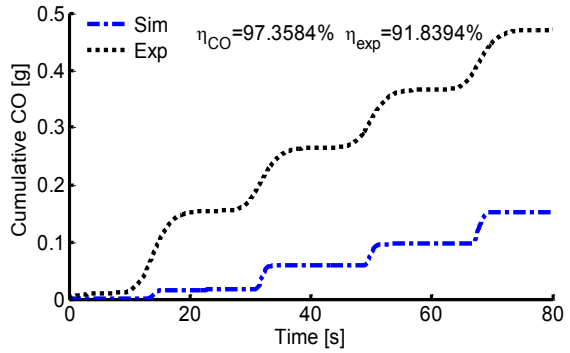

Figure 3-30: Cumulative CO comparison at 3500 rpm, 30% load

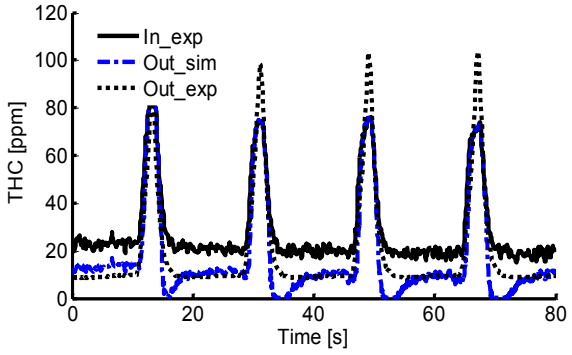

Figure 3-31: Instantaneous HCs comparison at 3500 rpm, 30% load

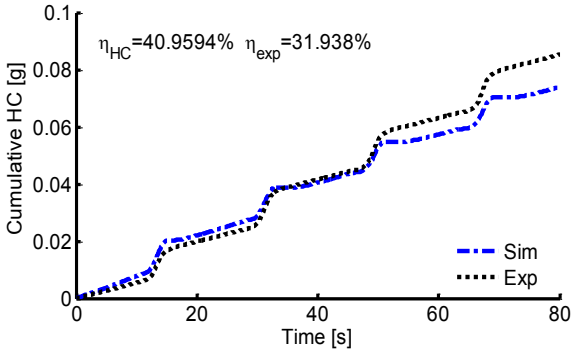

Figure 3-32: Cumulative HCs comparison at 3500 rpm, 30% load

www.manaraa.com

3.5 Pd-only TWC in a flow reactor

Experimental data collected on a flow bench reactor are more suitable for kinetics validations. In flow bench reactor experiments, temperature and species concentrations are well controlled. Moreover a switch between lean and rich is prompt, which is very useful to investigate transient performance of a catalyst therefore to help model development.

A fully automated furnace bench flow reactor with a Pd-only TWC catalyst was set up at ORNL. The TWC catalyst under study is a 1.3 liter catalyst combination with two formulations. The front 0.6L of the TWC is Pd only with high PGM loading (0/6.7/0 g/L Pt/Pd/Rh) and without ceria-based OSC. The rear 0.7L of the TWC is low PGM (0/1.1/0.3 g/L Pt/Pd/Rh) catalyst with ceria-based OSC. The catalyst was degreened for 16 hours at 700°C in humidified air (2.7% H2O).

In this study, only the front brick of the TWC catalyst was investigated due to its high capability of NH_3 generation over a wide range of temperatures. In order to isolate flow distribution and temperature gradients within the catalyst, a small sample from the front Pd-only catalyst is extracted for investigation. The sample is put into a quartz cube, which is shown in Figure 3-34.The dimensions of the catalyst sample are summarized in Table 3-5.

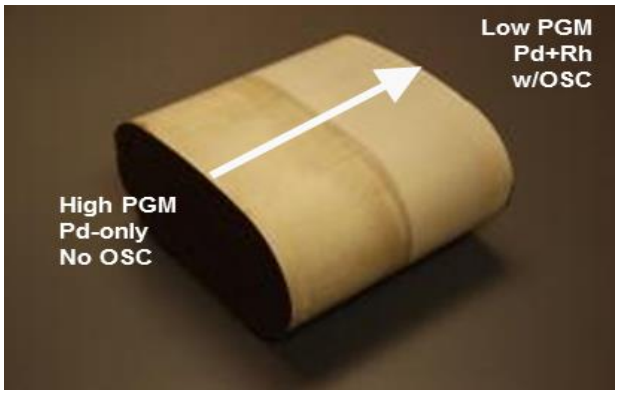

Figure 3-33: A 1.3L TWC with two formulations

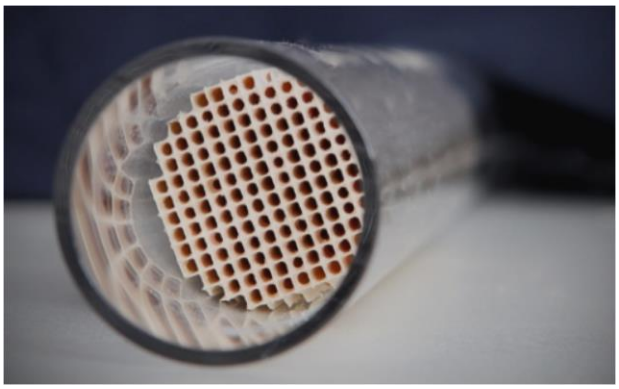

Figure 3-34: A sample of front brick of TWC in a quartz tube

www.manaraa.com

Table 3-5: Specification of the catalyst sample

Catalyst sample	Pd-only
PGM loading [g/ft^3]	190
Length [cm]	2.2cm
Diameter [cm]	2.0 cm
Cell density [cpsi]	600
Wall thickness [mm]	0.3

The catalyst temperature is swept from 250 to 600°C. A standard space velocity at all temperatures is maintained at 75K hour^{-1}. Oxygen concentration is changed corresponding to different air-fuel ratios (AFRs). The gas compositions for all the tests are shown in

Table 3-6.

Table 3-6: Feed-in gas composition

	Lean	Rich					
AFR	24	14.0	14.1	14.2	14.3	14.4	14.59
O_2 (%)	8	0.79	0.92	1.06	1.20	1.34	1.59
NO (ppm)	600	1200					
CO (%)	0	1.8					
H2 (%)	0	0.6					
C3H6 (%)	0	0.1					
H2O (%)	5	5					
CO_2 (%)	5	5					

3.5.1 Heat transfer modeling

Even though the experiments were conducted in a small scale TWC catalyst sample, heat transfer in the system may still need to be modeled. Schematic of temperature measurements is shown in Figure 3-35.

www.manaraa.com

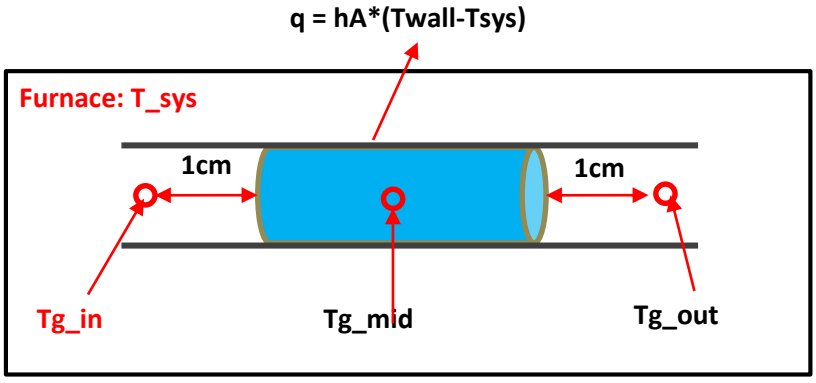

Figure 3-35: Schematic of temperature measurements

When inlet gas enters into the catalyst, the gas temperature will be increased resulting from exothermic reactions on the catalyst surface once the catalyst is light-off. On the other hand, gas may be cooled down through the rear part of the catalyst, which is not light-off. It can be found that gas temperature in the middle of the catalyst is 15 to 65 °C higher than the gas temperature at the outlet of the catalyst in Figure 3-36. This is because the rear portion of catalyst acts as a heat exchanger. Internal convection and conduction along the quartz tube are taken cared by the classic heat transfer correlations assuming laminar flow. There could be heat transfer from catalyst wall through quartz tube wall to the furnace due to conduction. Radiation from heating coil in the furnace could be significant as well.

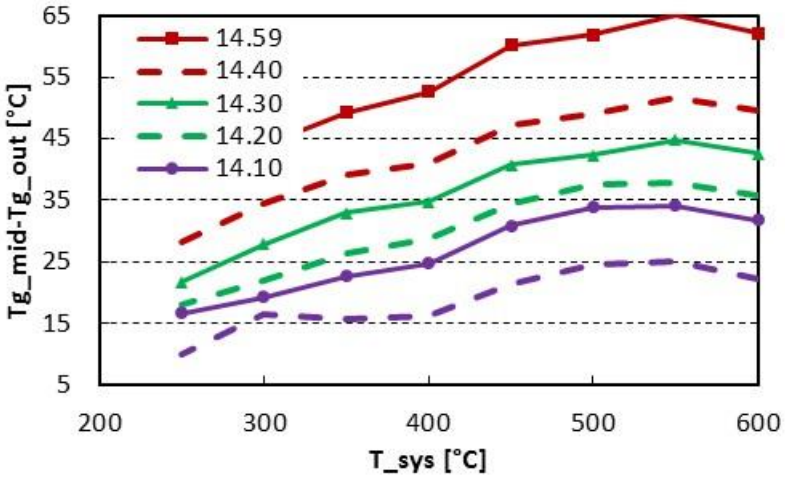

Figure 3-36: Differences between experimental gas temperatures in the middle and at the outlet of catalyst

www.manaraa.com

In order to have a simple heat transfer model, a combined heat transfer coefficient including convection and radiation is used to model the heat transfer from gas through quartz wall to the environment. Assuming an air velocity of 1 cm/s, a convection heat transfer coefficient is given at about 1 W/m^2-K from Zhukauskas's convective correlation [121]. Combined heat transfer coefficients at different surface temperatures are shown in Figure 3-37. It is found that radiative heat transfer is dominant. In TWC simulations, the combined heat transfer coefficient is given at 20 W/m^2-K, which is an average value in the temperature window between 250 and 600°C.

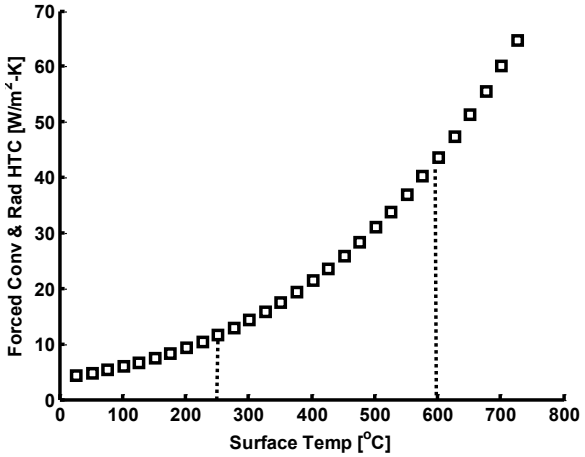

Figure 3-37: Combined convective and radiative heat transfer coefficients at different surface temperatures

3.5.2 TWC kinetics validation

Previous TWC kinetics calibrated by the engine dynamometer data were first used to simulate the Pd-only TWC catalyst. It is expected that the Pd-only TWC catalyst may have different light-off temperatures as well as NH_3 generation capabilities. Three TWC kinetics including the one validated by engine dynamometer data were tested on the flow reactor Pd-only TWC catalyst. It can be seen that the kinetic model from Gong et al. [129] under-predicts the gas temperatures when TWC inlet temperature is less than 400°C. That is probably because of the temperature window of engine dynamometer data for kinetics validation is above 400°C. However, similar results are

www.manaraa.com

predicted compared to two other reference kinetics at high temperatures (T>400°C). Therefore, the TWC kinetic model developed on engine dynamometer needs to be re-calibrated in order to improve the light-off performance. Comparison between the previous TWC kinetics and re-calibrated kinetics for the Pd-only TWC catalyst is shown in the Appendix D. Generally, CO and HCs oxidation rate coefficients are adjusted to have high oxidation performance at relatively low temperatures.

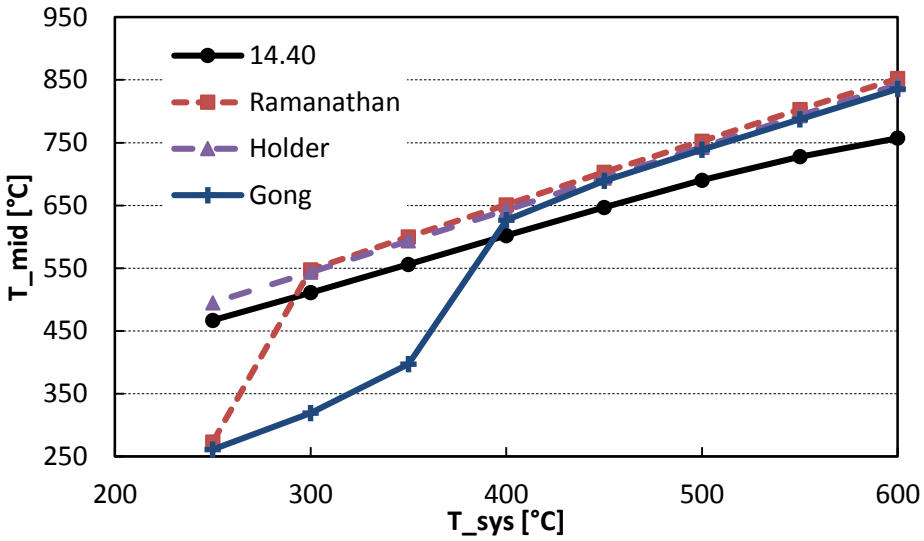

Figure 3-38: Temperature comparison of three TWC kinetics [127,128,129]

Based on the calibrated Pd-only TWC kinetics, calculated gas temperatures in the middle and at the outlet of the catalyst are compared to experimental measurements in Figure 3-39 and Figure 3-40. At 250°C, the gas temperatures are under-predicted, which is due to the limitation of kinetics at low temperatures. At high temperatures, the experimental temperatures in the middle of the catalyst shows consistent 15 to 65 °C higher than calculated temperatures. The differences are probably due to the use of a constant heat transfer coefficient.

www.manaraa.com

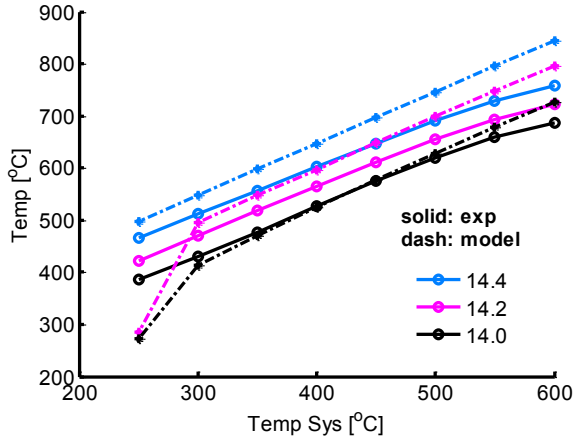

Figure 3-39: Gas temperature (middle) comparisons between model and data at different operating temperatures for three AFRs

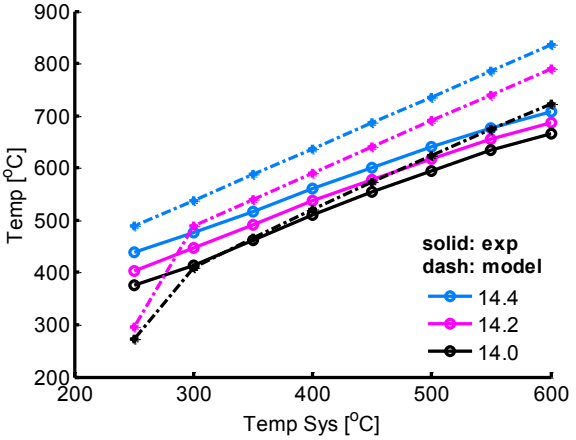

Figure 3-40: Gas temperature (outlet) comparisons between model and data at different operating temperatures for three AFRs

CO and HCs conversion efficiencies are shown in Figure 3-41 and Figure 3-42. Generally, the model well predicts the light-off performance of the catalyst. CO conversion efficiencies at 250°C and AFRs of 14.0 and 14.2 are under-predicted resulting in lower gas temperatures in Figure 3-39 and Figure 3-40. NO_x conversion efficiencies at all temperatures and AFRs are close to one, which are not shown.

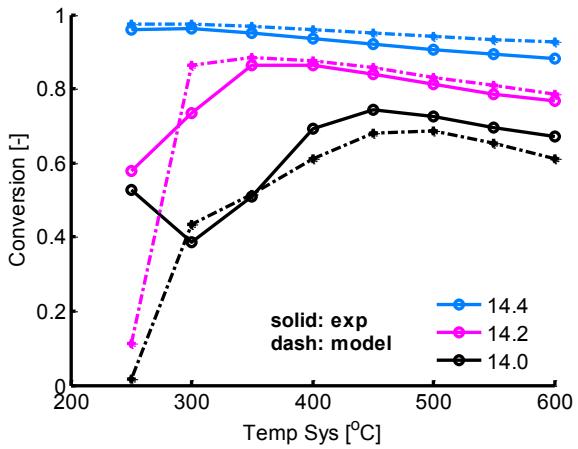

Figure 3-41: CO conversion efficiencies at different operating temperatures for three AFRs

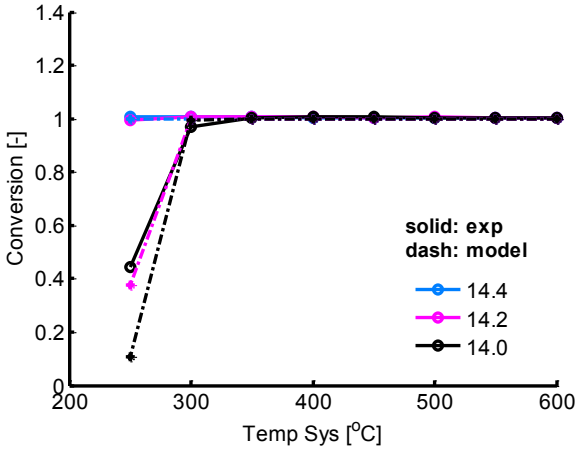

Figure 3-42: HCs conversion efficiencies at different operating temperatures for three AFRs

Hydrogen conversion efficiencies are shown in Figure 3-43. The model gives relatively high conversion efficiencies at slightly rich conditions (AFR =14.4) for all temperatures. However, lower hydrogen conversion efficiencies are observed at very rich condition (AFR = 14.0) when

www.manaraa.com

temperature is less than 400°C. As temperature is higher than 400°C, water-gas-shift and steam reforming reactions become active and a great amount of hydrogen is generated, which is observed by the model.

Ammonia generation efficiencies from the model are compared with experimental data in Figure 3-44. At relatively rich conditions (AFR = 14.2), ammonia generation efficiency peaks at around 400°C and starts to decrease as temperature increases further. This trend is well predicted by the model. However, the highest ammonia generation rate is about 80% compared to 100% from experimental data at the richest condition (AFR=14.0). It is found that the differences are not due to un-availability of hydrogen but the selectivity of NO_x reduction. The NO_x can be selectively reducted to ammonia or nitrogen.

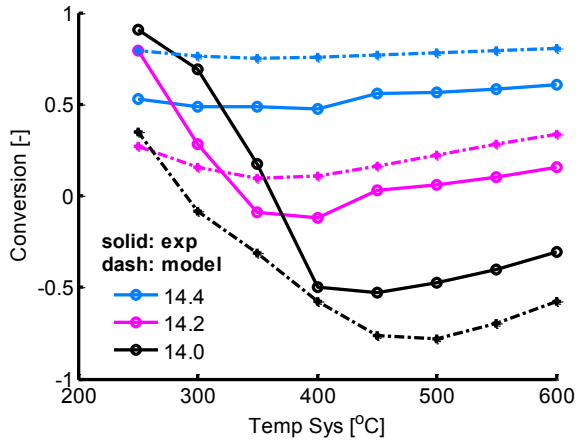

Figure 3-43: H_2 conversion efficiencies at different operating temperatures for three AFRs

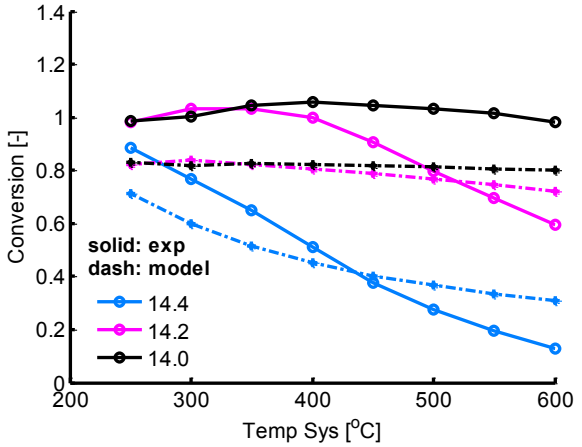

Figure 3-44: NH_3 conversion efficiencies at different operating temperatures for three AFRs

3.6 Summary

A TWC and a LNT model were developed based on the engine dynamometer data collected on a SIDI gasoline engine. Ammonia and N_2O kinetics were included in the TWC model. The TWC model was first calibrated by time-resolved experimental data and validated by a large set of time-

www.manaraa.com

averaged steady state data and real world driving cycles. It was found the TWC model is able to predict the performance of the TWC in a wide range of exhaust conditions with reasonable accuracy.

The TWC kinetics from the engine dynamometer were calibrated for a Pd-only TWC, which has better light-off performance. There are good agreements of CO, HCs and NO_x conversion between the model and experiments. It was found that ammonia formation is limited by selective reduction of NO_x, which needs to be further investigated.

www.manaraa.com

Chapter 4 - Ammonia SCR Kinetics Modeling

In this Chapter, a global SCR kinetic model is developed based on the experimental SCR protocol designed at ORNL.

The catalyst for SCR studies is a small pore Cu-Chabazite (CHA) NH_3-SCR catalyst, which was supplied by BASF Corporation. The catalyst is a 100% ion exchanged Cu chabazite containing 2.8% copper [130]. The exchanged zeolite was coated on a cordierite ceramic honeycomb substrate. The specification of the Cu SCR catalyst is shown in Table 4-1.

Table 4-1: Specification of a SCR catalyst sample

Catalyst sample	BASF Cu zeolite
Length [cm]	5.0 cm
Diameter [cm]	2.0 cm
Cell density [cpsi]	300
Number of channels in the sample [-]	121
Cell width [mm]	1.5
Wall +washcoat thickness [mm]	0.3

In order to study SCR performance, a small core samples was extracted from SCR catalyst brick. Experiments were performed at ORNL in a laboratory fixed flow bench reactor system, which is similar to that used for Pd-only TWC catalyst studies. The catalyst was located in a position inside the heated zone of the furnace so as to achieve a near-isothermal condition.

Table 4-2: A global SCR kinetic model

No.	*Reaction*	*Description*
1	$S+NH_3 \rightarrow SNH_3$	NH_3 adsorption
2	$SNH_3 \rightarrow S+NH_3$	NH_3 desorption
3	$4NH_3+3O_2 \rightarrow 2N_2+6H_2O$	NH_3 oxidation
4	$2NO+O_2 \leftrightarrow 2NO_2$	NO oxidation
5	$4SNH_3+4NO+O2 \rightarrow 4N_2+6H2O+4S$	Standard SCR
6	$2SNH_3+NO+NO2 \rightarrow 2N_2+3H2O+2S$	Fast SCR
7	$4SNH_3+3NO_2 \rightarrow 3.5N_2+6H2O+4S$	NO_2 SCR
8	$2SNH_3+2NO_2 \rightarrow N_2O+N_2+3H2O+2S$	N_2O formation

www.manaraa.com

A global SCR kinetic model based on Olsson's work [77] is described in Table 4-2. The SCR model has 8 reactions including ammonia storage, ammonia oxidation, NO oxidation, three SCR reactions (standard SCR, fast SCR and NO_2 SCR) and N_2O formation.

4.1 Experimental SCR protocol

A SCR reactor experimental protocol to measure the key catalyst properties that control SCR NO_x conversion performance was developed at ORNL. The isothermal protocol consists of a series of step changes in inlet gas composition designed to measure reaction rates and NH_3 inventories under SCR operating conditions.

Table 4-3: The isothermal SCR protocol

Step	Description	NH_3 (ppm)	NO (ppm)	NO_2 (ppm)	O_2 (%)	T (°C)
1.0	cool	0	0	0	10	600→400
1.1	NH_3 storage	350	0	0	0	400
1.2	NH_3 oxidation	350	0	0	10	400
1.3	NH_3 inventory/NO oxidation	0	350	0	10	400
1.4	NO SCR	350	350	0	10	400
1.5	NO SCR NH_3 inventory	0	350	0	10	400
1.6	start NO_2	0	175	175	10	400
1.7	NO+NO_2 SCR	350	175	175	10	400
1.8	NO+NO_2 SCR NH_3 inventory	0	175	175	10	400
1.9	NO_2 decomposition	0	0	263	10	400
1.10	NO_2 SCR	350	0	263	10	400
1.11	NO_2 SCR NH_3 inventory	0	0	263	10	400
1.12	NO+NO_2 clean	0	175	175	10	400
2.1	cool	0	0	0	10	400→350
…	repeat i.1-i.13 for all Ts					350…150

Space velocity (SV) is 60,000 $hour^{-1}$ in all the tests. The space velocity is defined as the total gas flow rate at standard conditions (1 atom and 273 K) divided by the total monolith volume. The core sample was hydrothermally degreened at 700 °C for 4 hours in humidified air (~10% H_2O, 20% O_2, balance N_2) in a laboratory furnace.

www.manaraa.com

Table 4-3 depicts the changes in inlet composition for a single run of the isothermal protocol. Figure 4-1 shows the detailed composition for each step in the protocol. Each step in the protocol was allowed to run until the outlet gas concentrations reached a steady state. 5% H_2O was maintained in all steps. There are 12 steps in a single run of the isothermal protocol.

The isothermal SCR protocol was conducted over a range of temperatures (150 to 400 °C) at ORNL. The NH_3 storage section of the protocol began in step 1.1 with NH_3 uptake measured in the absence of O_2 and NO_x. This step yielded a measurement of the total NH_3 storage capacity while avoiding the complications introduced by NH_3 oxidation. The rate of NH_3 oxidation was measured in step 1.2 after O_2 was turned on. NO was turned on in step 1.3. Integrating the NO_x reduced by the NH_3 stored on the catalyst during this step yielded a measure of the NH_3 inventory under SCR conditions. Standard SCR, fast SCR and slow SCR reactions were examined from step 1.4 to step 1.11. The protocol was repeated at different operating temperatures.

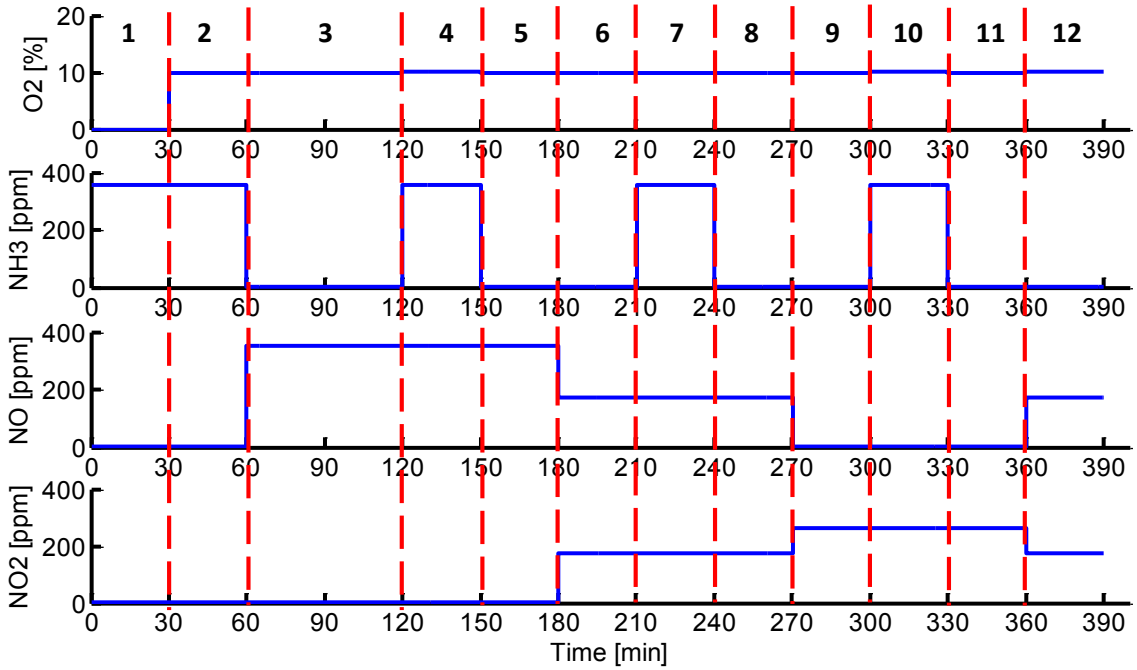

Figure 4-1: Composition for each step in the SCR protocol

www.manaraa.com

4.2 SCR storage modeling

The accurate description of NH3 adsorption/desorption from the catalyst surface is the basis for the correct description of the NH3-SCR performance. NH_3 adsorption and desorption will strongly affect the transient behavior of NO_x reduction. Therefore, a one site NH_3 storage model is developed to model the NH_3 adsorption and desorption characteristics. NH_3 adsorption site is denoted as "S" in SCR reactions. The catalyst active site density is fitted from the ammonia temperature programmed desorption (TPD) experiments.

4.2.1 Ammonia TPD experiments

In ammonia TPD experiments, a SCR catalyst was exposed to 350 ppm or 420 ppm NH_3 and 5% H_2O for about 70 minutes at 150 °C and followed by a temperature ramp for about 80 minutes.

TPD experiments were conducted to calibrate the NH_3 storage model. The TPD experiments began with an NH_3 adsorption step, which consisted of a stepwise increase in NH_3 concentration (from 0 to 350 or 420 ppm) while the catalyst temperature was held constant at 150°C. After the catalyst was saturated with NH_3 (as evidenced by a steady state outlet concentration equal to the inlet concentration), the flow of NH_3 was shut off. At this point, the catalyst was held at the 150°C while NH_3 isothermally desorbed. When the outlet NH_3 concentration dropped below 5 ppm (indicate the end of isothermal desorption), the catalyst temperature was increased to 550 °C at a rate of 5 °C min^{-1}. One of the ammonia TPD experiments is shown in Figure 4-2.

www.manaraa.com

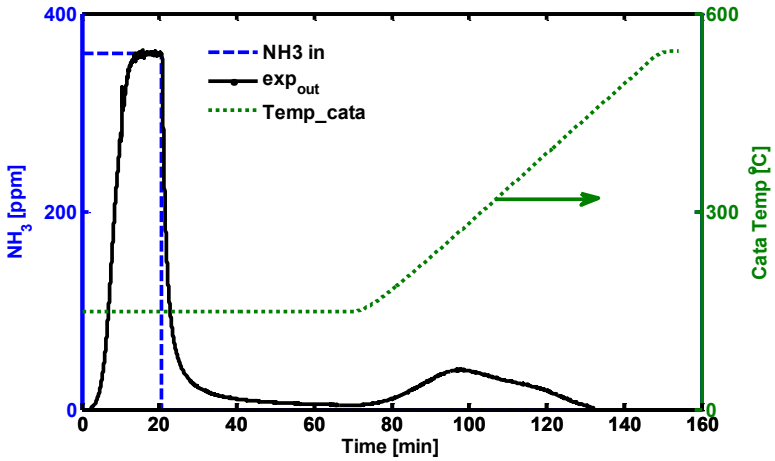

Figure 4-2: Ammonia TPD experiment (NH_3=350 ppm)

Assuming a non-activated adsorption rate constant [77,131], an adsorption rate express can be given by Eq. 4-1.

$$RR_{ad} = A_{ad} \cdot c_{NH3} \cdot (1 - \theta) \qquad \textit{Eq. 4-1}$$

Here θ is the coverage of NH_3 storage on the catalyst surface. A coverage dependent activation energy is used in Eq. 4-2 for ammonia desorption, which has been used in several other models for a desorption step [131,132,133].

$$RR_{de} = A_{de} \cdot \exp\left[-\frac{Ea_{de}(1 - \epsilon_{cat} \cdot \theta)}{RT}\right] \cdot \theta \qquad \textit{Eq. 4-2}$$

Here ϵ_{cat} is a model constant. It determines the dependence of desorption activation energy Ea_{de} on NH_3 coverage θ. From adsorption and desorption reaction rates, the amount of NH_3 being adsorbed can be calculated as:

$$C_{NH3,abs,cal} = \Omega_{cat} \cdot \theta_{eq} \qquad \textit{Eq. 4-3}$$

where the equilibrium NH_3 coverage θ_{eq} is obtained from $\frac{d\theta_{eq}}{dt} = RR_{ad} - RR_{de} = 0$. Here Ω_{cat} is the active site density of the catalyst.

www.manaraa.com

On the other hand, the amount of NH_3 being adsorbed from experiments can be calculated from Eq. 4-4.

$$C_{NH3,abs,exp} = \int (x_{NH3,in} - x_{NH3,out}) \cdot SV \cdot \frac{P}{R_u T} dt \qquad \textit{Eq. 4-4}$$

The active site density of the catalyst can be calibrated from ammonia TPD experiments and it turns out to be 250 mole/m^3.

The outlet NH_3 concentrations from the NH_3 TPD experiment (inlet NH_3 =150 ppm) and simulation are presented in Figure 4-3. There is a total uptake of ammonia for about 2 minutes and thereafter the ammonia starts to increase. The increase is slower experimentally and this might be explained by a slower adsorption when the catalyst is close to saturation. The experimental data shows slightly NH_3 breakthrough when the catalyst is saturated with NH_3. Cumulative ammonia adsorptions between the model and experiment are shown Figure 4-4. The model gives very similar ammonia adsorption characteristics compared to the experiment and the total amount of ammonia adsorbed is the same to the experimental value. After the adsorption period, catalyst temperature is increasing from 150 °C to 550 °C. An ammonia desorption peak is observed at about 270 °C. It seems that there is a second weak ammonia desorption peak around 340 °C and a large overlap between the two peaks. The second desorption at relatively high temperature indicates that some of ammonia is strongly bonded with the surface site. Two ammonia desorption peaks were observed by Olsson et al. [77] on a Cu-ZSM-5 SCR catalyst. The model captures ammonia desorption and resulted in a flat ammonia desorption curve, even though the magnitude of desorption is slightly higher than the experiment. Desorption of ammonia is complete at 450 °C, which is predicted by the model as well. Generally, the ammonia storage model can describe the release of ammonia well due to the coverage dependent activation energy.

www.manaraa.com

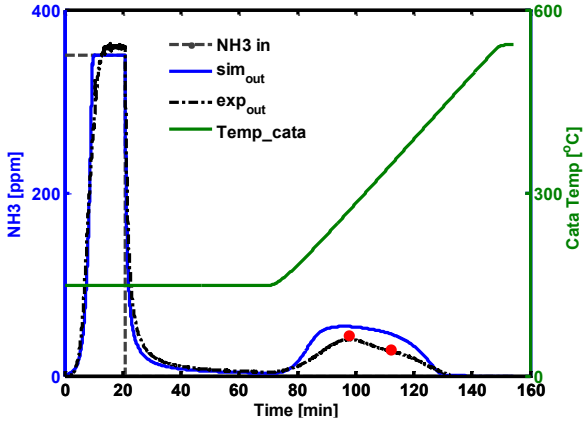

Figure 4-3: NH_3 storage model validation from NH_3 TPD experiment (NH_3= 350 ppm, T = 150, SV =60K hour^{-1})

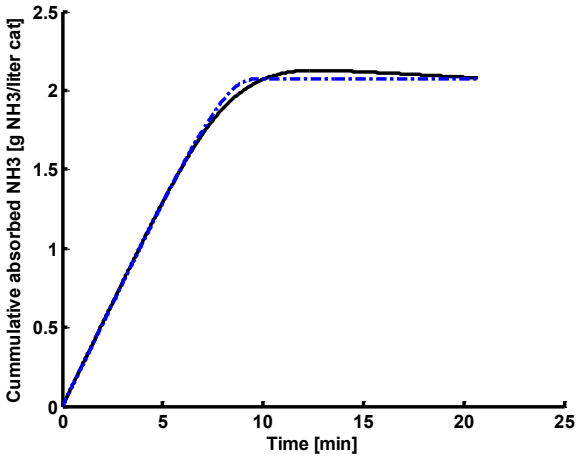

Figure 4-4: Comparison of cumulative adsorbed NH_3 (NH_3= 350 ppm, T = 150, SV =60K hour^{-1})

The storage model is validated by another ammonia TPD experiment with 420 ppm NH_3 at the inlet in Figure 4-5 and Figure 4-6. Similar results are observed.

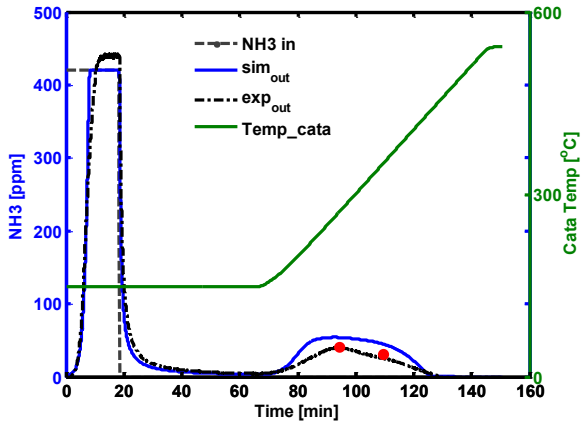

Figure 4-5: NH_3 storage model validation from NH_3 TPD experiment (NH_3= 4200 ppm, T = 150, SV =60K hour^{-1})

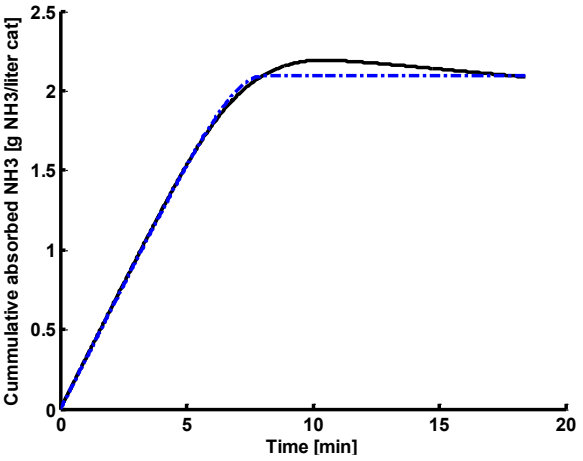

Figure 4-6: Comparison of cumulative adsorbed NH_3 (NH_3= 4200 ppm, T = 150, SV =60K hour^{-1})

4.2.2 Ammonia storage at different temperatures

The ammonia storage model was validated by the ammonia TPD experiments at 150°C at two different inlet ammonia concentrations in the previous section. It is important to check ammonia storage capacity at different temperatures since our objective is to develop a SCR model at a wide

www.manaraa.com

range of exhaust conditions. Therefore, ammonia adsorption experiments were conducted at different temperatures from 150°C to 400°C with an inlet ammonia concentration of 350 ppm. The outlet ammonia concentration and cumulative adsorbed ammonia are shown in Figure 4-7 and Figure 4-8.

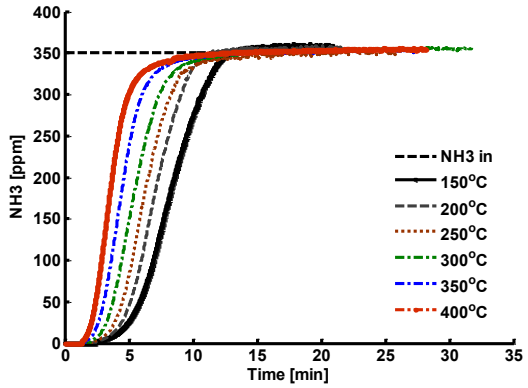

Figure 4-7: Outlet ammonia concentration at temperatures from 150 to 400 °C

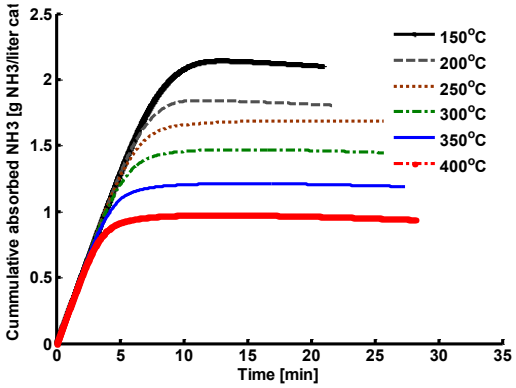

Figure 4-8: Cumulative adsorbed ammonia at temperatures from 150 to 400 °C

Using the storage model with calibrated kinetics, the comparison of the ammonia storage between the model and data is shown in Figure 4-9. Adsorbed ammonia from experiments decreases with temperature linearly. However, the model gives lower ammonia adsorptions at high temperatures, even though the relationship between the adsorbed ammonia and temperature is linear.

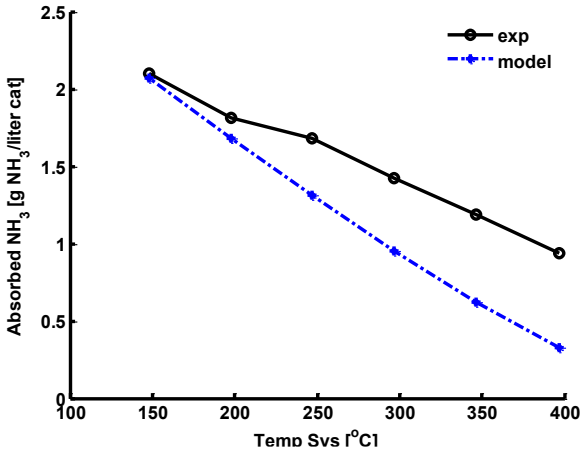

Figure 4-9: Comparison of ammonia storage at different temperatures with ϵ_{cat} of 0.73

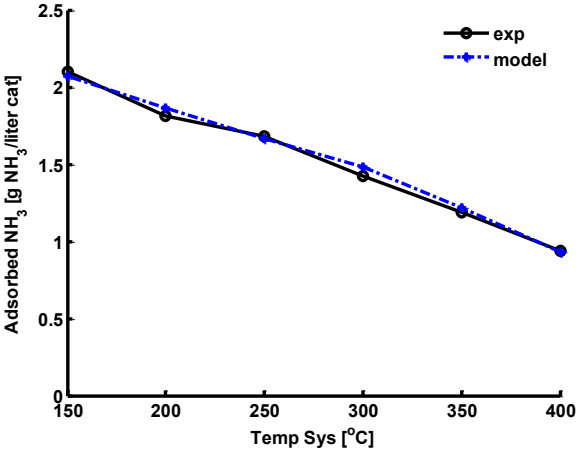

Figure 4-10: Comparison of ammonia storage at different temperature using calibrated ϵ_{cat}

www.manaraa.com

The differences indicate that the model gives a higher desorption rate (or a lower desorption activation energy) at a higher temperature resulted in less amount of ammonia adsorbed. Based on that, the model constant ϵ_{cat}, which determines the dependency of the desorption activation energy on ammonia coverage, is calibrated at different temperatures rather than using a constant value of 0.73. The calibrated ϵ_{cat} results in a low value of 0.07 at 400 °C and a high value of 0.73 at 150 °C. With ammonia coverage calculated at different temperatures, ϵ_{cat} shows a linear dependence with the ammonia coverage in Figure 4-11. As a result, the dependence of desorption activation energy on ammonia coverage is linear in Figure 4-12. Generally, Figure 4-12 indicates that desorption activation energy should be lower at low temperatures as more ammonia is adsorbed at the catalyst surface. At high temperatures, the amount of ammonia adsorbed on the catalyst surface is low. The small amount of ammonia is strongly bound and it is difficult to desorb from the storage site, which has a higher energy barrier for ammonia desorption. Using calibrated ϵ_{cat}, the model gives better predictions to ammonia storage at different temperatures in Figure 4-10.

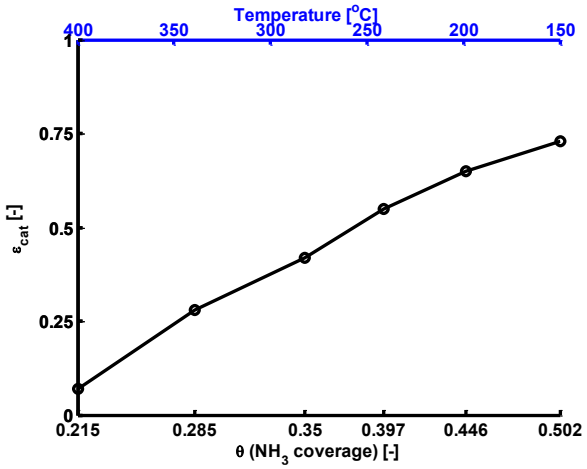

Figure 4-11: Calibrated model constant ϵ_{cat} at different temperatures

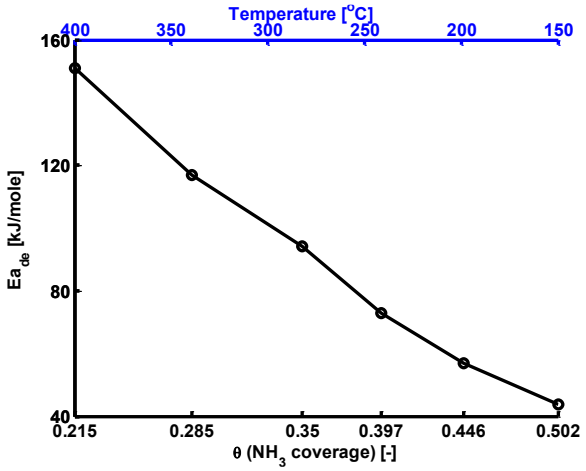

Figure 4-12: Desorption activation energy dependency on NH_3 coverage

4.3 Cu-zeolite NH_3 SCR kinetics modeling

www.manaraa.com

Ammonia storage (step 1.1) has been validated by the storage model in the previous section. In this section, each step in the experimental protocol will be discussed.

4.3.1 Ammonia oxidation

It was reported that Cu-zeolites selectively oxidize NH_3 to nitrogen when the temperature is below 500°C. At higher temperatures (T>500°C), NO was observed from oxidation of NH_3 [134].

However, selective NH_3 oxidation is not considered in this SCR model. Since the temperature window of SCR operation is below 500°C in this study, one reaction step is added for the ammonia oxidation. In this step, ammonia on the surface is reacting with oxygen to produce nitrogen and water.

$$RR_{NH3,oxi} = k_{NH3,oxi} \cdot C_{g,O2} \cdot \theta \qquad \textit{Eq. 4-5}$$

Step 1.2 in the experimental SCR protocol was simulated with inlet gas of 350 ppm or 420 ppm NH_3 and 10% of O_2. Comparisons of the NH_3 concentration between the model and experiment at two different inlet ammonia concentrations are shown in Figure 4-13 and Figure 4-14. The model describes NH_3 oxidation adequately by using one global reaction.

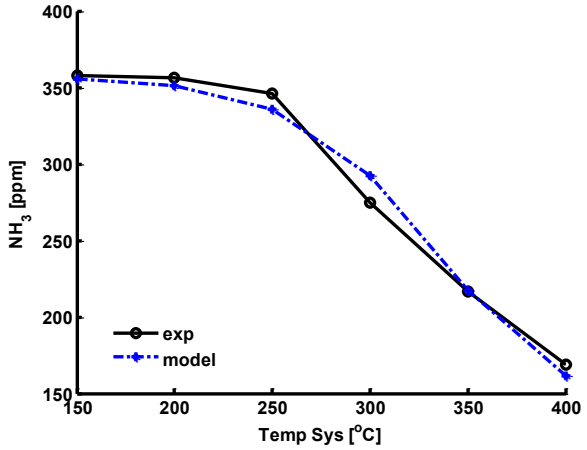

Figure 4-13: Outlet NH_3 concentration at different temperatures (Step 1.2: 350 ppm NH_3 and 10% O_2)

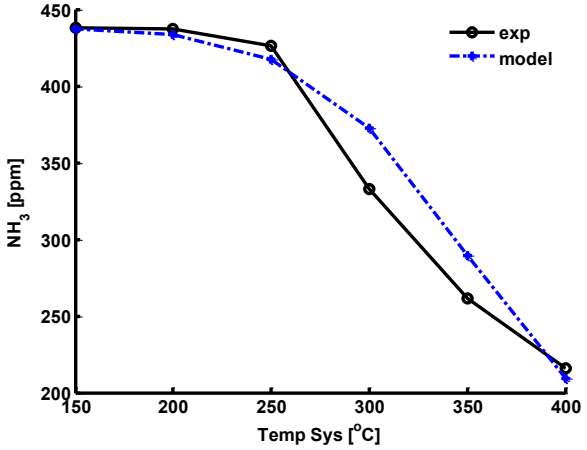

Figure 4-14: Outlet NH_3 concentration at different temperatures (Step 1.2: 420 ppm NH_3 and 10% O_2)

www.manaraa.com

4.3.2 NO oxidation

Describing the influence of changing NO/NO_2 ratio on ammonia SCR performance is important. Therefore, a NO oxidation step is included in the model as well. NO oxidation is a reversible reaction. At low temperatures, NO to NO_2 conversion is kinetically limited and NO_2 increases as temperature increases. NO_2 reaches its maximum at about 450°C and therefore starts to decrease due to thermodynamic constraints. The forward reaction rate of NO oxidation is determined by temperature and the backward rate is determined by the equilibrium constant.

$$RR_{NO,oxi} = k_{NO,oxi} \cdot (C_{g,NO} C_{g,O2}^{0.5} - \frac{C_{g,NO2}}{k_{eq}}) \qquad \textit{Eq. 4-6}$$

The equilibrium constant based on molar concentration is given by Eq. 4-7. Here $k_{p,eq}$ is the equilibrium constant based on partial pressure $k_{p,eq} = \exp\left(-\frac{\Delta G}{RT}\right)$, where ΔG is the Gibbs function with a definition of $\Delta G = \Delta H - T\Delta S$.

$$k_{eq} = k_{p,eq} \cdot \left(\frac{RT}{P}\right)^{0.5} \qquad \textit{Eq. 4-7}$$

NO oxidation kinetics are validated by simulating step 1.3 with inlet gas of 350 ppm NO. However, there are some NH_3 inventory on the catalyst surface. The model adequately captures the NO and NO_2 concentration at the catalyst outlet, which can be seen from Figure 4-15 and Figure 4-16.

www.manaraa.com

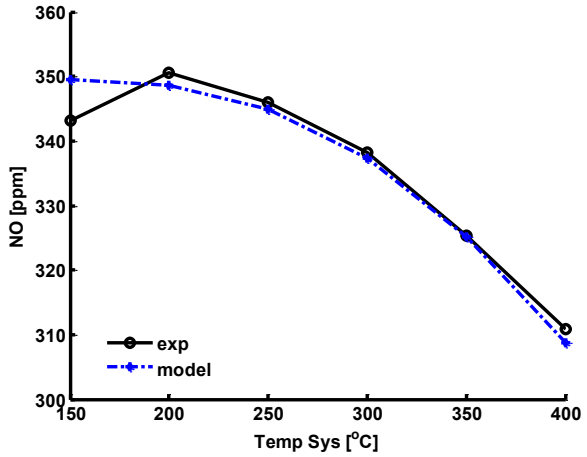

Figure 4-15: Outlet NO concentration at different temperatures (step 1.3: 350 ppm NH_3 and 10% O_2)

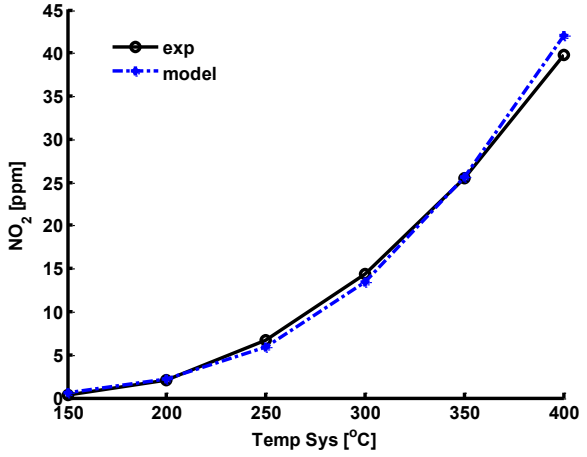

Figure 4-16: Outlet NO_2 concentration at different temperatures (step 1.3: 350 ppm NH_3 and 10% O_2)

4.3.3 NH_3 SCR kinetics modeling

Three reaction steps for SCR are added for three SCR processes including standard SCR with NO + O_2, fast SCR with NO + NO_2 and NO_2 SCR with NO_2. The reaction rates are shown in Eq. 4-8 to Eq. 4-10.

$$RR_{SCR,std} = k_{SCR,std} \cdot C_{g,NO} \cdot \theta \qquad \textit{Eq. 4-8}$$

$$RR_{SCR,fast} = k_{SCR,fast} \cdot C_{g,NO} \cdot C_{g,NO2} \cdot \theta \qquad \textit{Eq. 4-9}$$

$$RR_{SCR,NO2} = k_{SCR,NO2} \cdot C_{g,NO2} \cdot \theta \qquad \textit{Eq. 4-10}$$

The standard SCR is described by a rate that includes ammonia on surface and NO in the gas phase. FTIR studies have shown that the rapid SCR can not be explained by reactions between surface species alone and that gas phase NO is likely important [135]. Similarly, rapid SCR is modeled by a reaction between adsorbed ammonia, NO and NO_2. The NO_2 SCR reaction occurs between adsorbed NH_3 and gas phase NO_2 and this reaction is slower than both the standard and rapid SCR reactions.

$$RR_{SCR,N2O} = k_{SCR,N2O} \cdot C_{g,NO2} \cdot \theta \qquad \textit{Eq. 4-11}$$

www.manaraa.com

In addition, N_2O formation is also considered in the kinetics. It was reported that the N_2O production increases with NO_2 concentration, for most conditions [135]. Therefore, a N_2O formation reaction is modeled in Eq. 4-11, which is a competing step with Eq. 4-10. The reaction constants for all the reactions are shown in Table 4-4.

Table 4-4: Kinetic parameters of SCR model

No.	*Reaction*	*Rate constants*	*Pre-exponential*	*Activation energy (kJ/mole)*	*Notes*
1	$S+NH_3 \rightarrow SNH_3$	k_{ad}	1.5	0	NH_3 adsorption
2	$SNH_3 \rightarrow S+NH_3$	k_{de}	1.000E+11	162.18	NH_3 desorption
3	$4NH_3+3O_2 \rightarrow 2N_2+6H_2O$	$k_{NH3,oxi}$	2.200E+02	68	NH_3 oxidation
4	$2NO+O_2 \leftrightarrow 2NO_2$	$k_{NO,oxi}$	9.500E+01	48	NO oxidation
5	$4SNH_3+4NO+O2 \rightarrow 4N_2+6H2O+4S$	$k_{SCR,std}$	2.300E+08	84.9	Standard SCR
6	$2SNH_3+NO+NO2 \rightarrow 2N_2+3H2O+2S$	$k_{SCR,fast}$	1.900E+12	85.1	Fast SCR
7	$4SNH_3+3NO_2 \rightarrow 3.5N_2+6H2O+4S$	$k_{SCR,NO2}$	8.200E+09	110.03	NO_2 SCR
8	$2SNH_3+2NO_2 \rightarrow N_2O+N_2+3H2O+2S$	$k_{SCR,N2O}$	4.400E+06	80.3	N_2O formation

*note: the reaction constant is in the form of $k = A \cdot \exp\left(-\frac{E_a}{RT}\right)$

4.3.4 SCR reactions

Before calibrations of the three main SCR reactions, the NO_x conversion efficiencies at different temperatures for the three SCR reactions are shown in Figure 4-17. It is very clear that the "NO_2 SCR" shows totally different trend of NO_x conversion efficiency. The light-off temperature for "NO_2 SCR" is around 300 °C compared to 200 °C for the standard and fast SCRs. This indicates that the activation energy for the "NO_2 SCR" should be higher. Another observation from Figure 4-17 is relatively high NO_x conversion efficiencies at low temperatures. For instance, there is about 20% NO_x conversion efficiency at 150 °C, which is higher than that of standard and fast SCRs at the same temperature. The reason could be due to NO_2 adsorption and nitrates or nitrites formation on the catalytic surface resulted in lower NO_x out of the catalyst [136].

www.manaraa.com

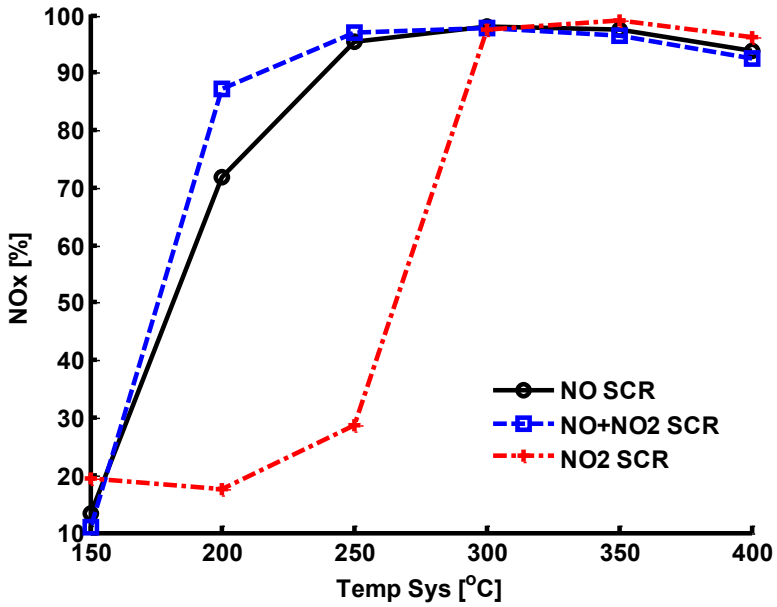

Figure 4-17: Comparison of deNO$_x$ efficiencies among three SCR reactions

Standard SCR

Step 1.4 in the experimental SCR protocol is the standard SCR step. 350 ppm NH_3 and 350 ppm NO are feed into the catalyst. The standard SCR step was simulated using the SCR kinetics discussed above. The amount of NH_3 at the catalyst outlet as well as total NO_x conversion efficiency are shown in Figure 4-18 and Figure 4-19. At all the test temperatures, NO reacts with NH_3 stoichiometrically. The NO_x conversion efficiency increases with temperature as expected. More than 90% conversion efficiency is observed when temperature is higher than 250°C. There are excellent agreement between the model and data.

www.manaraa.com

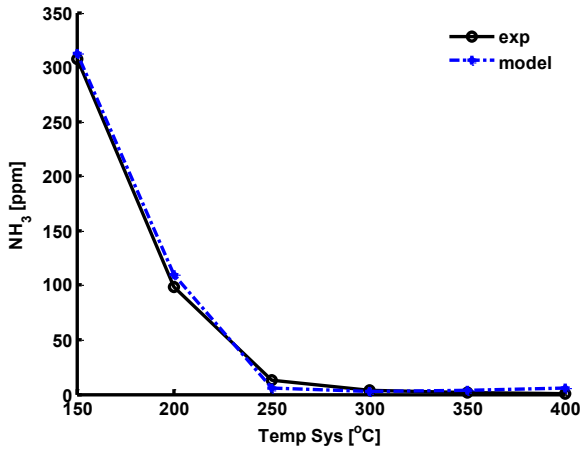

Figure 4-18: Outlet NH_3 concentrations at different temperatures (step 1.4: 350 ppm NH_3, 350 ppm NO and 10% O_2)

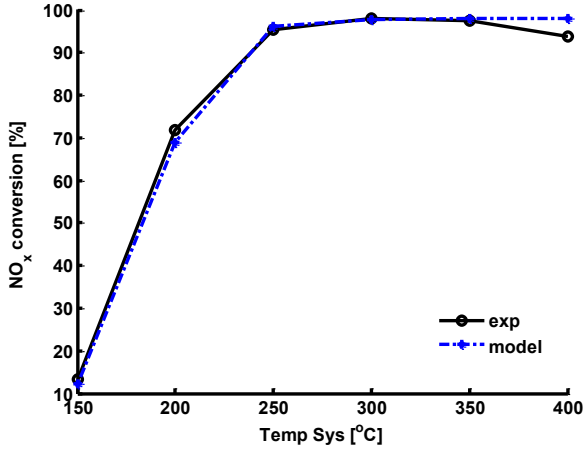

Figure 4-19: Total NO_x conversion efficiencies at different temperatures (step 1.4: 350 ppm NH_3, 350 ppm NO and 10% O_2)

Step 1.5 is NO oxidation and NH_3 inventory step, which is similar to step 1.3. Results from step 1.5 are similar to that of step 1.3 as well and therefore are not shown here.

At step 1.6, 175 ppm NO and 175 ppm NO_2 are feed into the catalyst. Since NH_3 inventory was cleaned by NO at the previous step, there is almost no SCR activities. The outlet concentration of NO and NO_2 are shown in Figure 4-20 and Figure 4-21. There is slightly NO oxidation as temperature increases to 350 °C. At 400 °C, the backward reaction starts to take effect and NO oxidation decreases.

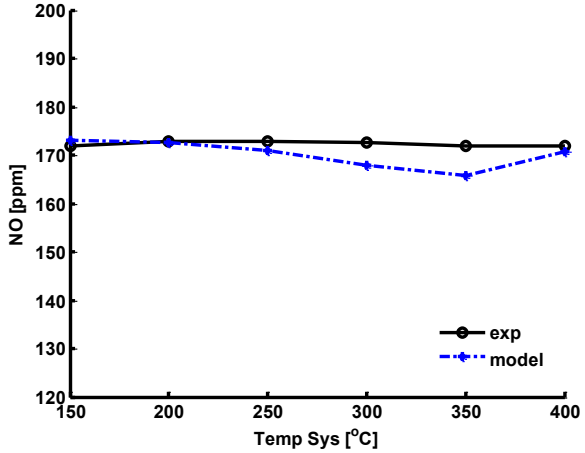

Figure 4-20: Outlet NO concentrations at different temperatures (step 1.6: 175 ppm NO, 175 ppm NO_2 and 10% O_2)

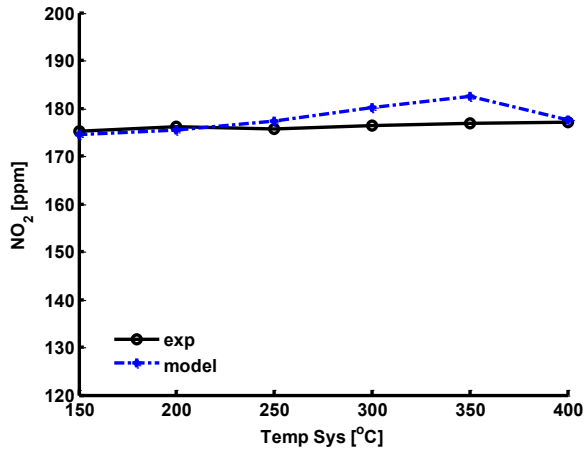

Figure 4-21: Outlet NO_2 concentrations at different temperatures (step 1.6: 175 ppm NO, 175 ppm NO_2 and 10% O_2)

www.manaraa.com

Fast SCR

For fast SCR reaction, the reaction rate is much faster compared to standard SCR reaction. Step 1.7 was simulated for the fast SCR. In Figure 4-22, more than 80% NO_x conversion efficiency is achieved when temperature is greater than 200°C. NH_3 and NO concentration decrease significantly at 200°C, which can be seen from Figure 4-23 and Figure 4-24. Fortunately, the model gives comparable NO_x and NH_3 conversion efficiencies even though the NO_2 concentration is slightly higher than the data. There is a large amount of NO_2 available from Figure 4-25. Low NO_x and NH_3 conversions may due to the non-availability of NO at high temperatures, which can be seen from Figure 4-24. However, the model gives 50% NO_x conversion compared to 10% from experiment at 150°C. This is due to the relatively high reaction rate when high concentration of ammonia storage in the catalyst surface is available.

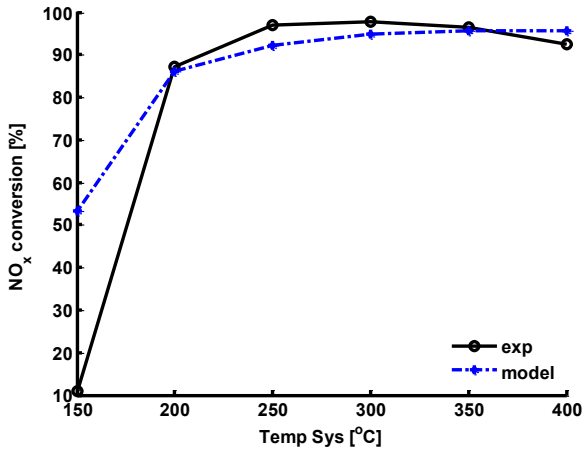

Figure 4-22: Total NO_x conversion efficiencies at different temperatures (step 1.7: 175 ppm NO, 175 ppm NO_2, 350 ppm NH_3 and 10% O_2)

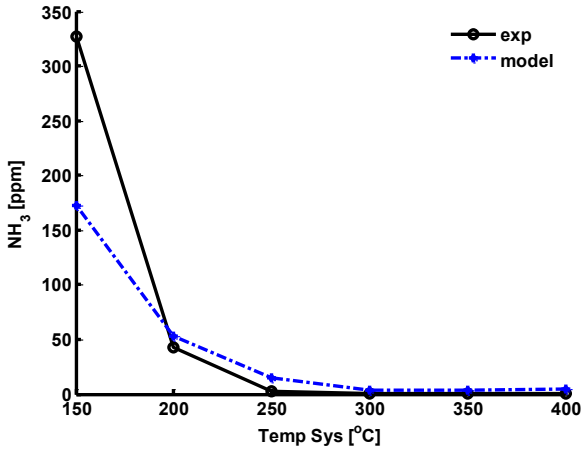

Figure 4-23: Outlet NH_3 concentrations at different temperatures (step 1.7: 175 ppm NO, 175 ppm NO_2, 350 ppm NH_3 and 10% O_2)

www.manaraa.com

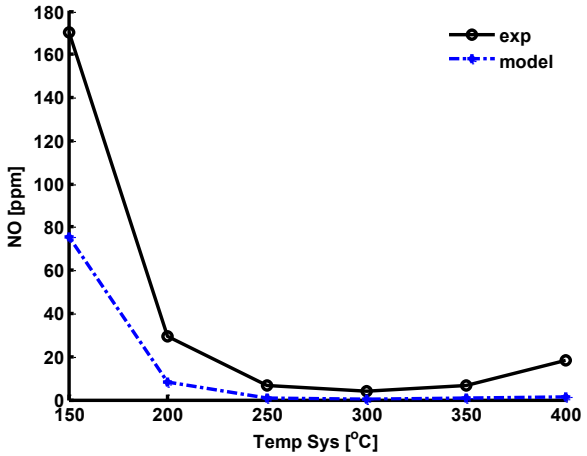

Figure 4-24: Outlet NO concentrations at different temperatures (step 1.7: 175 ppm NO, 175 ppm NO_2, 350 ppm NH_3 and 10% O_2)

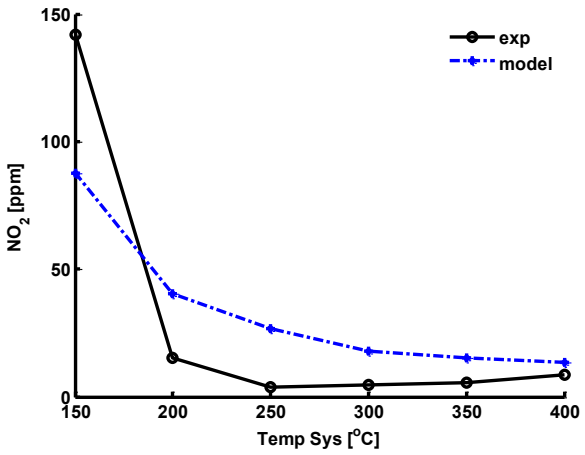

Figure 4-25: Outlet NO_2 concentration at different temperatures (step 1.7: 175 ppm NO, 175 ppm NO_2, 350 ppm NH_3 and 10% O_2)

Generally, it is difficult to calibrate the fast SCR to match the data since standard SCR and NO_2 SCR will occur when NO and NO_2 are both available. Therefore, the fast SCR step is the result of interactions among the three SCR reactions.

<u>NO_2 SCR</u>

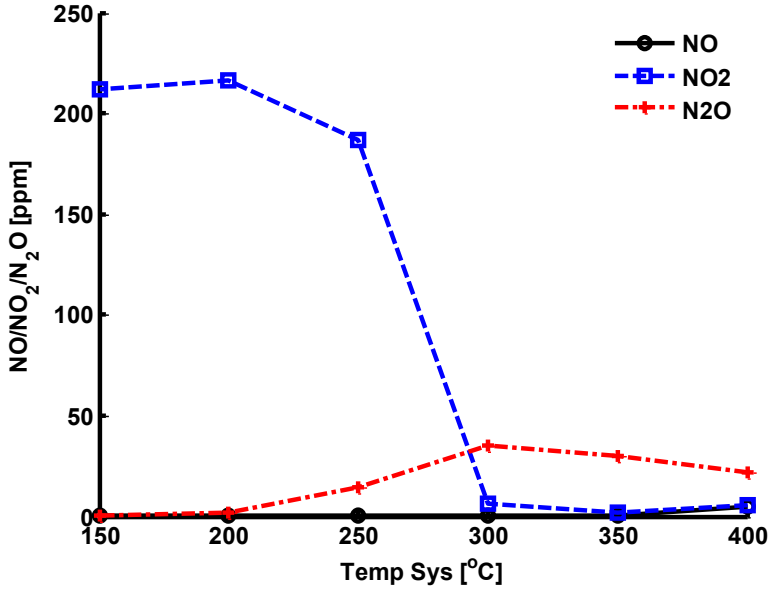

Figure 4-26: NO, NO_2 and N_2O concentration at the NO_2 SCR step

NO_2 SCR is very selective on this catalyst. In Figure 4-26, a large amount of N_2O can be formed at medium temperatures. That is why an additional N2O formation reaction needs to be modeled

www.manaraa.com

as discussed in Eq. 4-11. The N_2O selectivity depends on the characteristics of the catalyst and temperature as well, which makes the NO_2 SCR difficult to be calibrated.

NO_2 SCR reaction was studies by conducting simulation of step 1.10. There is a big jump of NO_x conversion efficiency from 250 °C to 300 °C in Figure 4-27. Similarly, NH_3 and NO_2 concentrations significantly decrease to almost zero when T>250°C, which can be seen from Figure 4-28 and Figure 4-29. The model gives relatively low NO_x conversation efficiencies at 150 ~ 200 °C, resulting in relatively high NO_2 at these temperatures. As discussed above, this could be due to the nitrates or nitrites formation, which is not modeled at all in the current model.

It seems that one NO_2-SCR mechanism in the model is unable to describe the NO_2-SCR performance. Other reactions, for instance nitrates formation, may need to be modeled to account for the experimental observations. However, the model shows reasonable agreement with the data over the whole range of exhaust conditions. The trend of N_2O concentration is generally captured as well by the model in Figure 4-30.

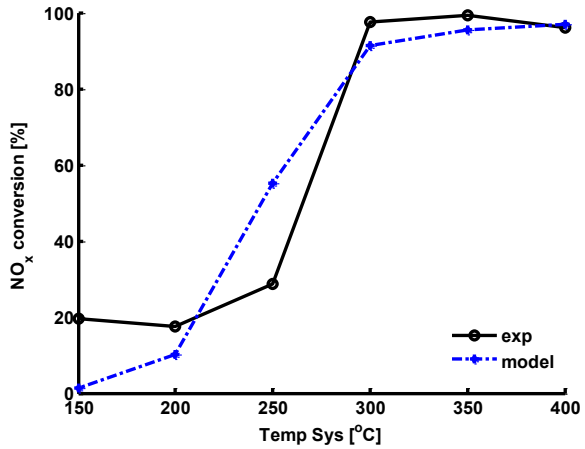

Figure 4-27: Total NO_x conversion efficiencies at different temperatures (step 1.10: 260 ppm NO_2, 350 ppm NH_3 and 10% O_2)

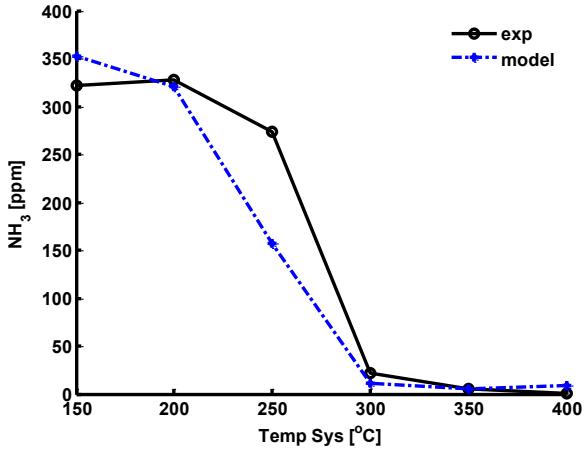

Figure 4-28: Outlet NH_3 concentrations at different temperatures (step 1.10: 260 ppm NO_2, 350 ppm NH_3 and 10% O_2)

www.manaraa.com

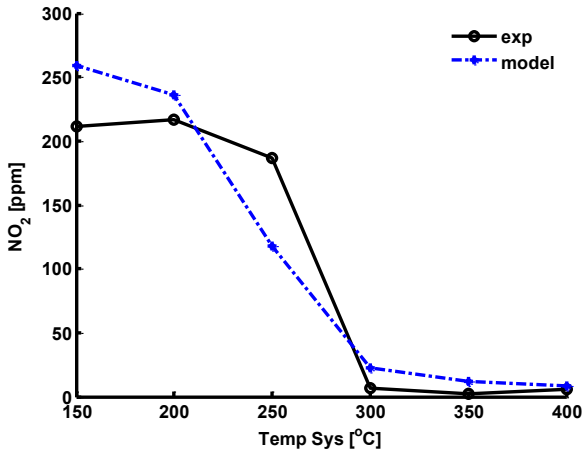

Figure 4-29: Outlet NO_2 concentration at different temperatures (step 1.10: 260 ppm NO_2, 350 ppm NH_3 and 10% O_2)

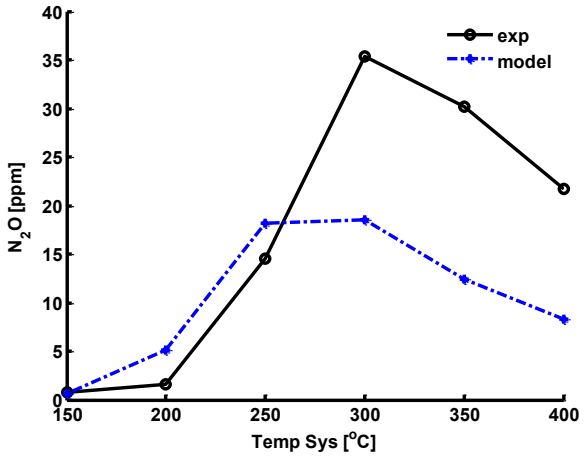

Figure 4-30: Outlet N_2O concentrations at different temperatures (step 1.10: 260 ppm NO_2, 350 ppm NH_3 and 10% O_2)

4.4 Summary

A global SCR kinetic model including ammonia storage, ammonia oxidation, NO oxidation, standard SCR, fast SCR, NO_2 SCR and N_2O formation was developed.

The ammonia storage model was investigated and calibrated from ammonia TPD experiments. A coverage dependent model constant was calibrated to represent the dependency of desorption activation energy on ammonia coverage. The storage model was found to be able to accurately predict the ammonia storage capacity at different temperatures. Each step in the experimental protocol was investigated to calibrate the SCR model. Generally, the SCR model gives good predictions of $DeNO_x$ performance over the temperature window in this study. The fast and NO_2 SCR may need further investigation to improve the model on NO_2 conversion.

www.manaraa.com

Chapter 5 - Particulate Filtration Modeling

In this chapter, a PDF based heterogeneous multi-scale filtration (HMF) model is developed to calculate filtration efficiency of particulate filters, which is motivated by modeling of gasoline particulate filters (GPFs). Several fundamental filtration experiments in the literature are selected for model validations [137,138,139]. A dynamic filtration model based on HMF is developed and validated by experiments from Exhaust Filtration System (EFA) [140] at Engine Research Center (ERC) at the University of Wisconsin-Madison. Finally, filtration characteristics of fuel neutral particulates are studied by using the dynamic HMF model.

5.1 Governing equations of particulate filter modeling

Modeling of the flow field in the particulate filter consists of two parts. The first part is modeling of the flow in the channels (inlet and outlet channels). On the filter channel scale, the flow distribution in the inlet and outlet channels can be solved by Navier Stokes equations. For the purpose of filtration modeling, the focus here will be on steady state, isothermal and non-reacting conditions. Therefore, only the one dimensional conservation equations of mass, momentum for alternatively plugged channels with porous wall are introduced here. The conservation equations of energy for the inlet and outlet channels and the porous wall can be found in [103, 141].

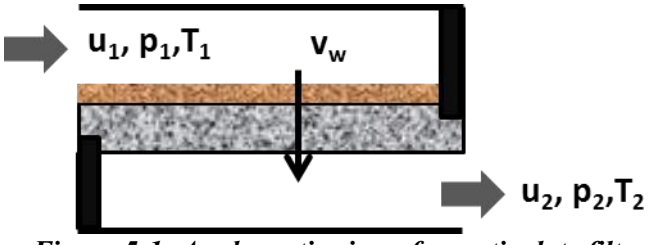

Figure 5-1: A schematic view of a particulate filter

The mass balance equation for gas flowing in the inlet and outlet channels is given by:

www.manaraa.com

$$\frac{\partial}{\partial x}(\rho_i u_i) = (-1)^i \cdot \left(\frac{4\rho_i v_w}{a}\right) \qquad \textit{Eq. 5-1}$$

where the subscript i refers to regions 1 (inlet channel) and 2 (outlet channel).

The momentum conservation equations in the inlet and outlet channels can be formulated as below:

$$\frac{\partial}{\partial x}(\rho_i u_i u_i) + \frac{\partial P_i}{\partial x} = -f \cdot \left(\frac{\mu u_i}{a^2}\right) \qquad \textit{Eq. 5-2}$$

Here f is a friction factor equivalent to 28.454 [103], and accounts for viscous effects on pressure loss.

Modeling of the pressure drop across the filter wall can give a relation for P_1 and P_2. The pressure drop across the porous wall can be given by Darcy's law [103,142,143].

$$\Delta P = P_1 - P_2 = \frac{\mu v_w w_s}{k_s} + \frac{\mu v_w w_w}{k_w} \qquad \textit{Eq. 5-3}$$

where k_s and k_w represent the permeability of the soot cake and the filter wall respectively. Here w_s and w_w are the thickness of the soot cake layer and the filter wall respectively.

The energy conservation equations for the inlet and outlet channels have the following form.

$$\left(C_{pi}\rho_i u_i\right)\frac{\partial T_i}{\partial x} = \frac{4}{a}(T_w - T_i) \cdot h_i + (-1)^i C_{pw}\rho_w v_w \cdot (T_w - T_i) \qquad \textit{Eq. 5-4}$$

where C_{pi} and C_{pw} are the specific heat of the gas and wall, T_i and T_w are the temperature of gas and wall. Here h_i is the heat transfer coefficient in the channel, which can be calculated from heat transfer correlations for square channels with suction flow [144].

The boundary and initial conditions for the mass, momentum and energy conservation equations as well as the numerical method for solving the conservation equations can be found in [145].

www.manaraa.com

5.1.1. Filtration modeling

As discussed in the previous section, the flow and temperature distributions can be obtained by solving the 1-D conservation equations. However, the flow field in the complicated porous filter wall is highly non-linear and difficult to be solved either numerically or analytically. Therefore, a filtration model is needed to model the particulate filtration process when the exhaust gas with particulates flow through the porous wall.

Specifically, some questions need to be answered by using the filtration model. For instance, what is the particulate number filtration efficiency, how much particulates are deposited insider or on the filter wall, how is the particulate distribution inside the filter wall and how the permeability changes with time? All these questions can be answered by developing a model of particulate size dependent total filtration efficiency $\eta(d_p)$.

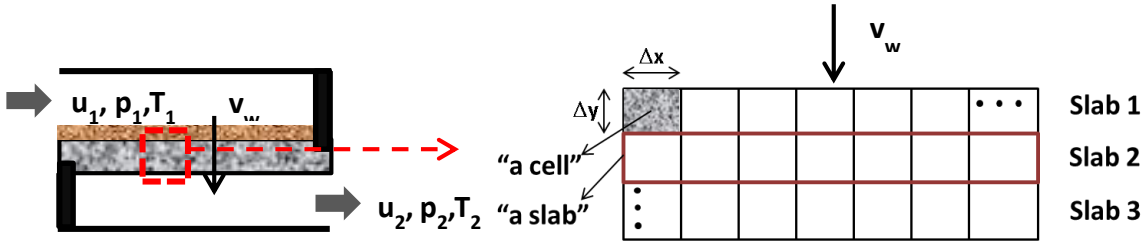

Figure 5-2: Discretization of a filter wall

Instead of apply the total filtration efficiency to the overall filter wall with a thickness of h, the filter wall is discretized into a number of slabs with a thickness of Δy. The schematic diagram of the discretized filter wall is shown in Figure 5-2.

At the beginning of the filtration, most soot particulates are depositing inside the filter wall. A partition coefficient ϕ_t is employed to determine the fraction of total upstream of particulates

www.manaraa.com

depositing on the surface of the filter wall. The definition of the partition coefficient is show in Eq. 5-5.

$$\phi_t = \frac{d_{c,t}^2 - d_{c0}^2}{(\psi b)^2 - d_{c0}^2} \qquad \textit{Eq. 5-5}$$

where ψ is a percolation factor between 0 and 1. It determines the degree of collector size can be reached before the end of "deep-bed" filtration. Here b is the diameter of a "unit cell", which can be calculated from the collector size and porosity.

By employing the percolation factor, the number of particulates at each diameter in the first slab can be calculated as:

$$PN(d_p)_1 = (1 - \phi_t) \cdot PN(d_p)_{up} \qquad \textit{Eq. 5-6}$$

Here PSD_1 is the number of particulates at each diameter entering into the first (top) slab. The PSD at j^{th} slab can be calculated based on the filtration efficiency of the (j-1) slab.

$$PN(d_p)_j = \left(1 - \eta(d_{pj})\right) \cdot PN(d_p)_{j-1} \qquad \textit{Eq. 5-7}$$

Therefore, the number of particulates exiting the filter (at the bottom slab $j = N_{slab}$) can be calculated. The total particulate number filtration efficiency is:

$$\eta(d_p) = 1 - \frac{PN(d_p)_{j=N_{slab}}}{PN(d_p)_{up}} \qquad \textit{Eq. 5-8}$$

From the discussion above, one of the greatest challenges is to model the filtration efficiency. In the next section, a heterogeneous multi-scale filtration model is presented to calculate the filtration efficiency.

www.manaraa.com

5.2 Heterogeneous multi-scale filtration (HMF) model

5.2.1 Pore size distribution

The porous wall of a filter typically has a heterogeneous micro-structure. One of the most common techniques for porous material characterization is mercury intrusion porosimetry measurements. Mercury porosimetry provides a wide range of information, e.g. the pore size distribution, the total pore volume and specific surface area of a porous sample [146]. Porosimetry data of common DPF samples were reported by Wirojsakunchai et al. [147] and Merke et al. [148]. Some studies found that the pore structure of the DPF based on porosimetry data analysis had significant effects on the filter performance [149,150,151].

From reported porosimetry data [147,148,151], most of pore size distributions follow a narrow or wide log-normal distribution. From this observation the pore size distribution is modeled using a log-normal statistical distribution function. Figure 5-3 shows the experimental porosimetry data of twelve samples of a cordierite DPF by using a porosimeter [152]. The twelve pore size distributions are very consistent with each other. The mean porosity of the filter samples is 0.48 and a most likely pore size corresponding to the peak of the pore size distribution is around 18 μm. This pore size is actually not the statistical mean pore size of the filter samples but the most critical pore size that governs the filtration performance. This most likely pore size is common used in classic mean filtration models.

www.manaraa.com

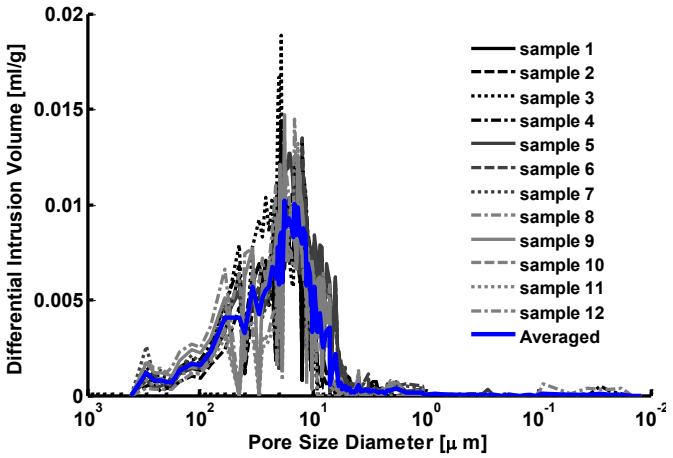

Figure 5-3: Pore size distributions of 12 samples of cordierite DPF measured by porosimeter

The averaged pore size distribution of 12 samples in Figure 5-3 is fitted by a log-normal distribution function with the same most likely pore size of 18 μm and a variance of 60 μm. The comparison of the pore size distributions between experimental data and fitted distributions is shown in Figure 5-4.

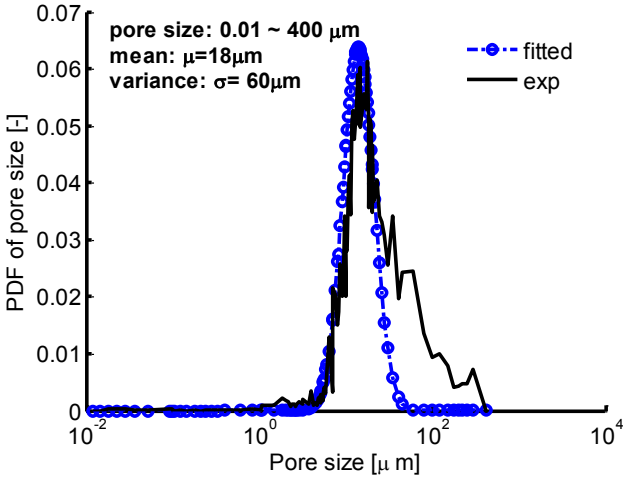

Figure 5-4: Comparison of the experimental averaged and fitted pore size distribution

Note that the magnitude of the pore size distribution from porosimeter was normalized in Figure 5-4. From statistical theory, the integral of the PDF over the pore size space gives unity, which is shown in Eq. 5-9.

$$\int pdf_{d_{ci}} \cdot d(d_{ci}) = 1 \qquad \textit{Eq. 5-9}$$

www.manaraa.com

The mean pore size of the distribution can be calculated as well from Eq. 5-10.

$$\int pdf_{do_i} \cdot do_i \cdot d(do_i) = do_m \qquad \textit{Eq. 5-10}$$

In order to use the solution of Kuwabara [99] flow in porous medium, the pore space has to be transformed to the collector space. By assuming the pore diameter is four times the ratio of the total pore volume to the total pore surface area, the diameter of the collectors can be determined in Eq. 5-11, where ϵ is the porosity of the filter. As a result, a PDF of collector size can be calculated according to "change of variables" in Eq. 5-12. The PDF of collector size is usually used in the calculation of collection efficiency, which will be discussed later.

$$d_{ci} = \frac{3(1-\epsilon)}{2\epsilon} d_{oi} \qquad \textit{Eq. 5-11}$$

$$pdf_{d_{ci}} = \frac{2\epsilon}{3(1-\epsilon)} pdf_{d_{oi}} \qquad \textit{Eq. 5-12}$$

5.2.2 Resolved flow velocity

An analytical solution of the flow field in a complex porous medium is impossible. Even though the flow is laminar in most operating conditions of particulate filters, the flow velocity inside the porous medium is highly nonlinear [153,154]. Furthermore, it is difficult to use numerical solutions from 3D CFD or Lattice Boltzmann Method (LBM) analysis to derive analytic solutions for filtration calculation. Therefore, an analytical solution of Stokes flow in a system of randomly packed spheres derived by Kuwabara [99] is used.

In creeping flow regime, the drag force exerted by the flow on an isolated sphere can be calculated by $F_D = 3\pi\mu d\overline{U}$, where $\overline{U}$ is the mean superficial velocity far away from the sphere with a diameter of d_c. In case of Stokes flow around a system of spheres with a packing density of $(1 -$

www.manaraa.com

ϵ), the drag exerted by the flow on a representative sphere in a system of spheres can be calculated by Eq. 5-13.

$$F_D = \frac{3\pi\mu d_c \bar{U}}{K(\epsilon)} \qquad \textit{Eq. 5-13}$$

Here $K(\epsilon)$ is a function of the porosity, which is a hydrodynamic factor of the system of spheres derived from flow field solution from Kuwabara [99]. At steady state, assuming the pressure drop across the porous wall with thickness h is a simple summation of all the drag force around each sphere, a linear momentum balance on the fluid in the control volume gives:

$$A \cdot \Delta P = N_s \cdot F_D \qquad \textit{Eq. 5-14}$$

where the number of the sphere in the system can be estimated by Eq. 5-15.

$$N_s = \frac{Ah \cdot (1-\epsilon)}{\frac{1}{6}\pi d_c^3} \qquad \textit{Eq. 5-15}$$

From Eq. 5-13 to Eq. 5-15, the mean superficial velocity is

$$\bar{U} = \frac{K(\epsilon)}{18\mu(1-\epsilon)} \frac{\Delta P}{h} d_c^2 \qquad \textit{Eq. 5-16}$$

However, a realistic porous filter is made of a cluster of spheres with different diameters. Similarly, the superficial velocity across the system of mono-dispersed spheres with a diameter of dc_i at the same pressure drop and porosity can be given by

$$U_i = \frac{K(\epsilon)}{18\mu(1-\epsilon)} \frac{\Delta P}{h} d_{ci}^2 \qquad \textit{Eq. 5-17}$$

As discussed early, the size distribution of spheres can be described by a lognormal probability density function. The mean velocity can be related to the individual velocity from Eq. 5-18.

$$\bar{U} = \int pdf_{d_{ci}} \cdot U_i \cdot d(d_{ci}) \qquad \textit{Eq. 5-18}$$

www.manaraa.com

Based on Eq. 5-16 to Eq. 5-18, the velocity for each individual sphere with a diameter dc_i can be calculated as:

$$U_i = \left(\frac{d_{ci}}{l_{dc}}\right)^2 \bar{U} \qquad \textit{Eq. 5-19}$$

where l_{dc} is a length scale that represents the overall filter collector size and is defined as $l_{dc} = \left[\int pdf_{d_{ci}} \cdot d_{ci}^2 \cdot d(d_{ci})\right]^{1/2}$.

5.2.3 Single Collector Efficiency

There are different collection mechanisms involved in filtration process: diffusion (Brownian), direct interception, inertia, gravitational, electrostatic and van der Waals [98]. The main mechanisms that dominating filtration performance of diesel/gasoline particulate filters at typical engine exhaust conditions are diffusion, direct interception and inertia impaction mechanisms [103]. A single collector efficiency due to diffusion and interception from Lee et al. [102] was widely and successfully applied in DPF filtration modeling [103,104,105,155]. The objective of this paper is not to derive a new correlation for single collector efficiency but to develop a new methodology for filtration efficiency calculation. Therefore, the single collector efficiency based on convection-diffusion equation from Lee et al. [102] is used as the basis for calculating filtration efficiency.

Diffusion

Single collector efficiency due to diffusion can be calculated from a flow field analysis and solving the convective diffusion equations near the boundary layer of a representative sphere. Analytical derivation of the diffusion efficiency of a single sphere can be found in Lee et al. [102].

www.manaraa.com

$$E_D = 2\left(\frac{3\pi}{4}\right)^{2/3}\left(\frac{\epsilon}{K(\epsilon)}\right)^{1/3} Pe_i^{-2/3} \qquad \textit{Eq. 5-20}$$

The Peclet number in Eq. 5-21 is defined as

$$Pe_i = \frac{U_i \cdot d_{ci}}{D_{diff}} \qquad \textit{Eq. 5-21}$$

Here $D_{diff} = \frac{k_B T}{3\pi\mu \cdot d_p} f(K_n)$ is the diffusion coefficient of a particle with a diameter of dp. $f(K_n) = 1 + K_n\left[1.257 + 0.4\exp\left(-\frac{1.1}{K_n}\right)\right]$ is the slip correction factor where $K_n = \frac{2\lambda}{d_{ci}}$ is the Knudsen number.

Direct Interception

As particle size becomes larger, its effect known as direct interception may be taken into consideration for particle collection. A single collector efficiency due to direct interception was derived based on the solution of creeping flow around a system of spheres by Lee et al. [156].

$$E_R = \frac{3(1-\epsilon)}{2K(\epsilon)} \frac{{N_R}^2}{(1+N_R)^2} \qquad \textit{Eq. 5-22}$$

Here N_R in Eq. 5-22 is a non-dimensional parameter to characterize the direct interception efficiency and l_{Ri} is a length scale to represent the critical length for direct interception.

$$N_R = \frac{dp}{l_{Ri}} \qquad \textit{Eq. 5-23}$$

Inertia Impaction

For large particles at relatively high velocity, the controlling collection mechanism is inertia impaction. The intensity of the inertial deposition of particles is described by the dimensionless Stokes number. In the applications of particulate filtration from engine exhaust, the Stokes number

www.manaraa.com

is very small and the inertia impaction makes limited contribution to the total collection efficiency. However, the inertia impaction is still considered in our model.

In order to take account the influence of the Reynolds number on the inertial efficiency, an effective Stokes number was proposed by D'Ottavio and Gorden [157], Gal et al. [158] and Otani et al. [159]. The effective Stokes number is calculated as the product of the Stokes number $Stk = \frac{\rho_p d_p^2 U_i}{18\mu \cdot d_{ci}}$ and a hydrodynamic term involving the Reynolds number and porosity. Based on Ergun's equation, the hydrodynamic term was modeled as $f(Re, \epsilon) = 1 + 1.75Re \cdot \frac{\epsilon}{150(1-\epsilon)}$, where $Re = \frac{\rho_g U d_{ci}}{\mu}$. The inertia efficiency correlation in Eq. 5-24 from Otani et al. [159] is used in this paper.

$$E_I = \frac{{Stk_{eff}}^3}{(0.014 + Stk_{eff})^3} \qquad \textit{Eq. 5-24}$$

$$Stk_{eff} = f(Re, \epsilon) \cdot Stk \qquad \textit{Eq. 5-25}$$

5.2.4 Total Filtration Efficiency

In filtration process, particles may be subjected to simultaneous effect of all deposition mechanisms. One of the basic but most difficult problems in filtration theory is to find the total collection coefficient. In general, this problem has not been exactly solved owing to mathematical difficulties [160]. In this paper, a common approach (the "independence rule") to calculate the total collection efficiency is used by assuming that all mechanisms act independently. Based on the "independence rule", the overall single collector penetration P_t can be calculated as a product of all penetrations from different deposition mechanisms. As a result, the total filter efficiency is $E_t = 1 - P_t = 1 - (1 - E_D)(1 - E_R)(1 - E_I)$.

www.manaraa.com

Filtration efficiency of a filter with a thickness of h and a porosity of ϵ can be calculated fromEq. 5-26.

$$\eta(d_{ci}, d_{pj}) = 1 - exp\left[-\frac{3(1-\epsilon)}{2\epsilon}\frac{E_t(d_{ci}, d_{pj}) \cdot h_j}{d_{ci}}\right] \qquad \textit{Eq. 5-26}$$

By summing the PDF weighted contributions from all of the collectors, a size dependent filtration efficiency can be calculated:

$$\eta(d_{pj}) = \frac{\int U_i \cdot \eta(d_{ci}, d_{pj}) \cdot pdf_{d_{ci}} \cdot d(d_{ci})}{\int U_i \cdot pdf_{d_{ci}} \cdot d(d_{ci})} \qquad \textit{Eq. 5-27}$$

By substituting U_i from Eq. 5-19 into Eq. 5-27, the final size dependent filtration efficiency can be written as

$$\eta(d_{pj}) = \frac{\int \eta(d_{ci}, d_{pj}) \cdot {d_{ci}}^2 \cdot pdf_{d_{ci}} \cdot d(d_{ci})}{{l_{dc}}^2} \qquad \textit{Eq. 5-28}$$

5.2.5 Model sensitivity

To investigate the interaction between the pore size PDF and filtration efficiency, a filtration study is conducted on a typical particulate filter sample. The specification of the filter sample and operating conditions are shown in

Table 5-1. The filter sample has a mean porosity of 0.5 and a thickness of 12 mil, which are very comparable to most commercial DPFs or GPFs. The micro-structure of the filter is represented by a pore size distribution with a mean pore size of 20 μm and a variance of 60 μm. The size of particulates for this study scales from 20 to 1000 nm, which covers the typical particulates from diesel and gasoline combustion engines.

www.manaraa.com

Table 5-1: Filter specifications and operating conditions

Filter material	Cordierite
Mean pore size [μm]	20
Pore size variance [μm]	60
Thickness [mil]	12
Mean Porosity [-]	0.5
Superficial velocity [cm/s]	5
Gas temperature [°C]	400
Soot particle size [nm]	20 ~ 1000

Each pore at a particular size corresponding to a particular collector makes a contribution to total filtration efficiency. Generally, small pores have higher filtration efficiency. However, contributions from small pores to total filtration efficiency can be low due to lower probability density of small pores. In Figure 5-5, a pore with a diameter of 12 μm makes less contribution to the total filtration efficiency compared to a pore with a diameter of 20 μm. Pores with relatively smaller diameters and higher probability densities dominate the total filtration efficiency.

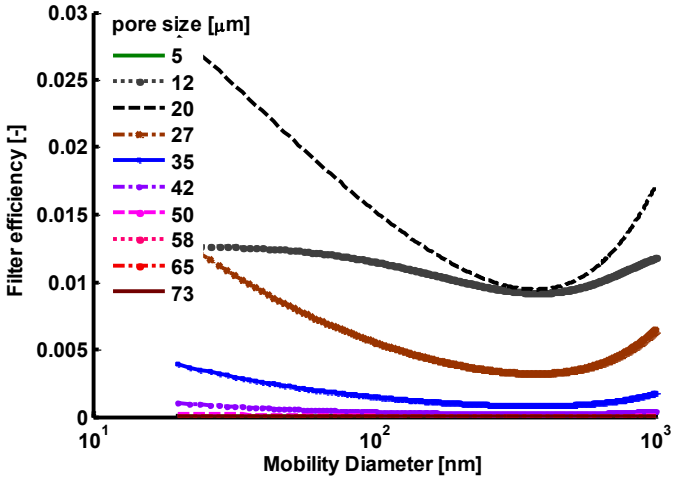

Figure 5-5: Filtration efficiency contributions of each collector with different size

Similarly, a contour plot of the filtration efficiency contributions from each pore size is shown in Figure 5-6. The most effective pores have a diameter between 10 μm to 30 μm for filtering

www.manaraa.com

relatively small particulates in the diffusion regime, which is consistent with the pore size distribution. In the interception filtration regime, the filtration efficiency is less sensitive to the pore size. There is a narrow range of pore diameters for effective collectors compared to that in the diffusion regime. This contour plot essentially represents how the PDF of pore size impacts the total filtration efficiency in the model.

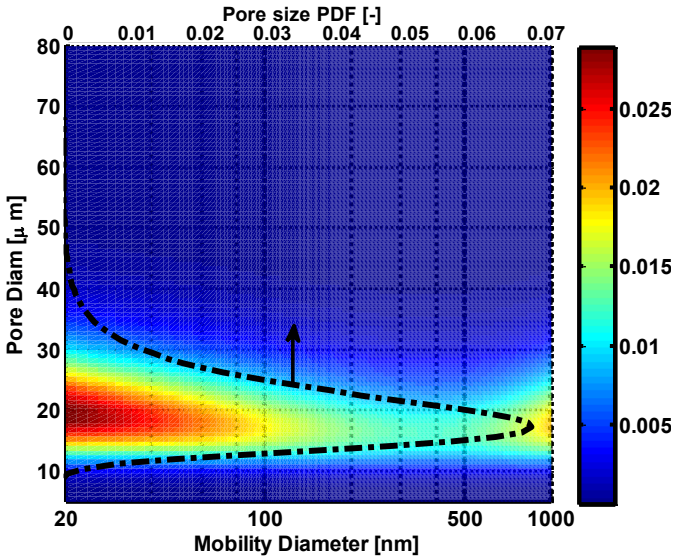

Figure 5-6: Contour plot of filtration efficiency contributions of each collector with different size

Variance of a pore size distribution determines how the pore size varies from the mean pore size. Physically, a pore size distribution with a small variance means the porous medium has more homogeneous micro-structure or mono-dispersed pores. In contrast, a pore size distribution with a large variance means the porous medium has more heterogeneous micro-structure or poly-dispersed pores. To investigate how the pore size distributions change the filtration efficiency in the HMF model, a few pore size distributions are created with the same mean pore size of 20 μm and different variances. These pore size distributions are shown in Figure 5-7.

www.manaraa.com

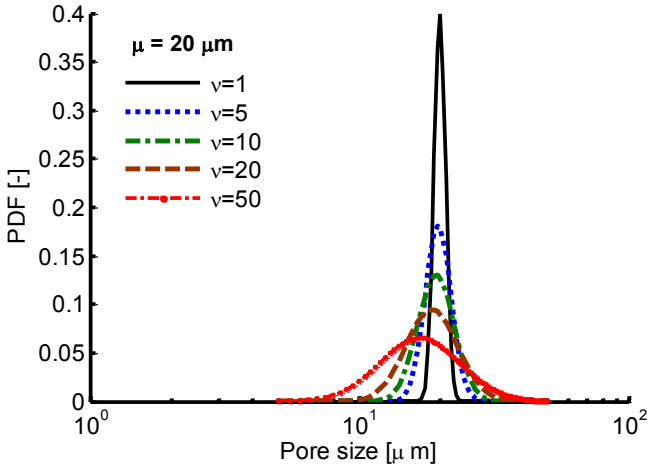

Figure 5-7: Pore size PDFs with different variances

As expected, as pore size variance increases, filtration efficiency tends to decreases over the whole range of particulate sizes (see Figure 5-8). Large pores are less effective for collecting particulates compared to small pores. As the variance reaches a very small value, the filtration efficiency from the HMF model is getting close to the mean model, which solely uses the mean pore size for filtration efficiency calculations. In other words, the HMF model recovers the mean model when the variance is small.

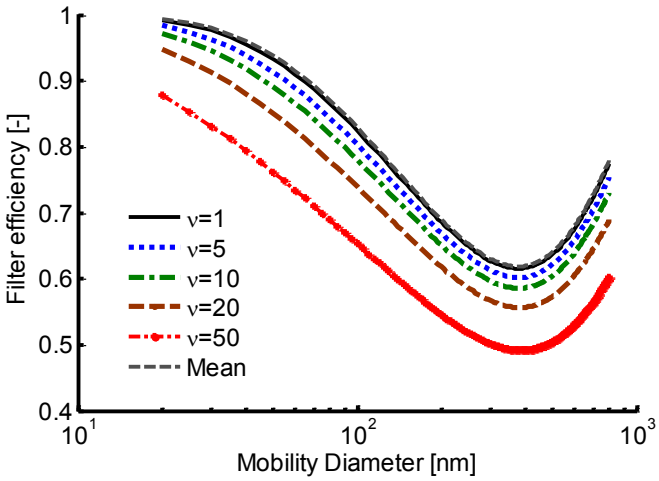

Figure 5-8: Comparison of particulate size dependent filtration efficiencies between mean filtration model and HMF models with different pore size distributions

From experimental pore size distribution measurements, it can be seen that a porous filter contains a wide range of length scales, which essentially determine the overall filtration performance of the

www.manaraa.com

filter. Individual collection efficiency due to different collection mechanisms may be controlled by different critical length scales.

To demonstrate the effect of length scales on filtraiton efficiency, the length scale in the interception efficiency is modeled as a product of a constant f and the diffusion length scale d_{ci} (see Eq. 5-29). The effect of interception length scale by changing the value of f on filtration efficiency is shown in Figure 5-9.

$$l_{Ri} = f \cdot dc_i = f \cdot \frac{3(1-\epsilon)}{2\epsilon} dpore_i \qquad \textit{Eq. 5-29}$$

Changing interception length scale has almost no effects on the filtration efficiency on the diffusion regime (small size particles). The interception efficiency increases as f decreases as expected. Also, note that the most penetrating particle size shifts to the left.

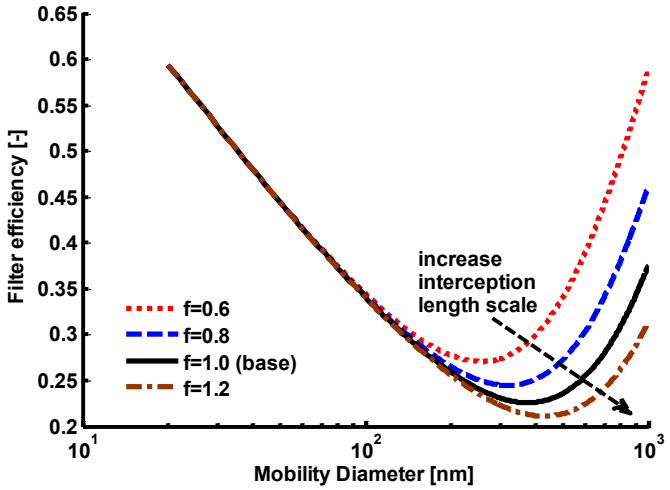

Figure 5-9: Effect of interception length scale on filtration efficiency

5.3 HMF model validations

There are few high quality experimental filtration data of particulates from combustion engines. First, particulates from combustion engine have complicated morphology and chemical

www.manaraa.com

composition and are difficult to characterize [161]. On the other hand, it is very difficult to get solid, reproducible filtration data. Particle filtration is highly dependent on filter preparation, particle sampling and measurement approaches. In this paper, several fundamental filtration experiments in the literature are selected for model validation [162,163,164].

5.3.1 Sintered Granular Ceramic Filter

The first filter used for model validation is a sintered granular ceramic filter, with a mean pore size of 10.8 μm and a mean porosity of 45% [162]. Filtration efficiency equations are derived based on the assumption that a porous medium consists of spherical grains. Therefore, filtration experiments from granular ceramic filters are very appropriate to test the filtration model.

The filter has a mean pore size of 10.8 μm and a thickness of 1.65 mm, which is much higher than the wall thickness of typical DPFs or GPFs. The particles in the filtration study are dioctyl phthalate (DOP 1%) aerosol particles with a diameter range from 100 nm to 700 nm. The filter was operated at four face velocities (1 cm/s, 2 cm/s, 3 cm/s and 4 cm/s).

Since there is no direct pore size distribution measurement for this filter, a pore size PDF is created by using the mean pore size and providing a pore size variance of 2 μm. This pore size PDF is shown in Figure 5-10.The pore size PDF used in the HMF model is shown in Figure 5-11. Calculated filtration efficiencies from the HMF model are compared to a "mean" model as well as the experimental data at a face velocity of 2cm/s in Figure 5-11. The mean model using the mean pore size over-predicts the filtration efficiency over the whole range of particle size. The HMF model gives a very good agreement to the experimental data.

www.manaraa.com

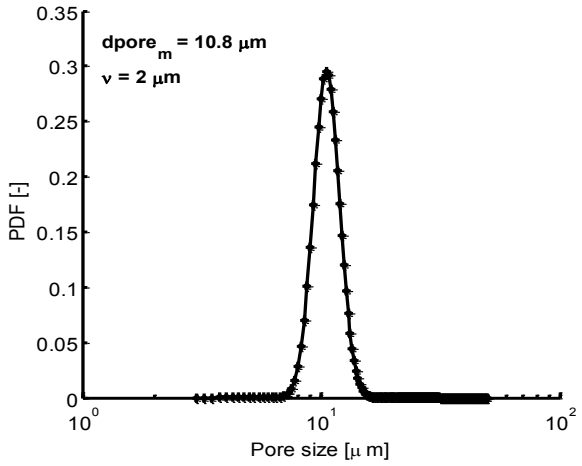

Figure 5-10: Pore size PDF of a sintered granular ceramic filter sample

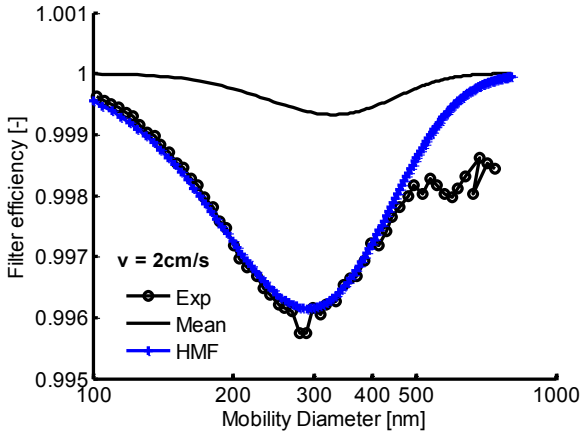

Figure 5-11: filtration efficiency comparison at face velocity of 2 cm/s

Similarly, the HMF model gives good predictions of filtration efficiency at four different face velocities in Figure 5-12, especially for small particles in the diffusion dominated regime. As face velocity increases, the filtration efficiency decreases dramatically for relatively small particles (in diffusion dominated regime) due to decrease of the residence time of particles in the filter. The dependence of face velocity on filtration efficiency has been captured by the model. Moreover, the maximum penetrating particle size (the particle size with minimum filtration efficiency) has been correctly predicted by the HMF model.

The decrease in filtration efficiency with increased velocity should diminish upon entering the direct interception regime, where the efficiency depends only on the particle size and not the velocity. This tendency is evident in Figure 5-12, even though there are some discrepancies between the HMF model and data for very large particles (> 500 nm). The differences could be due to high uncertainty of the filtration efficiency measurements for large particles.

www.manaraa.com

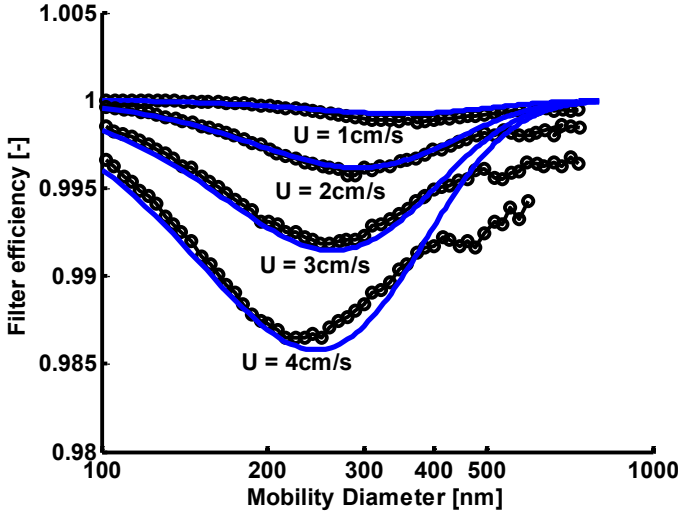

Figure 5-12: Comparison of the filtration efficiencies between the HMF model and experiment at four different face velocities

5.3.2 Cordierite-bonded SiC DPF

Filtration experimental data from Ohara et al. [163] are used to further investigate effects of filter micro-structure (in terms of pore size distribution) on filtration efficiency. Three cordierite-bonded SiC DPF samples with different mean pore sizes of 9μm, 12μm, and 17μm are selected from the filtration experiments conducted by Ohara et al. [163]. The round disc filter samples all have the same diameter of 25 mm and thickness of 0.305 mm (12 mil). The filter wall thickness is very close to typical DPF filter wall thickness. During the filtration tests, $ZnCl_2$ particles with a diameter in the range of 20 nm to 500 nm were used instead of particulates from diesel engine exhaust.

Three pore size distributions with different mean pore sizes and variances in the HMF model are shown in Figure 5-13. Calculated logarithmic standard deviation of the pore size from the PDFs are comparable with the reported logarithmic standard deviation of the pore size distribution [163].

www.manaraa.com

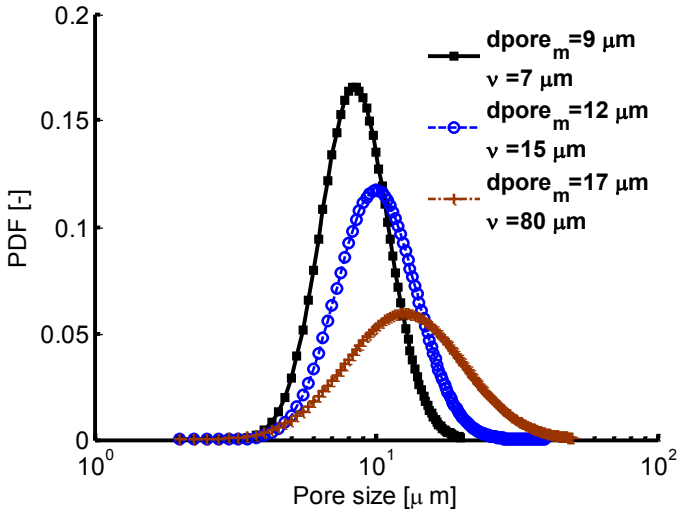

Figure 5-13: Three pore size PDFs with mean pore size of 9μm, 12μm, and 17μm

The comparisons of filtration efficiencies of the three filter samples between the model and experimental data at two different face velocities are shown in Figure 5-14 and Figure 5-15. Even through the experimental data were poorly resolved over the particle size domain, the model captures the particle size dependent filtration efficiency for all filter samples. Both the data and model indicate that the smaller the mean pore size, the greater the filtration efficiency. The effects of the pore size distribution on filtration efficiency are correctly captured by the model.

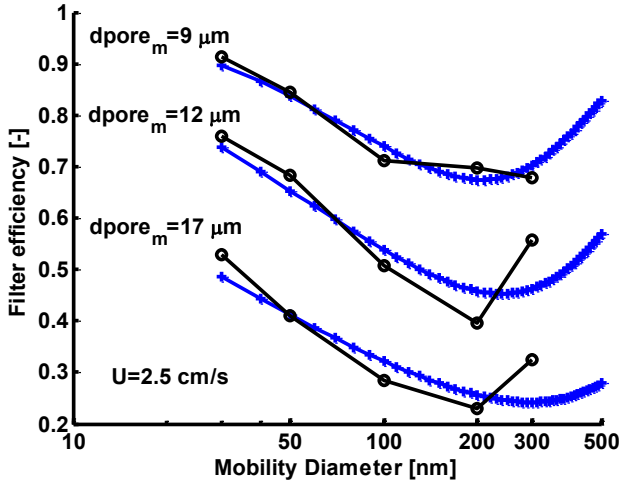

Figure 5-14: Filtration efficiency comparisons of three filter samples at face velocity of 2.5 cm/s

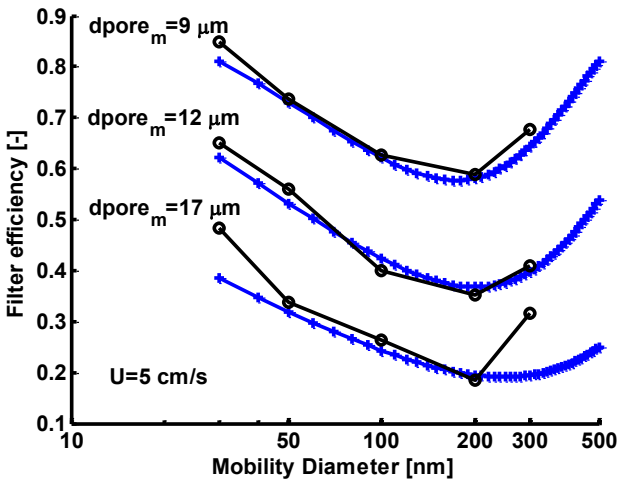

Figure 5-15: Filtration efficiency comparisons of three filter samples at face velocity of 5 cm/s

www.manaraa.com

5.3.3 Single Channel Filter Sample

The HMF model is further tested using filtration data recently collected on commercial particulate filters at laboratory scales. The fundamental filtration experiments were conducted at PNNL for an uncoated, single channel filter sample [162]. The single channel was prepared by extracting a channel from a larger DPF substrate and is shown in Figure 5-16.

Figure 5-16: A Single channel sample cut from a filter [165]

Table 5-2: Specification of Corning Duratrap AC filter

Filter Sample Name	Corning Duratrap
Filter material	cordierite
Mean pore size [μm]	18.8
Pore size variance [μm]	43
Cell density [cpsi]	200
Thickness [mil]	12
Filter length [cm]	5.0
Mean Porosity [-]	0.5435
Superficial face velocity [cm/s]	0.56~1.8
Gas temperature [°C]	20
Particle size [nm]	40 ~ 400

As shown in Table 5-2, the mean pore size of the filter is 18.8 μm, a variance of pore size 43 μm is chosen to generate a PDF of pore size distribution in the HMF model. This pore size PDF is shown in Figure 5-17. Ammonium Sulfate particles which have a spherical shape were used as filtration particles.

www.manaraa.com

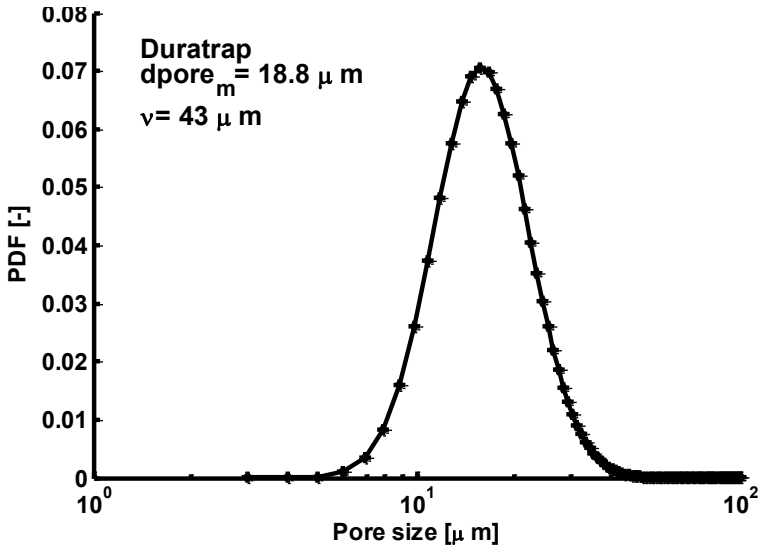

Figure 5-17: Pore size PDF for Corning Duratrap AC filter

The comparison of the filtration efficiency between the model and experimental data at four flow rates are shown in Figure 5-18. The filtration efficiency drops significantly as particle size increases. The HMF model correctly predicts the filtration efficiency at small and large particle sizes. The most penetrating particle size of this filter is around 200 nm to 300 nm, which is captured by the model as well.

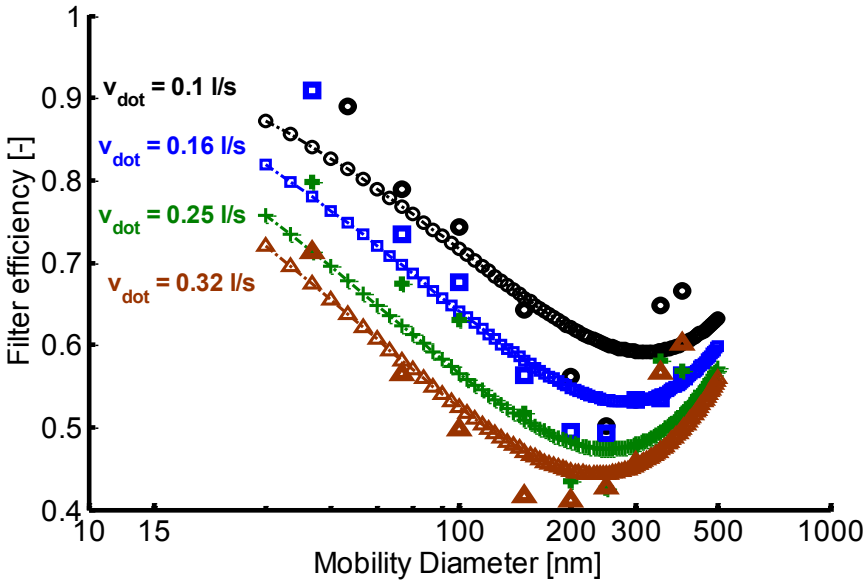

Figure 5-18: Comparison of the filtration efficiency for the Duratrap filter at four flow rates

www.manaraa.com

5.3.4 Mini DPF Samples

The last model validation in this study is conducted on two commercialized mini-DPF samples [164]. The filter samples are 1 inch in diameter and 3 inch in length. Each mini-DPF sample, which is shown in Figure 5-19, is composed of a few DPF channels. Specifications of these two DPF samples are compared in Table 5-3. Aerosolized salt particles were used in the filtration experiments.

Table 5-3: Mini DPF sample specifications

Sample	NGK 558	NGK 650
Filter material	cordierite	cordierite
Mean pore size [μm]	18	23.5
Pore size variance [μm]	70	90
Cell density [cpsi]	200	300
Thickness [mil]	12	12
Mean Porosity [-]	0.558	0.650
Superficial velocity [cm/s]	1.68	1.55

Figure 5-19: Mini NGK DPF samples [166]

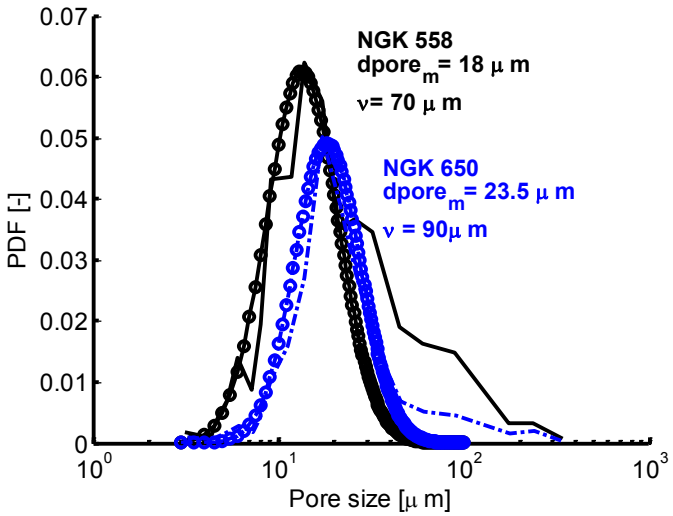

Figure 5-20: Pore size DPFs of NGK 558 and NGK 650

Experimental pore size distribution measurements and created pore size PDFs for the two mini DPF samples are shown in Figure 5-20. The differences of pore size distribution for NGK 558

www.manaraa.com

between the experimental pore size distribution and modeled pore size PDF are due to the non-symmetry of the experimental pore size distribution, which has a long tail on the side of large pore diameter. The modeled pore size PDF of NGK 650 is very close to the experimental pore size distribution.

The filtration efficiency comparisons of NGK 558 and NGK 650 filters between the model and experimental data are shown in Figure 5-21 and Figure 5-22. The HMF model matches the experimental data very well in the diffusion dominated regime (particle diameter < 300 nm). In contrast, the mean model over-predicts the filtration efficiency over the whole range of particle sizes. The differences between the model and experimental data at large particle sizes could be due to uncertainty of the measurements, which can be seen from the experimental data scatter of NGK 558 in Figure 5-21.

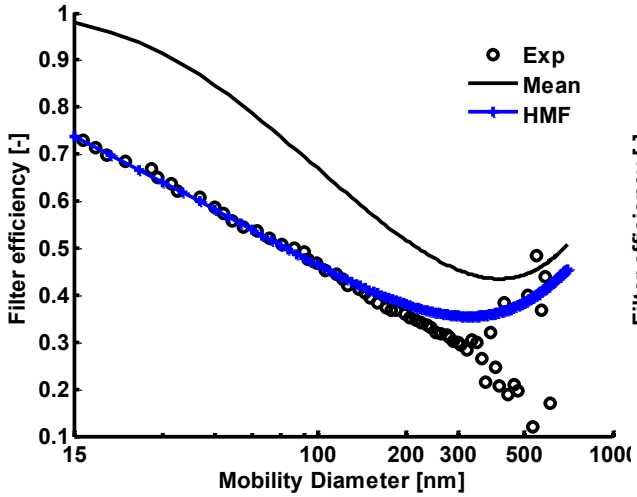

Figure 5-21: Filtration efficiency comparison of NGK 558

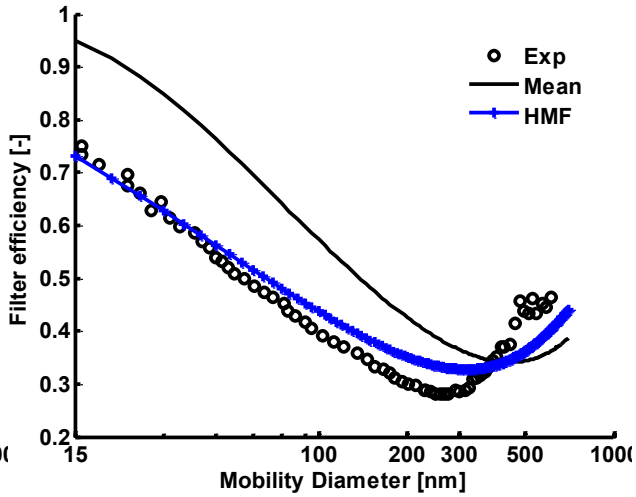

Figure 5-22: Filtration efficiency comparison of NGK 650

5.4 Dynamic HMF model development

The previous section shows the validations of the HMF model on initial (or clean) filter filtration efficiency. During particle filtration, filter states (characteristics of filter, for instance, porosity,

www.manaraa.com

permeability) change with time. As a result, filtration efficiency, particulate distribution inside the wall as well as pressure drop will change with time. Therefore, how to accurately model the dynamic process of filtration is a challenge. In this section, a dynamic filtration model based on HMF is presented.

5.4.1 Dynamic filtration theory based on HMF

During early stage of filtration, particulate filtration is governed by the micro-structure of a clean filter. Even though the micro-structure of the filter is slightly changed due to particulate deposition inside the wall, the macro-properties of the filter remain almost the same. As more particulates accumulate inside the porous wall, the micro-structure of the filter is altered. In other words, cumulated particulates become part of the filter. A "new" filter with different structure and properties continues filtering incoming particulates.

The classic dynamic filtration theory is based on the change of a collector diameter. Assuming a collector is a sphere, the new diameter of the collector will increase as particulates deposit on the surface of the collector, which is shown in Eq. 5-30.

$$dc_{new} = 2\left[\frac{3}{4\pi}\frac{m}{\rho} + \frac{dc_{old}}{2}\right]^{1/3} \qquad \textit{Eq. 5-30}$$

where m is the mass of deposited particulates and ρ is the packing density of the particulates.

In the HMF model, there is a cluster of collectors with different sizes, which are characterized by a PDF. Similarly, the new diameter of each individual collector can be calculated from Eq. 5-31. However, the particulate mass deposited on each individual collector needs to be determined. Based on the statistical characteristics of a collector size distribution, the particulate mass

www.manaraa.com

depositing on a specific collector can be estimated by its probability density function from Eq. 5-32. In other words, more particulates will likely deposit on the most popular collector, which has a high probability density.

$$dc_{i,t} = 2\left[\frac{3}{4\pi}\frac{m_i}{\rho} + \frac{dc_{i,t-1}}{2}\right]^{1/3} \quad \textit{Eq. 5-31}$$

$$m_i = m \cdot pdf_{dc_i,t-1} \quad \textit{Eq. 5-32}$$

Once the sizes of all the collectors are calculated, a new PDF of collector size can be determined from Eq. 5-33 from the "change of variable" rule.

$$pdf_{dc_{i,t}} = f(dc_i, pdf_{dc_i,t-1}) \quad \textit{Eq. 5-33}$$

One of the examples to illustrate the change of collector size PDF is shown in Figure 5-23. As particulates are captured by collectors, the collector size PDF shifts to the right as small collectors become larger due to particulates deposition. Moreover, the peak of the PDF increases significantly since more particulates deposited on most likely collectors with a diameter around 20 μm. In contrast, the probability of large particulates increases slowly.

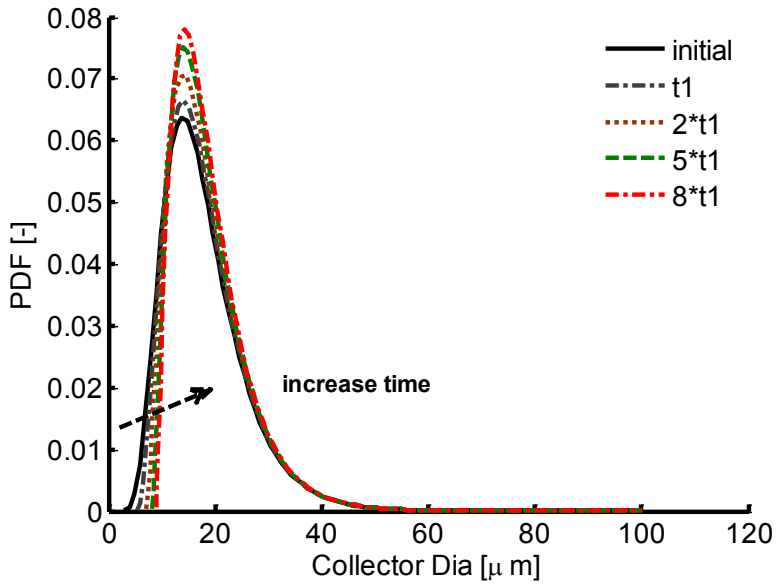

Figure 5-23: Evolution of collector size PDF with time

www.manaraa.com

Based on the updated collector size and PDF, some statistical functions are defined from Eq. 5-34 to Eq. 5-36 in order to calculate the macro-states of a filter.

$$Int_{dc,t} = pdf_{dc_{i,t}} \cdot dc_{i,t} \quad \textit{Eq. 5-34}$$

$$Int_{k,t} = pdf^2_{dc_{i,t}} \cdot dc_{i,t} \quad \textit{Eq. 5-35}$$

$$Int_{\epsilon,t} = pdf^3_{dc_{i,t}} \cdot dc_{i,t} \quad \textit{Eq. 5-36}$$

The macro-states of a filter can be calculated from the initial macro-states of the filter and the change of micro-states. For instance, one of the macro properties of a filter is mean collector size. The new mean collector size can be calculated according to the definition in Eq. 5-37. Similarly, a new porosity and permeability are calculated by their definition in Eq. 5-38 and Eq. 5-39.

$$dc_t = \int pdf_{dc_i,t} \cdot dc_{i,t} \cdot d(dc_{i,t}) = \int Int_{dc,t} \cdot d(dc_{i,t}) \quad \textit{Eq. 5-37}$$

$$\epsilon_t = 1 - (1 - \epsilon_0)\frac{\int Int_\epsilon \, d(dc_{i,t})}{\int Int_{\epsilon_0} \, d(dc_{i,t})} \quad \textit{Eq. 5-38}$$

$$k_t = k_0 \cdot \frac{\int Int_k \, d(dc_{i,t})}{\int Int_{k_0} \, d(dc_{i,t})} \cdot \frac{f(\epsilon_t)}{f(\epsilon_0)} \quad \textit{Eq. 5-39}$$

5.4.2 Porosity distribution across the wall

Inhomogeneous porosity distribution across the filter wall was reported by some researchers using experimental diagnostic tools [165,167]. It was found that porosity increases drastically from nominal mean value at the center of a filter to a high value near the surface. Since the porosity distribution across the wall has a significant effect on flow distribution as well as pressure drop, a porosity distribution profile is imposed to resolve the heterogeneous wall structure by discretization of the wall. The porous filter wall was discretized into a number of slabs or layers along the wall direction. The homogeneous porosity distribution used in most of filtration modeling and heterogeneous porosity distribution in this study are shown in Figure 5-24.

www.manaraa.com

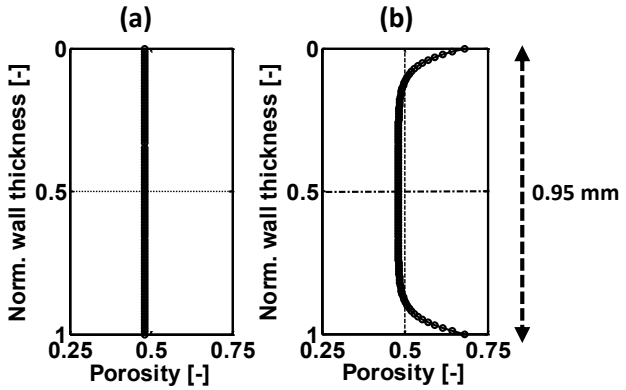

Figure 5-24: Porosity distribution across the wall (a) homogeneous porosity distribution (b) heterogeneous porosity distribution

In Figure 5-25, particulate mass at different slabs (or different wall depth) was normalized by the maximum particulate mass in one of the slabs. By using a homogeneous porosity (mean porosity) distribution across the wall, most of particulate mass is deposited at the top slab resulting in a large mass gradient across the wall. It may be sufficient to use homogeneous porosity distribution that ignores the heterogeneous wall structure for simulating diesel particulate filtration, since a "soot cake" can be formed at the surface of the wall in a short time. There is a great amount of large particulates from conventional diesel engines that can quickly fill up the top slab and prevent incoming particulates penetrating into the wall.

However, a heterogeneous porosity distribution is necessary to simulate filtration of small particulates from SIDI and advanced diesel combustion engines. By using the heterogeneous porosity distribution, a broader distribution of particulates is observed at the upper portion of the filter rather than the top slab in Figure 5-25. Particulates are penetrating deeper into the filter resulting in a lower gradient of particulate mass across it. This is consistent with the observation by Karin et al. [167] from filtration visualization experiments.

www.manaraa.com

Generally, SIDI gasoline engines and advanced diesel combustion engines generate much more particulates emission consisting of small particulates compared to conventional diesel engines. Relatively small particulates may penetrate into the porous wall or might escape from the filter. Therefore, filtration characteristics of small particulates are more dependent on the micro-structure of the porous wall. It is necessary to resolve the complicated porous wall structure.

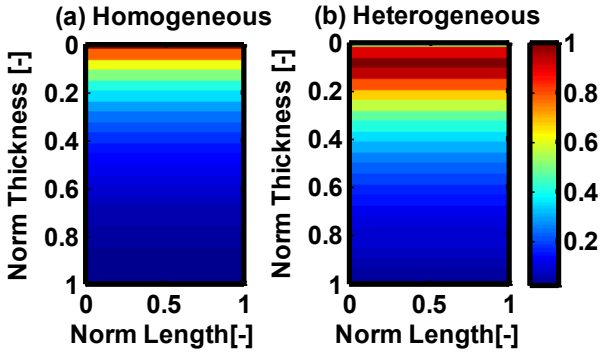

Figure 5-25: Normalized particulate mass inside a filter after a 1200s filtration simulation by using (a) a homogeneous porosity distribution or (b) a heterogeneous porosity distribution

5.4.3 Exhaust filtration analysis (EFA) experiments

A Diesel Exhaust Filtration Analysis (DEFA) system [168,169] was initially developed by Wirojsakunchai et al. for diesel particulate filtration study in the Engine Research Center (ERC). Later, the DEFA system was modified by Viswanathan et al. [140] in order to experimentally investigate particulate filtration from fuel-neutral engine exhaust and was renamed as Exhaust Filtration Analysis (EFA) system. The schematic view of the DEFA system can be seen in Figure 5-26. One of wafer samples from previous studies in the DEFA system is shown in Figure 5-27.

www.manaraa.com

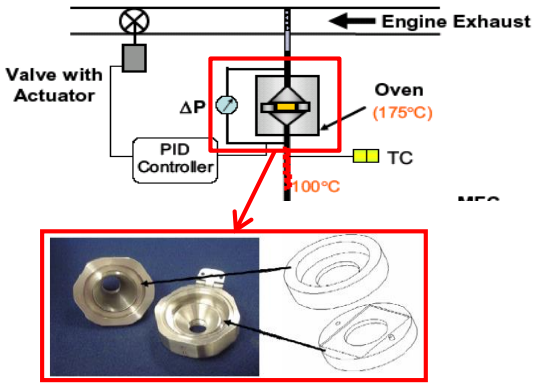

Figure 5-26: Schematic of the DEFA system [169]

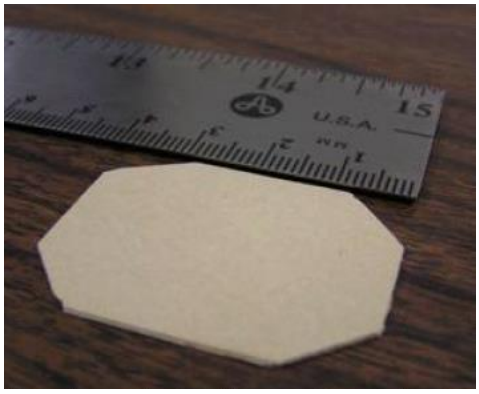

Figure 5-27: A cordierite wafer sample used in a full scale of particulate filter [168]

A very thin rectangular section of a filter wall is put into a holder to filter particulates when sampled raw exhaust flows through the holder. The absence of alternative plugged channels allow for more detailed fundamental studies of filtration. Flow contraction and expansion at the entrances and exits of the filter channels in a typical full-scale filter can be eliminated. The volumetric flow rate (or face velocity) and flow temperature are well controlled. More details about the EFA system setup and experimental procedures can be found in [140]. The specification of the filter sample in this study is shown in Table 5-4.

Table 5-4: Filter specifications and operating conditions

Filter material	Cordierite
Mean pore size [µm]	18
Pore size variance [µm]	60
Thickness [mm]	0.95
Mean Porosity [-]	0.48
Superficial velocity [cm/s]	~ 2.5
Gas temperature [°C]	175

Using well controlled flow rate, temperature, particulate size distribution from engine exhaust and properties of the filter sample as model inputs, particulate size distribution downstream of the wafer, filtration efficiency and pressure drop can be calculated by the model. This EFA system is extremely helpful to understand the fundamental filtration process for model development and validations.

www.manaraa.com

5.4.4 EFA validation

The HMF model was first validated by the filtration experiment of particulates from the SIDI engine fueled with gasoline at rich condition. The particulates at rich condition was chosen for filtration model validation, because it had the highest concentration of particulates and this has a large effect on the filtration as a function of time.

An upstream PSD and downstream PSDs at different times are shown in Figure 5-28. Basically, the downstream PSDs change with time significantly. Small particles (dp<100 nm) are greatly reduced after 200s and the deposition rate of small particles increases significantly with time. Relatively large particles (dp>100 nm) have slightly lower deposition rate compared to smaller particles. The most penetrating particle size for this filter is around 100 nm, which is accurately predicted by the model.

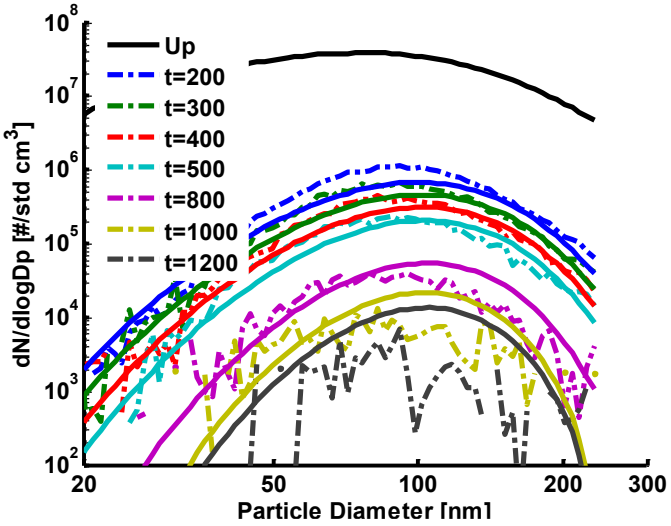

Figure 5-28: Particle size distributions downstream of the filter at different time for EEE-rich particulate filtration test (dashed line: experimental data; solid line: model)

Evolution of the number concentrations of individual particle of different sizes is shown in Figure 5-29. For small particles, the model agrees well with the experimental data on the number

www.manaraa.com

concentration evolution. For large particles, the model slightly over-predicted the filtration efficiency at the beginning with a slightly slower evolution rate. Overall, the evolution of the particulate concentration is accurately predicted across the whole range of particle sizes.

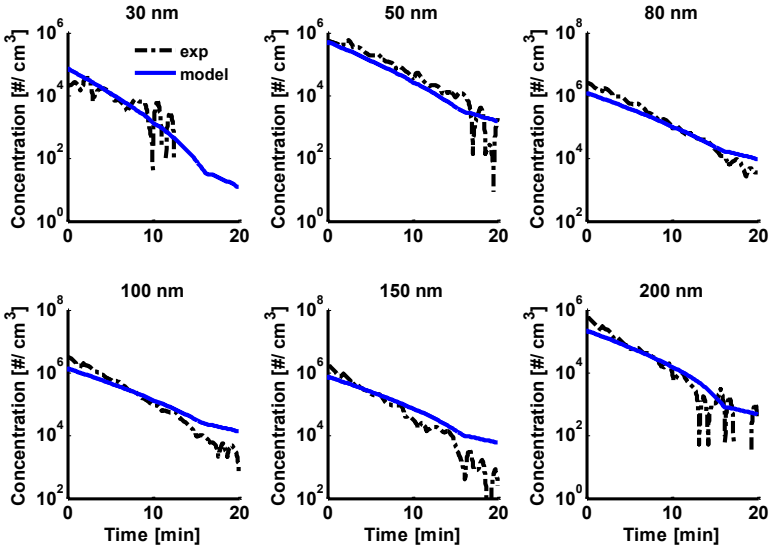

Figure 5-29: Size resolved particulate number concentration evolution for particulates from SIDI engine fueled with gasoline at rich condition

The macroscopic status of a filter during filtration can be traced by change of permeability of the filter wall. Since the face velocity of the filter is decreasing as backpressure increases due to particulate filtration, a normalized pressure drop is reasonable to represent the permeability evolution. The normalized pressure drop is defined in Equation (3) according to Darcy's law.

$$\frac{\Delta P}{U} = \frac{\mu \cdot h}{k_{perm}} \qquad \textit{Eq. 5-40}$$

As seen from Figure 5-30, the permeability evolution in terms of the normalized pressure drop is well captured by the model, which is critical for model validation. In other words, the dynamic status of the filter is accurately predicted by the model.

www.manaraa.com

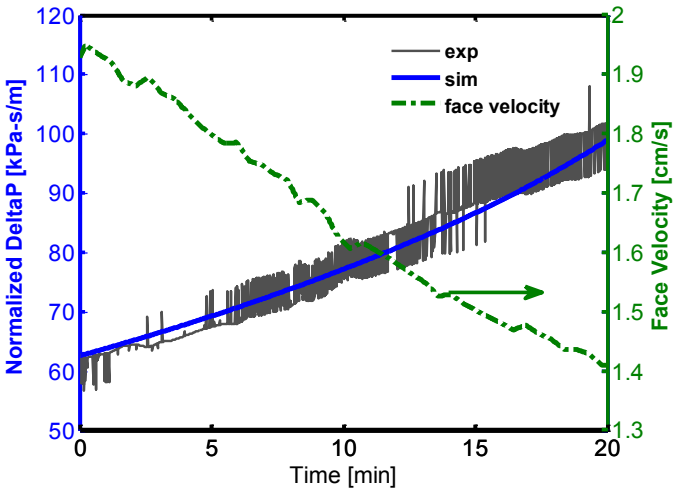

Figure 5-30: Normalized pressure drop across the filter wall

To further investigate the dynamic process of filtration, normalized particulate mass distributions at three different times are shown in Figure 5-31. The particulate mass is normalized by the maximum particulate mass deposited at t=1200s. At t=60s, the filter is almost clean since there is a limited number of particulates being deposited. After 600s, there is a gradient of particulate mass across the filter. Most of particles are deposited in the top one third of the filter. However, there are still quite a lot of particulates penetrating through the lower portion of the filter by comparing to the particulate distribution at t=60s. This is due to the use of a porosity distribution profile. Similarly, a high concentration of particulates near the top of the wall and a larger gradient of particulate mass were found at t=1200s.

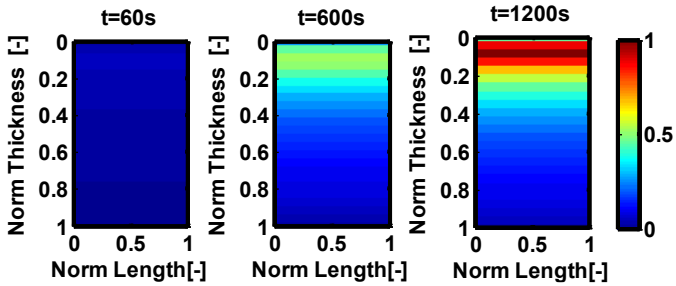

Figure 5-31: Normalized particulate mass across the filter wall at t=200s, 600s and 1200s

www.manaraa.com

5.5 Filtration characteristics of fuel neutral particulates

Various sources of particulates from combustion engines were used in the filtration studies. The particle size distributions at different engine operating conditions were obtained from Scanning Mobility Particle Sizer (SMPS) system. Particulate measurements were conducted by Sakai et al. [170] on a SIDI fuel neutral engine. Some particulates from advanced compression ignitions were collected by Zhang et al. [171]. However, only six representative particulate size distributions were selected for filtration studies, which can be seen from Figure 5-32.

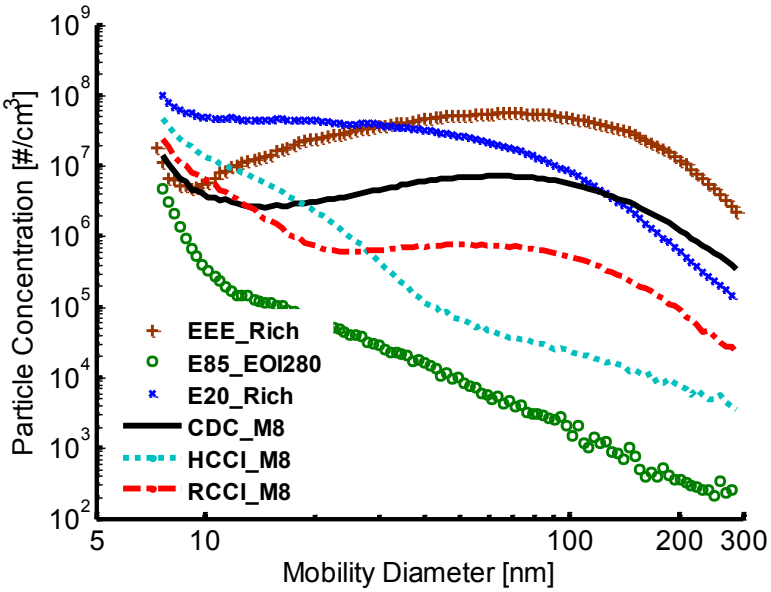

Figure 5-32: Selected PSDs for filtration studies

From Figure 5-32, the EEE rich case shows the highest number of large particlulates, which is similar to those from conventional diesel engines. The E20 rich case has high concentration of small particulates but relatively low concentration of large particulates. The E85 EOI280 case has the lowest particulates in the entire size range. CDC, HCCI and RCCI generate high number of ultra-fine particles (<50 nm), however CDC has more particles at large size (>50 nm) following by RCCI and HCCI as expected.

www.manaraa.com

5.5.1 Fuel neutral particulates

Particulates from a Spark Ignited Engine

EPA Tier II EEE gasoline, E20 (20% ethanol by volume) and E85 (85% ethanol by volume) were used to generate particulates from a single-cylinder fuel-neutral SIDI engine. The SIDI engine specifications are summarized in Table 5-5. Three particulate size distributions from the SIDI engine were selected for filtration studies: EEE rich, E20 rich and E85 EOI280. The operating conditions for those three cases are defined in Table 5-6.

Table 5-5: A single-cylinder SIDI fuel neutral engine

Cylinders/layout	single-cylinder
Compression Ratio [-]	11.97
Bore [mm]	85.96
Stroke [mm]	94.6
Connecting Rod Length [mm]	152.4
Inlet Valve Opening (IVO)	350°ATDC
Inlet Valve Closing (IVC)	220°ATDC
Exhaust Valve Opening (EVO)	150°ATDC
Inlet Valve Closing (IVC)	5°ATDC
Intake/Exhaust Valve Lift [mm]	9.9

Table 5-6: Engine operating conditions for the SIDI engine

Parameters	EEE Rich	E20 Rich	E85 EOI280
Speed [RPM]	2100	2100	2100
Injection Timing [°bTDC]	220	220	280
IMEP [kPa]	300	300	350
Fuel flow [mg/cyc]	11	11.7	15.4
Equivalence ratio [-]	1.13	1.13	0.98
Spark Timing [°bTDC]	25	25	25
CA-50 [°aTDC]	7	7	8.8
Injection Press [MPa]	11	11	11
Intake Temp [°C]	45	45	45
Oil Temp [°C]	90	90	90
Coolant Temp [°C]	90	90	90

www.manaraa.com

Particulates from a Compression Ignited Engine

Some particulates were collected from a compression ignition engine running at conventional diesel combustion (CDC), homogeneous charge compression ignition (HCCI) and reactivity controlled compression ignition (RCCI). Even though engines operated at HCCI and RCCI regimes can probably meet the PM mass regulations without any particulate filters [172], the PSDs from HCCI and RCCI were studied as references.

Table 5-7: Specification of the compression ignition engine

Description	value
Compression Ratio [-]	16.7
Bore [mm]	82
Stroke [mm]	90.4
Connecting Rod Length [mm]	145.54
Inlet Valve Opening (IVO)	344°ATDC
Inlet Valve Closing (IVC)	228°ATDC
Exhaust Valve Opening (EVO)	112°ATDC
Inlet Valve Closing (IVC)	388°ATDC
Swirl ratio [mm]	1.5
Injector	Bosch CRIN$_2$ 154μm × 6 at 144°

The engine is a modified single-cylinder version of a GM 1.9 L four-stroke light-duty diesel engine with a reentrant piston bowl. Table 5-7 shows the specification of this compression ignition engine.

Table 5-8: Engine operating conditions for CDC, HCCI and RCCI at mode 8

Parameters	CDC	HCCI	RCCI
Speed [RPM]	2300	2300	2300
Injection Timing [°aTDC]	-9	-	-44
IMEP [kPa]	800	800	800
Spark Timing [°bTDC]	25	25	25
CA-50 [°aTDC]	7.5	7.5	5
Injection Press [MPa]	95	-	500
Intake Temp [°C]	35	35	35
Intake Pressure [bar]	1.88	1.88	1.88
EGR [%]	0	42	48

"-" indicates that item is not applicable for the combustion strategy

www.manaraa.com

Particulates from mode 8, which represents a high-speed high-load condition was chosen for the filtration studies. The operating conditions at mode 8 for each combustion regime are shown in Table 5-8. More details about engine operation and particulate sampling for each combustion regime at mode 8 can be found in [170].

The objective of this paper is not to explore the combustion and emission characteristics for different combustion modes with different fuels but to investigate the effects of different particulate size distributions on filter performance. However, it is important to have a general idea about the differences of the particulates, which may lead to distinct filter performance.

5.5.2 Filtration of fuel neutral particulates

In the filtration studies, the face velocity is set to 2.56 cm/s, which is a typical wall velocity for a full scale filter. The total PN concentrations of selected PSDs from Figure 5-32 are shown in Figure 5-33. It is interesting to see that the SIDI engine fueled with gasoline at the rich condition generates more particulates than the diesel engine operating in the CDC regime.

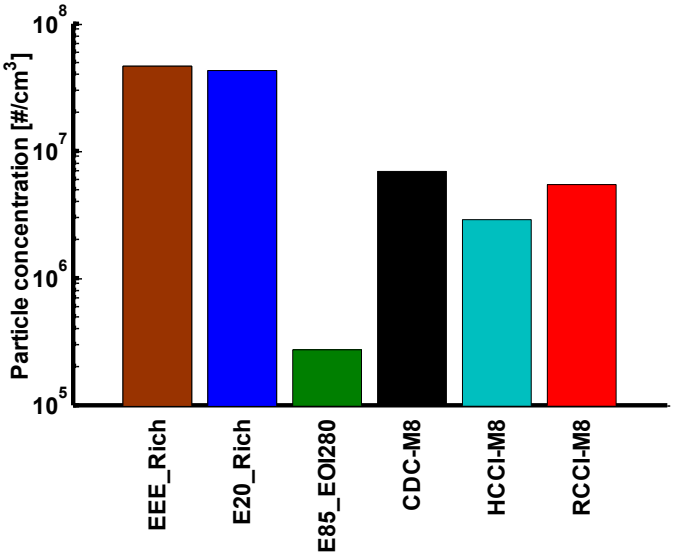

Figure 5-33: Total particulate number concentrations for selected PSDs

www.manaraa.com

The clean filter filtration efficiency as well as the filtration efficiencies at 1200s for all PSDs are shown in Figure 5-34. As expected, the filtration efficiencies of HCCI and E85 cases almost do not change after 1200s operation. The filter is almost clean since there is a lower rate of particulates flow through the filter and deposition in the filter for the HCCI and E85 cases compared to the EEE rich case. The EEE rich case gives almost 100% filtration efficiency after 1200s. However, it is surprising that CDC case has a much higher filtration efficiency than the RCCI case while the particulate concentration of CDC is only slightly higher than the particulate concentration of RCCI. Similarly, the E20 rich case has higher particulate number than the CDC case, however, the filtration efficiency of E20 rich is slightly higher than the filtration efficiency of CDC. It seems the filtration efficiency is not strongly dependent on the total particulate concentration.

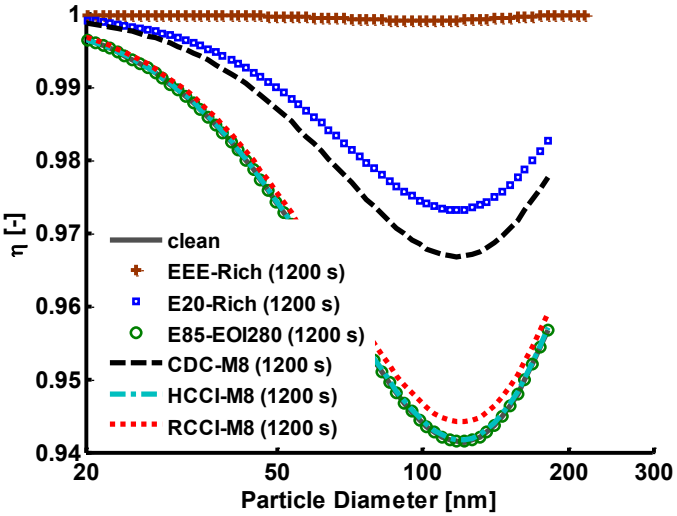

Figure 5-34: Size dependent filtration efficiencies of different PSDs at 1200s

In order to investigate filtration efficiency dependence, the total particulate volume for all the PSDs from Figure 5-32are shown in Figure 5-35. CDC has higher particulate volume compared to RCCI. This is because there are more large particulates from CDC compared to RCCI, even though the total number concentrations of CDC and RCCI are fairly close. It was found that the filtration efficiencies in Figure 5-34 actually follow the trend of total particulate volume.

www.manaraa.com

The maximum void space of a specific filter does not change with time. However, the effective void space will decrease as deposited particulates take up available void space and eventually alter the status of the filter. Therefore, it is the total particulate volume that determines the dynamic filtration characteristics rather than the total particulate number concentration.

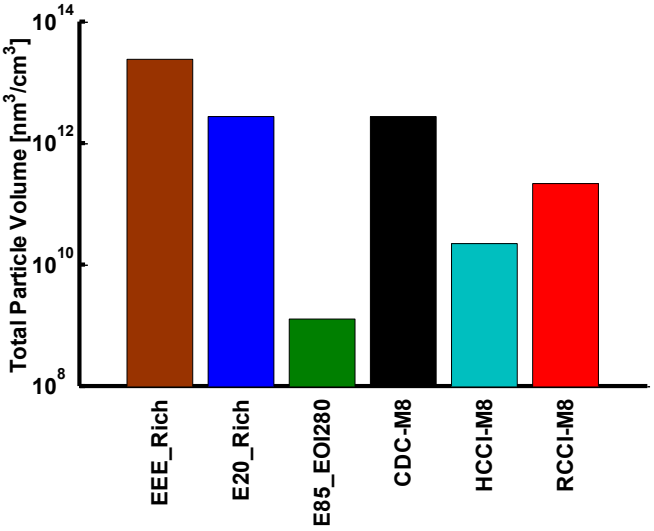

Figure 5-35: Total particulate volumes for selected PSDs

Normalized pressure drops for selected cases are shown in Figure 5-36. As expected, the permeabilities of E85, HCCI and RCCI cases are almost the same as the clean filter. While the permeability of EEE rich case changes dramatically followed by the E20 rich case and the CDC case.

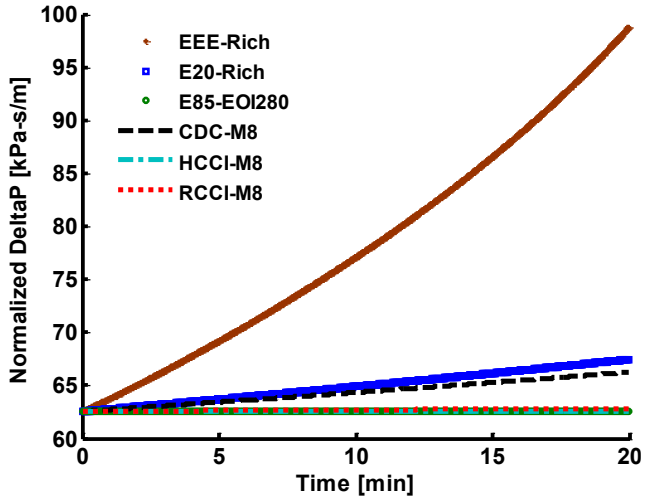

Figure 5-36: Normalized pressure drops across the filter wall of different PSDs

www.manaraa.com

In Figure 5-37, normalized particulate mass distributions across the wall are not homogenous for all the six cases and they all show a similar distribution pattern. The Particulate mass concentrations of E85, HCCI and RCCI cases inside the wall are much lower compared to those of EEE rich, E20 rich and CDC cases. Therefore, the particulate mass concentration at each slab is normalized by the total mass trapped inside the whole filter for each case. As demonstrated in Figure 5-25, the particulate distribution inside the wall is strongly dependent on the heterogeneous micro-structure of the filter wall itself, such as the porosity distribution across the wall.

Penetration depth for the six cases were investigated. The penetration depth is defined as the depth corresponding to 2% of the total mass trapped inside the wall, which is highlighted by the red dashed line in Figure 5-37. For EEE rich, E20 rich and CDC cases, the penetration lengths follow the reverse trend of the total particulate volume shown in Figure 5-35. The EEE rich case with highest total particulate volume has the shortest penetration depth followed by the E20 rich and the CDC case. With a large total particulate volume flowing through, porosity and permeability of the filter for rich case are greatly reduced, which prevents particulates penetrating deeper.

However, the observed trend does not work for RCCI, HCCI and E85 cases. RCCI has the largest total particulate volume but shows a large penetration length. The reason of high penetration length for RCCI case is because of the particulate size distribution. The porosity and permeability of the filter for RCCI case are almost unchanged in Figure 5-36. From Figure 5-32, it can be seen that RCCI has high number of particulates with a diameter around 100 nm, which is the most penetrating particle for this specific filter. In other words, a high percent of particulates with a diameter around 100 nm will penetrate deeper into the filter. Therefore, the penetration depth is

www.manaraa.com

not only determined by the total particulate volume but also the shape of particulate size distribution.

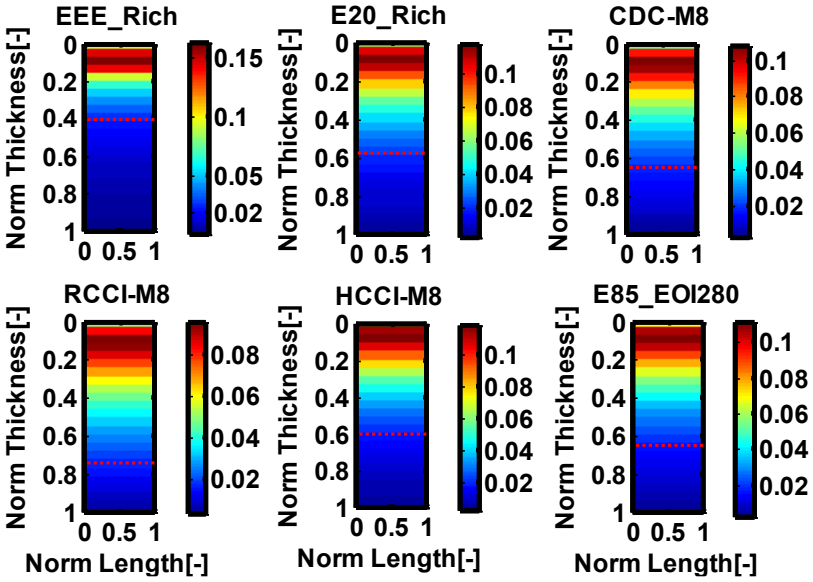

Figure 5-37: Normalized particulate mass distribution across the filter wall at t=1200s (red dashed line represents the penetration depth)

To demonstrate the importance of the shape of the particulate size distribution, another simulation was conducted by isolating the effect of total particulate volume. From Figure 5-35, the total particulate volume for RCCI case is about ten times greater than that of HCCI. A filtration study for the RCCI case was conducted for a period of 120s. The total particulate volume flow through the filter during the period of 120s for RCCI case is the same as the total particulate volume for HCCI case during a period of 1200s. It was found that the permeabilities of the filter for RCCI and HCCI cases are the same, which represents that the filter has the same macroscopic characteristic. However, the particulate mass distribution inside the wall are different from Figure 5-38. This difference demonstrates the importance of the shape of the PSD in determining the penetration depth.

www.manaraa.com

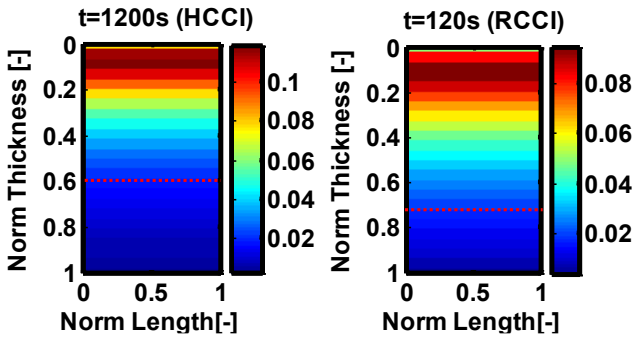

Figure 5-38: Normalized particulate mass of HCCI particulates filtration for a period of 1200s and RCCI particulates filtration for a period of 120s (red dashed line represents the penetration depth)

5.6 Summary

A PDF based heterogeneous multi-scale filtration (HMF) model was used to study the filtration characteristics of fuel neutral particulates. In the HMF model, a PDF based pore size distribution and a porosity distribution across the filter wall were introduced to represent the heterogeneous multi-scale porous filter. The HMF model was validated by fundamental filtration experimental data from different scales of filter samples. The model shows good agreement with experimental data at various operating conditions.

A dynamic filtration model based on HMF was developed to study the dynamic filtration process. It was found that the porosity distribution across the porous wall is critical and necessary to simulate filtration of particulates from gasoline and advanced diesel combustion engines.The dynamic HMF model was validated by fundamental filtration experiments conducted on a well-designed exhaust filtration analysis (EFA) system. The change of the PSDs downstream of the filter was well captured by the model. A good agreement of the evolution of the particulate number concentration in the whole range of particle sizes was observed between the model and experiments. The dynamic change of the permeability was accurately predicted by the model as

www.manaraa.com

well. It turns out that the HMF model is able to predict the dynamic filtration process for fuel-neutral particulates and is a useful diagnostic tool for filtration investigation.

Filtration simulations were conducted for six representative fuel neutral particulates from different combustion regimes with different fuels. The dynamic filtration characteristics including filtration efficiency, pressure drop and particulate distribution inside the wall were found to be strongly dependent on the total particulate volume rather than the total particulate number concentration. The penetration length is influenced by the interactions between the filter and particulates. The change of the filter structure and the shape of the particulate size distribution play an important role on particulate penetration.

www.manaraa.com

Chapter 6 - Summary and Future Work

In this chapter, a summary of the present work on $DeNO_x$ modeling and particulate filtration studies will be given. Some future work will be discussed.

6.1 Summary

6.1.1 $DeNO_x$ modeling

A TWC and a LNT model were developed with global kinetics for a $DeNO_x$ aftertreatment system on a lean-burn SIDI gasoline engine. The TWC and LNT model were validated by three types of experimental data collected on the engine dynamometer. It was found that TWC model and LNT model are able to predict the temperatures as well as species concentration with a good accuracy.

In the TWC model validations, two sets of time-resolved steady state data were first used. The model showed very good predictions of TWC wall temperature, NO_x and CO at lean and rich periods. The magnitudes and phasing of NH_3 and N_2O were captured by the model. Then, a large set of time-averaged steady state data under a wide range of engine operating conditions were used to validate the TWC model. A phasing comparison was found to be very helpful to examine the model and find the conditions at which discrepancies existed between the model and the data. Temperature dependences of the conversion rate of NH_3 and N_2O from NO_x were examined against the experimental data using the $\alpha - T$ plots. Some deviations were found in NH_3 predictions, especially at low temperatures. Finally, the model was tested at a transient FTP drive cycle with cold start conditions. Even though there were some discrepancies at the beginning of the cycle, the overall characteristics were captured.

www.manaraa.com

In the LNT model validations, a set of time-resolved steady state data was used. The catalyst wall temperature matches very well with the experimental data and the model successfully predicted the NO_x adsorption, desorption and reduction.

As part of a passive ammonia SCR system, a Pd-only TWC model was develop based on the experiments from a flow bench reactor. The TWC kinetics developed on the lean-burn SIDI engine were initially tested as a start point. It was found that the Pd-only TWC catalyst has better light-off performance compared to the Pt/Rh TWC catalyst. Re-calibrated kinetics on the Pd-only TWC show a good agreement with experimental data on CO, HCs and NO_x conversions. However, NH_3 formation kinetics need to be improved.

A global SCR model including ammonia storage, ammonia oxidation, NO oxidation, three SCR reactions and N_2O formation (standard SCR, fast SCR and NO_2 SCR) was developed on a Cu-chabazite (CHA) NH_3-SCR catalyst. Experimental data collected on a flow bench SCR reactor based on well-designed experimental SCR protocol were used for model calibrations and validations. Each SCR reaction was investigated individually. It turns out that the SCR model is able to predict the SCR performance at various operating conditions.

6.1.2 Particulate filtration

A PDF based heterogeneous multi-scale filtration (HMF) model is developed to calculate the filtration efficiency of particulate filters. In the HMF model, a new methodology based on statistical theory and classic filtration theory is presented.

Some observations from experimental pore size distribution measurements were discussed. The pore space of a filter contains a wide range of length scales, which essentially determine the

www.manaraa.com

filtration performance of the filter. A pore size probability density function based on the mean pore size and variance was introduced to represent heterogeneity and multi-scale characteristics of the porous wall. The filtration efficiency of a filter is calculated as the sum of the contributions from collectors over the pore size range. The sensitivity of the variance of pore size distribution is analyzed. The HMF model recovers the classical mean model when the pore size variance is very small. The HMF model is validated by fundamental filtration experimental data from different scales of filter samples. The HMF model overcomes the limitations of classic mean filtration models which rely on tuning of the mean collector size. The model shows good agreement with experimental data at various operating conditions. Effects of the micro-structure of filters on filtration efficiency as well as the most penetrating particle size are correctly predicted by the model.

A dynamic filtration model based on HMF was developed to study the dynamic filtration process. Fundamental filtration experimental data from EFA system were used for model validation. The change of the PSDs downstream of the filter was well captured by the model. A good agreement of the evolution of the particulate number concentration in the whole range of particle sizes was observed between the model and experiments. The dynamic change of the permeability was accurately predicted by the model as well. It turns out that the HMF model is able to predict the dynamic filtration process for fuel-neutral particulates and is a useful diagnostic tool for filtration investigation.

Various sources of particulates from combustion engines were used in the filtration studies. The micro-structure of the porous wall was found to be more critical and necessary to simulate filtration of particulates from gasoline and advanced diesel combustion engines than those from

www.manaraa.com

conventional diesel combustion engines. Six representative fuel neutral particulates from different combustion regimes with different fuels were used for filtration studies. The dynamic filtration characteristics including filtration efficiency, pressure drop and particulate distribution inside the wall were found to be strongly dependent on the total particulate volume rather than the total particulate number concentration. The penetration length is influenced by the interactions between the filter and particulates. The change of the filter structure and the shape of the particulate size distribution play important role on particulate penetration.

6.2 Future work

Based on the present work we have done on the passive ammonia SCR and particulate filtration modeling, future work are discussed in these two areas.

6.2.1 Passive ammonia SCR system modeling

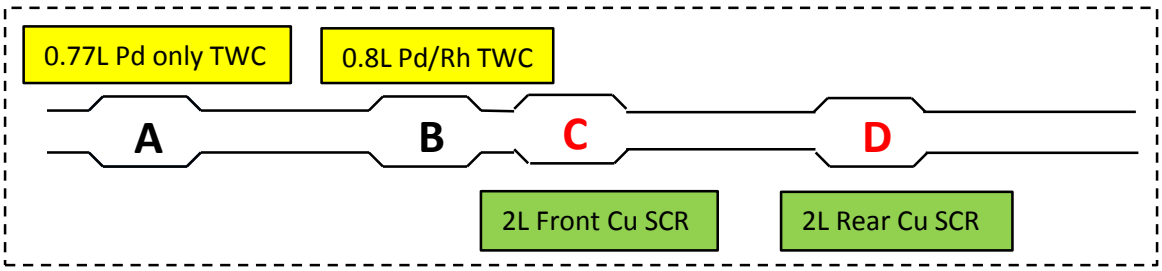

Figure 6-1: Schematic of a full scale PASS system

Once the NH_3 kinetics in the TWC are validated from the flow bench reactor data, the TWC model can be applied to study the combined TWC and SCR system. Experimental data generated from the full scale PASS system integrated in a SIDI engine dynamometer at GM can be used to validate and test the model. Figure 6-1 shows the configuration of a full scale PASS system. There are

www.manaraa.com

some challenges to simulate the full scale PASS on an engine dynamometer. One of the challenges is heat transfer modeling on the exhaust pipes that connecting the TWC and SCR.

Once the integrated TWC and SCR model is validated on the engine dynamometer experiments, the model can be used to explore the optimum engine control strategies by minimizing rich operating period (less fuel penalty) while meeting the NO_x emission requirement.

One of the other interesting thing is to look at is the ammonia and CO/HC slip. It was found that a long rich operation period in order to generate enough ammonia could potentially resulte in ammonia and CO/HCs slip through the downstream SCR catalyst. This is because the ammonia generated by TWC may slip if the SCR is not able to store them. The TWC catalyst has relatively low CO and HCs conversion efficiencies at rich conditions. Therefore, there are lots of opportunities on engine control strategies development as well as aftertreatment system optimizations.

6.2.2 Filtration model development

Even though the dynamic HMF model has been developed, there are limited validations from fundamental filtration data. More filtration experiments from EFA system on advanced filters will be extremely helpful to improve the model. A set of filtration experimental data were recently collected by Viswanathan et al. [173], which can be used for model validations. Four engine operating conditions were selected with unique PSDs that differed in total number concentration as shown in Table 6-1.

www.manaraa.com

Table 6-1: Engine operating conditions

Condition	Speed	Injection Timing	IMEP	AFR	CA-50	Spark Timing	Injection Press	Total PM
	[RPM]	[°bTDC]	[kPa]	[-]	[°aTDC]	[°bTDC]	[MPa]	*1E5[#/cm^3]
Rich	2100	220	300 (±5)	13	6.7 (±0.5)	25	11	178
EOI220	2100	220	330 (±6)	15	6.7 (±0.5)	25	11	16
MBT-15	2100	220	275 (±12)	15	28 (±2.0)	12	11	8.3
EOI280	2100	280	350 (±5)	15	8.8 (±0.5)	25	11	0.51

Most of filtration models in the literature treat particulates as an idealized sphere [103,174,175]. This assumption probably works fine for modeling particulate filtration in DPFs for diesel engines, since particulates from diesel engine have more compact and larger aggregates and less nuclei mode aggregates. However, the characteristics and chemical compositions of the particulate emission varies a lot for advanced diesel combustion (PCCI, RCCI) engines as well as SIDI engines fueled with gasoline ethanol blends and other alternative fuels[91,176,177,178]. From morphology perspective, particulates from EEE gasoline and E20 showed more open and branched aggregates with chain-like fractals consist of small and large primary particles compared to more dense and compact aggregates from E85 under the same engine operating conditions (Ø=0.98 and EOI 280° bTDC) in Figure 6-2.

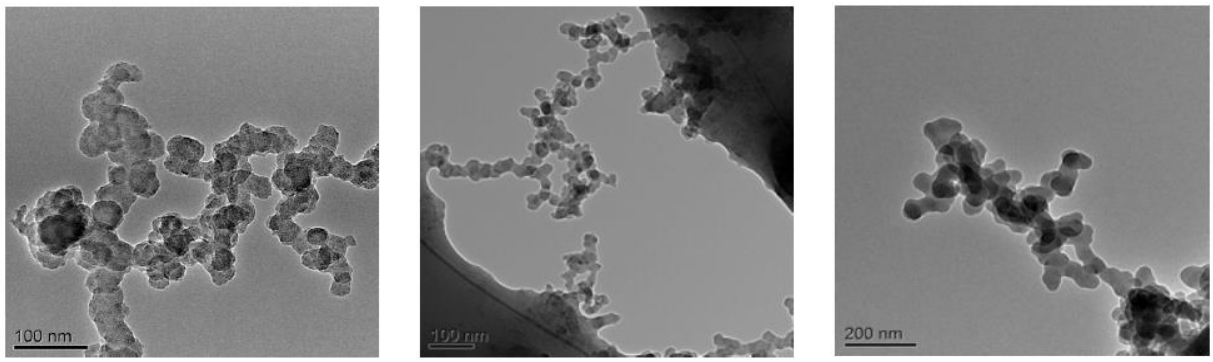

Figure 6-2: TEM micrographs of the aggregates morphology for the particulates from (a) EEE gasoline (b) E20 (c) E85 at Ø=0.98 and EOI 280° bTDC [178]

www.manaraa.com

It will be necessary and interesting to apply the morphology of the particulates into the filtration modeling rather than only using a size distribution and assuming each particulate is a sphere. The morphology and structural properties of particulates can be measured using transmission electron microscopy (TEM). Through the morphology analysis, some critical properties of the particulates will be determined to represent the realistic particulates. As discussed above, the fractal dimension, dynamic shape factor and inherent material density are proposed to be good candidates to represent the particulate morphology. Eventually, correlations for each of these critical properties will be derived from the particulate morphology analysis. For example, the correlation of the dynamic shape factor to particulate mobility diameter was found by Park et al. [179].

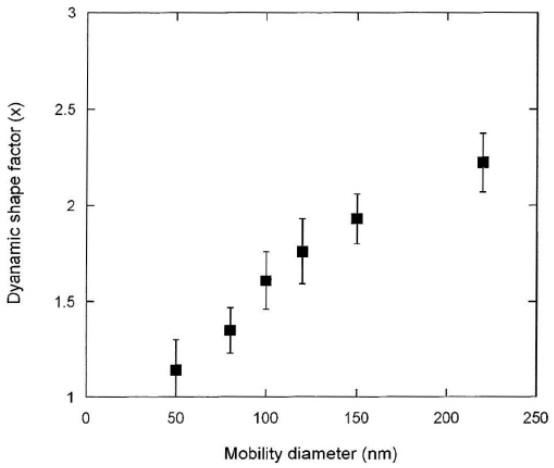

Figure 6-3: dynamic shape factor as a function of mobility diameter [179]

Regeneration characteristics are also very important for development of particulate filters. GPF regeneration will be interesting since the soot particulates reaction kinetics will be different due to the characteristics of the particulates from gasoline engines. The regeneration conditions, for instance, the oxygen concentration, NO_2 availability and exhaust temperature, are distinct to that of DPF regenerations. GPF regeneration control strategies (active or passive) need to be investigated as well.

www.manaraa.com

Appendix A : Summary of flow field

Table A 1: Summary of solutions of Stokes flow around spheres

Expression	
$\psi(r,\theta)=\frac{3}{4}\cdot H(\beta,\mathrm{Re})a^2U_0\left(\frac{r-a}{a}\right)^2\sin^2\theta$	(In the near vicinity of the sphere (r-a)/a<<1)
$H=1$	Isolated sphere
$H=\frac{1-\beta^{5/3}}{H_s}$, $H_s=1-\frac{3}{2}\beta^{1/3}+\frac{3}{2}\beta^{5/3}-\beta^2$	A system of spheres; with Happel boundary conditions
$H=\frac{\varepsilon}{K_s}$, $K_s=1-\frac{9}{5}\beta^{1/3}-\frac{1}{5}\beta^2+\beta$	A system of spheres; with Kuwabara boundary conditions

Table A 2: Summary of solutions of Stokes flow around cylinders

Expression	
$\psi(\rho,\theta)=\frac{aU_0}{2H(\beta,\mathrm{Re})}\left(\frac{a}{\rho}-\frac{\rho}{a}+2\frac{\rho}{a}\ln\frac{\rho}{a}\right)\sin\theta$	
$H=2-\ln\mathrm{Re}$	Isolated cylinder; Lamb approximation (from Oseen's approximation)
$H=-\frac{1}{2}-\frac{1}{2}\ln\beta+\frac{\beta^2}{1+\beta}$	A system of cylinders with Happel boundary conditions
$H=-\frac{3}{4}-\frac{1}{2}\ln\beta+\beta-\frac{1}{4}\beta^2$	A system of cylinders; with Kuwabara boundary conditions

www.manaraa.com

Appendix B : Summary of filtration mechanisms

Mechanisms	Description
Diffusion	• The trajectories of individual small particles do not coincide with the streamlines of the fluid because of Brownian motion. • With decreasing particle size, the intensity of the Brownian motion increases and so does the intensity of the diffusion deposition.
Direct interception	• A particle is intercepted as it approaches the collecting surface to a distance equal to its radius.
Inertial	• The individual particles do not follow the curved streamlines due to the inertia of the particles • The intensity of inertia mechanism increases with increasing particle size and velocity of flow.
Gravitational	• Individual particles have a certain sedimentation velocity due to gravity. The trajectory of particles deviates from the streamlines of the fluid and the particles may deposit there.
Electrostatic	• Particles and porous medium may carry electric charges. Deposition of particles may take place because of the force between charges or induced forces.
London-Van der Waals	• Deposition may be influenced by London-van der Waals forces when the distance between a particle and the porous medium element is very small.

www.manaraa.com

Appendix C : TWC kinetics

The specific reaction rate is in the form of $r_i = k_i \cdot [concentration] \cdot f(G_i) \cdot C(\theta_i)$. Rate coefficient is in the form of $k_i = A_i \cdot T^{b_i} \exp(-\frac{E_i}{R_u T})$. Units are moles, cubic meters, seconds and Kelvin.

No.	*Reaction*	*A*	*b*	*E(J/mole)*	*Conc*f(Gi)*	*C(θ)*
1	$CO + 0.5O_2 \rightarrow CO_2$	3.642E+13	0	138450	$[CO]*[O_2]/G(1)$	1
2	$C_3H_6 + 4.5O_2 \rightarrow 3CO_2 + 3H_2O$	3.170E+13	0	130530	$[C_3H_6]*[O_2]/G(1)$	1
3	$C_3H8 + 5O_2 \rightarrow 3CO_2 + 4H_2O$	9.404E+14	0	165160	$[C_3H_8]*[O_2]/G(1)$	1
4	$H_2 + 0.5O_2 \rightarrow H_2O$	1.67E+13	0	111450	$[H_2]*[O_2]/G(1)$	1
5	$CO + NO \rightarrow CO_2 + 0.5N_2$	3.154E+09	0	52374	$[CO]*[NO]/G(1)$	1
6	$C_3H_6 + 9NO \rightarrow 3CO_2 + 3H_2O + 4.5N_2$	6.242E+09	0	80063	$[C_3H_6]*[NO]/G(1)$	1
7	$H_2 + NO \rightarrow H_2O + 0.5N_2$	4.642E+08	0	69237	$[H_2]*[NO]/G(1)$	1
8	$CO + H_2O \leftrightarrow CO_2 + H_2$	1.800E+00	0	56720	$([CO]*[H_2O]-[H_2]*[CO_2]/G(2))/G(1)$	1
9	$C_3H_6 + 3H_2O \rightarrow 3CO + 6H_2$	1.230E+05	0	81920	$[C_3H_6]*[H_2O]/G(1)$	1
10	$NH_3+1.25O_2 \rightarrow NO+1.5H_2O$	3.000E+13	0	139300	$[NH_3]*[O_2]/G(1)$	1
11	$NO+2.5H_2 \rightarrow NH_3+H_2O$	7.390E+09	0	44720	$[NO]*[H_2]/G(1)$	1
12	$NH_3+1.5NO \rightarrow 1.25N_2+1.5H_2O$	1.500E+10	0	121400	$[NH_3]*[NO]/G(1)$	1
13	$NO+1/18C_3H_6 \rightarrow 0.5N_2O+1/6CO_2+1/6H_2O$	6.720E+12	0	83700	$[NO]*[C_3H_6]*G(3)/G(1)$	1
14	$N_2O+1/9C_3H_6 \rightarrow N_2+1/3CO_2+1/3H_2O$	1.200E+15	0	135000	$[N_2O]*[C_3H_6]/G(1)$	1
15	$2Ce_2O_3 + O_2 \rightarrow 4CeO_2$	2.943E+00	0	5296	$[O_2]$	1-θ
16	$Ce_2O_3 + NO \rightarrow 2CeO_2 + 0.5N_2$	7.920E+02	0	25101	$[NO]$	1-θ
17	$CO + 2CeO_2 \rightarrow Ce_2O_3 + CO_2$	1.824E-01	0	31768	$[CO]$	θ
18	$C_3H_6 + 12CeO_2 \rightarrow 6Ce_2O_3 + 3CO + 3H_2O$	1.357E+01	0	39070	$[C_3H_6]$	θ
19	$C_3H_8 + 14CeO_2 \rightarrow 7Ce_2O_3 + 3CO + 4H_2O$	1.770E+01	0	39680	$[C_3H_8]$	θ
20	$H_2 + 2CeO_2 \rightarrow Ce_2O_3 + H_2O$	2.845E+00	0	31768	$[H_2]$	θ

The inhibition functions used in the rate equations are:

$$G(1) = \left(1+4.314\cdot\exp(\frac{485}{T_s})\cdot[CO]+1.289\cdot\exp(-\frac{166}{T_s})\cdot[C_3H_6]\right)^2 \cdot \left(1+2.147E-4\cdot\exp(\frac{10163}{T_s})\cdot[CO]^2\cdot[C_3H_6]^2\right)\cdot\left(1+8.699E5\cdot\exp(-\frac{3685}{T_s})\cdot[NO]\right)$$

$$G(2) = \exp\left(-\frac{-41034+44.19T_s-5.553E-3T_s^2}{8.314\cdot T_s}\right)$$

$$G(3) = f_0 + \exp\left(-\frac{(T_s-T_{m1})^2}{\sigma_1}\right)\cdot\exp\left(-\frac{(T_s-T_{m2})^2}{\sigma_2}\right)$$

www.manaraa.com

Reaction constants comparison between Pt/Rh TWC and Pd-only TWC

TWC kinetics			Gong et al. 2013		Pd-only TWC	
Rxn #	Reactants	Products	pre-exp	Ea J/mole	pre-exp	Ea J/mole
1	CO + 0.5O2	CO2	3.642E+13	138450	3.54E+12	110450
2	C3H6 + 4.5O2	3CO2 + 3H2O	3.170E+13	130530	5.92E+13	120530
3	C3H8 + 5O2	3CO2 + 4H2O	9.404E+14	165160	9.404E+14	165160
4	H2 + 0.5O2	H2O	1.67E+13	111450	1.67E+12	111450
5	CO + NO	CO2 + 0.5N2	3.154E+09	52374	2.154E+09	52374
6	C3H6 + 9NO	3CO2 + 3H2O + 4.5N2	6.242E+09	80063	8.242E+09	80063
7	H2 + NO	H2O + 0.5N2	4.642E+08	69237	4.642E+08	69237
8	CO + H2O	CO2 + H2	1.800E+05	56720	1.800E+05	56720
9	C3H6 + 3H2O	3CO + 6H2	1.230E+05	81920	6.430E+06	53620
10	2Ce2O3 + O2	4CeO2	2.943E+00	5296	2.943E+00	5296
11	Ce2O3 + NO	2CeO2 + 0.5N2	7.920E+02	25101	7.920E+02	25101
12	CO + 2CeO2	Ce2O3 + CO2	1.824E-01	31768	1.824E-01	31768
13	C3H6 + 12CeO2	6Ce2O3 + 3CO + 3H2O	1.357E+01	39070	1.357E+01	39070
14	C3H8 + 14CeO2	7Ce2O3 + 3CO + 4H2O	1.770E+01	39680	1.770E+01	39680
15	H2 + 2CeO2	Ce2O3 + H2O	2.845E+00	31768	2.845E+00	31768
16	NH3+1.25O2	NO+1.5H2O	3.000E+13	139300	3.000E+13	139300
17	NO+2.5H2	NH3+H2O	7.390E+09	44720	7.390E+09	44720
18	NH3+1.5NO	1.25N2+1.5H2O	1.500E+10	121400	1.500E+10	121400
19	NO+1/18C_3H_6	0.5N_2O+1/6CO_2+1/6H_2O	6.720E+12	83700	2.720E+12	83700
20	N_2O+1/9C_3H_6	N_2+1/3CO_2+1/3H_2O	1.200E+15	135000	1.200E+15	135000

www.manaraa.com

Appendix D : LNT kinetics

No.	*Reaction*	*A*	*b*	*E(J/mole)*	*Conc*f(Gi)*	*C(θ)*
1	$CO+0.5O_2 \rightarrow CO_2$	1.28E+08	0	104400	{CO}*{O_2}/G(1)	1
2	$C_3H_6+4.5O_2 \rightarrow 3CO_2 + 3H_2O$	1.20E+09	0	105000	{C_3H_6}*{ O_2}/G(1)	1
3	$C_3H_8+ 5O_2 \rightarrow 3CO_2 + 4H_2O$	2.50E+09	0	109000	{C_3H_8}*{ O_2}/G(1)	1
4	$H_2 + 0.5O_2 \leftrightarrow H_2O$	3.50E+10	0	100100	{H_2}*{ O_2}/G(1)	1
5	$NO+0.5\ O_2 \rightarrow NO_2$	75.1	0	39200	{NO}*{ O_2}^0.5-{NO_2}/G(4)	1
6	$CO + NO \rightarrow CO_2 + 0.5N_2$	4.51E+08	0	50500	{CO}^(1.9)*{NO}^(0.13)*G(5)/G(2)	1
7	$1/9C_3H_6+NO \rightarrow 1/3CO_2+1/3H_2O+1/2\ N_2$	5.29E9	0	60000	{NO}^0.13*{C_3H_6}	1
8	$0.5BaCO_3+NO+0.75O_2 \rightarrow 0.5Ba(NO_3)_2+0.5CO_2$	2.27E+08	0	73300	{NO}*{O_2}^(0.25)/G(3)	θ
9	$0.5BaCO_3+NO_2+0.25O_2 \rightarrow 0.5Ba(NO_3)_2+0.5CO_2$	4.67E+07	0	83700	{NO_2}*{O_2}^(0.25)/G(3)	θ
10	$0.5Ba(NO_3)_2+1.5CO \rightarrow 0.5BaCO_3+NO+CO_2$	1.5E+07	0	142700	{CO}	$(1-\theta)^{0.3}$
11	$Ba(NO_3)_2+1/3C_3H_6+CO_2 \rightarrow BaCO_3+2\ NO+H_2O$	5.09E+09	0	121300	{C_3H_6}	$(1-\theta)^{0.3}$
12	$Ba(NO_3)_2+8H_2+CO_2 \rightarrow 2NH_3+BaCO_3+5H_2O$	6.532	0	81400	{H_2}	$(1-\theta)^{0.3}$
13	$NH_3+0.5Ba(NO_3)_2+0.5CO_2 \rightarrow N_2O+0.5BaCO_3+1.5H_2O$	10	0	131400	{NH_3}	$(1-\theta)^{0.3}$
14	$NH_3+4NO \rightarrow 2.5N_2O+1.5H_2O$	1.00E+08	0	121400	{NH_3}*{NO}/G(1)	1
15	$NO+2.5H_2 \rightarrow NH_3+H_2O$	3532000	0	42720	{NO}*{H_2}/G(1)	1
16	$NH_3+1.25O_2 \rightarrow NO+1.5H_2O$	3.00E+10	0	169300	{NH_3}*{O_2}/G(1)	1
17	$NH_3+1.5NO \rightarrow 1.25N_2+1.5H_2O$	1.00E+10	0	121400	{NH_3}*{NO}^0.5/G(1)	1

The inhibition functions used in the rate equations are:

$$G(1) = T_s \cdot \left\{ \left(1 + 65.6 \cdot \exp\left(\frac{961}{T_s} \right) \right) \cdot [CO] + 2.08\text{E}3 \cdot \exp\left(\frac{361}{T_s} \right) \cdot [C_3H_6] \right\}^2 \cdot \left[1 + 3.98 \cdot \exp\left(\frac{11611}{T_s} \right) \cdot [CO]^2 \cdot [C_3H_6]^2 \right] \cdot \left[1 + 4.79\text{E}5 \cdot \exp\left(-\frac{3733}{T_s} \right) \cdot [NO]^{0.7} \right]$$

$$G(2) = T_s^{-0.17} \cdot \left[T_s + 1.2E5 \cdot \exp\left(\frac{653}{T_s} \right) \cdot [CO] \right]^2$$

$$G(3) = 1 + 4.7E10 \cdot \exp\left(-\frac{75.3E3}{R_u T_s} \right) \cdot \frac{100E-9 \cdot (1-\theta)^{1/3}}{4.9E-9} \cdot \theta^{1/3}$$

$$G(4) = \exp\left[-\left(\frac{76.1 \cdot T_s - 58E3}{R_u \cdot T_s} \right) \right] \cdot \left(\frac{R_u \cdot T_s}{P_{amb}} \right)^{0.5}$$

www.manaraa.com

Appendix E : TWC model validation

Time-resolved validation at 4000 rpm and 50% load

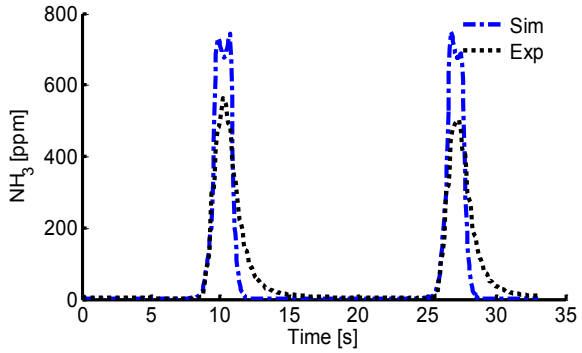

Figure F 1: TWC ammonia concentration comparison at 4000 rpm, 50% load

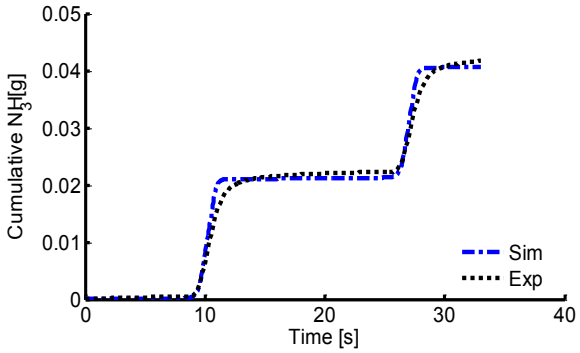

Figure F 2: TWC cumulative ammonia concentration comparison at 4000 rpm, 50% load

Time-averaged validation

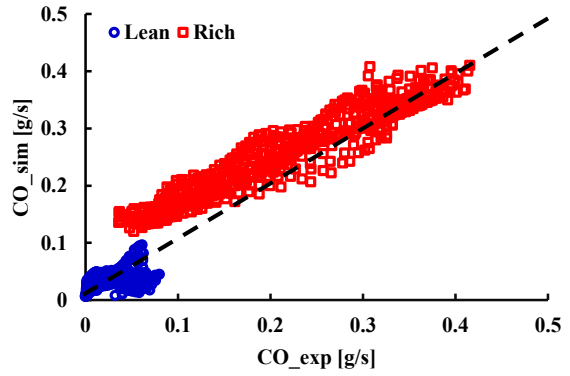

Figure F 3: Comparison of time-averaged CO emission at lean (blue) and rich (red) periods

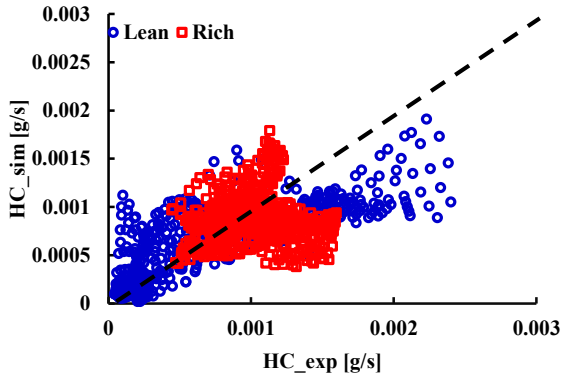

Figure F 4: Comparison of time-averaged hydrocarbon emission at lean (blue) and rich (red) periods

www.manaraa.com

Transient FTP Cycle validation

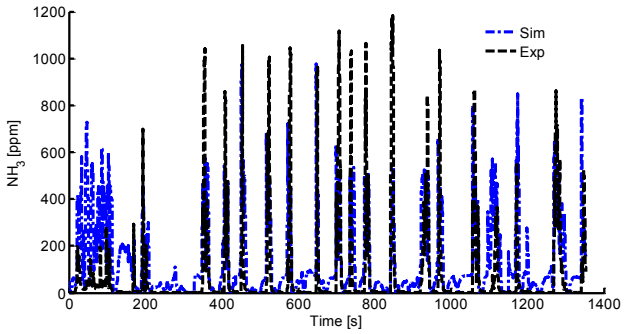

Figure F 5: Cumulative NH_3 comparison at FTP cold cycle

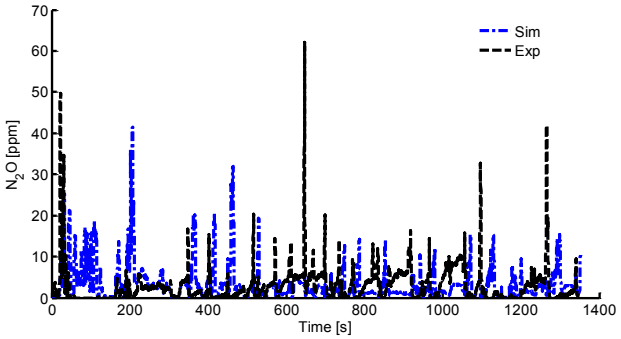

Figure F 6: Cumulative N_2O comparison at FTP cold cycle

www.manaraa.com

References

1 Noma, K., Iwamoto, Y., Murakami, N., Iida, K. et al., "Optimized Gasoline Direct Injection Engine for the European Market," SAE Technical Paper 980150, 1998, doi:10.4271/980150.

2 Spicher, U., Reissing, J., Kech, J., and Gindele, J., "Gasoline Direct Injection (GDI) Engines - Development Potentialities," SAE Technical Paper 1999-01-2938, 1999, doi:10.4271/1999-01-2938.

3 Ando, H. and Kuwahara, K., "A Keynote on Future Combustion Engines," SAE Technical Paper 2001-01-0248, 2001, doi:10.4271/2001-01-0248.

4 Zhao F., Lai M., and Harrington D. L., "Automotive spark-ignited direct-injection gasoline engines," Progress in Energy and Combustion Science, 25(5), pp. 437-562, 1999.

5 Akihama, K., Takatori, Y., Inagaki, K., Sasaki, S. et al., "Mechanism of the Smokeless Rich Diesel Combustion by Reducing Temperature," SAE Technical Paper 2001-01-0655, 2001, doi:10.4271/2001-01-0655.

6 Mital, R., Li, J., Huang, S., Stroia, B. et al., "Diesel Exhaust Emissions Control for Light Duty Vehicles," SAE Technical Paper 2003-01-0041, 2003, doi:10.4271/2003-01-0041.

7 Neely, G., Sasaki, S., Huang, Y., Leet, J. et al., "New Diesel Emission Control Strategy to Meet US Tier 2 Emissions Regulations," SAE Technical Paper 2005-01-1091, 2005, doi:10.4271/2005-01-1091.

8 Toops, Todd J., Parks, James E., Pihl, Josh A., DiGiulio, Christopher D., Amiridis, Michael D. DEER Conference, October 18, 2012

9 Cole, R., Poola, R., and Sekar, R., "Exhaust Emissions of a Vehicle with a Gasoline Direct-Injection Engine," SAE Technical Paper 982605, 1998, doi:10.4271/982605.

10 Kaiser, E., Siegl, W., Brehob, D., and Haghgooie, M., "Engine-Out Emissions from a Direct-Injection Spark-Ignition (DISI) Engine," SAE Technical Paper 1999-01-1529, 1999, doi:10.4271/1999-01-1529.

11 Zhang, S. and McMahon, W., "Particulate Emissions for LEV II Light-Duty Gasoline Direct Injection Vehicles," SAE Int. J. Fuels Lubr. 5(2):637-646, 2012, doi:10.4271/2012-01-0442.

www.manaraa.com

12 Flynn P. F., Hunter G. L., Farrel L., Durrett R. P., Akinyemi O., Loye A. O. Z., Westbrook C. K., and Pitz W. J., “The inevitability of engine-out NO_x emissions from spark-ignited and diesel engines,” Proceedings of the Combustion Institute, 28(1), pp. 1211-1218, 2000.

13 Johnson, T., "Vehicular Emissions in Review," SAE Int. J. Engines 5(2):2012, doi:10.4271/2012-01-0368.

14 Piock, W., Hoffmann, G., Berndorfer, A., Salemi, P. et al., "Strategies Towards Meeting Future Particulate Matter Emission Requirements in Homogeneous Gasoline Direct Injection Engines," SAE Int. J. Engines 4(1):1455-1468, 2011, doi:10.4271/2011-01-1212.

15 Braisher, M., Stone, R., and Price, P., "Particle Number Emissions from a Range of European Vehicles," SAE Technical Paper 2010-01-0786, 2010, doi:10.4271/2010-01-0786.

16 Yassine, M. and La Pan, M., "Impact of Ethanol Fuels on Regulated Tailpipe Emissions," SAE Technical Paper 2012-01-0872, 2012, doi:10.4271/2012-01-0872.

17 Oh, H., Bae, C., and Min, K., "Spray and Combustion Characteristics of Ethanol Blended Gasoline in a Spray Guided DISI Engine under Lean Stratified Operation," SAE Int. J. Engines3(2):213-222, 2010, doi:10.4271/2010-01-2152.

18 Olsson L., Fredriksson M., and Blint R. J., “Applied Catalysis B : Environmental Kinetic modeling of sulfur poisoning and regeneration of lean NOx traps,” “Applied Catalysis B, Environmental,” 100(1-2), pp. 31-41, 2010.

19 Shamim T., Shen H., Sengupta S., Son S., and Adamczyk A. A., “A Comprehensive Model to Predict Three-Way Catalytic,” Journal of Engineering for Gas Turbines and Power, 124(April), pp. 421-428,2002.

20 Pontikakis G. N., Konstantas G. S., and Stamatelos A. M., “Three-Way Catalytic Converter Modeling as a Modern,” Journal of Engineering for Gas Turbines and Power, 126(October), pp. 906-923, 2004.

21 Li, W., Perry, K., Narayanaswamy, K., Kim, C. et al., "Passive Ammonia SCR System for Lean-burn SIDI Engines," SAE Int. J. Fuels Lubr. 3(1):99-106, 2010, doi:10.4271/2010-01-0366

22 Kim, C., Perry, K., Viola, M., Li, W. et al., "Three-Way Catalyst Design for Urealess Passive Ammonia SCR: Lean-Burn SIDI Aftertreatment System," SAE Technical Paper 2011-01-0306, 2011, doi:10.4271/2011-01-0306

23 Roy, S., and Baiker, A., 2009, “NOx storage-reduction catalysis: from mechanism and materials properties to storage-reduction performance.,” Chem. Rev., 109(9), pp. 4054–91.

www.manaraa.com

24 Pereda-Ayo, B., López-Fonseca, R., & González-Velasco, J. R. (2009). Influence of the preparation procedure of NSR monolithic catalysts on the Pt-Ba dispersion and distribution. *Applied Catalysis A: General*, *363*(1), 73-80.

25 Abdulhamid, H., Fridell, E., & Skoglundh, M. (2004). Influence of the type of reducing agent (H2, CO, C3H6 and C3H8) on the reduction of stored NO X in a Pt/BaO/Al2O3 model catalyst. *Topics in catalysis*, *30*(1-4), 161-168.

26 Tronconi, E., Nova, I., Ciardelli, C., Chatterjee, D., Bandl-Konrad, B., and Burkhardt, T., 2005, "Modelling of an SCR catalytic converter for diesel exhaust after treatment: Dynamic effects at low temperature," Catal. Today, 105(3-4), pp. 529–536.

27 Schmieg, S., Sloane, T., and Blint, R., "Catalysts for Lean-Burn Engine Exhaust Aftertreatment Using Hydrocarbon Selective Catalytic Reduction," *SAE Int. J. Fuels Lubr.* 2(2):323-336, 2010, doi:10.4271/2009-01-2819.

28 Subbiah, A., Cho, B. K., Blint, R. J., Gujar, A., Price, G. L., and Yie, J. E., 2003, "NOx reduction over metal-ion exchanged novel zeolite under lean conditions: activity and hydrothermal stability," Appl. Catal. B Environ., 42(2), pp. 155–178.

29 Chatterjee, D., Burkhardt, T., Weibel, M., Nova, I. et al., "Numerical Simulation of Zeolite- and V-Based SCR Catalytic Converters," SAE Technical Paper 2007-01-1136, 2007, doi:10.4271/2007-01-1136.

30 Wilken, N., Wijayanti, K., Kamasamudram, K., Currier, N. W., Vedaiyan, R., Yezerets, A., and Olsson, L., 2011, "Mechanistic investigation of hydrothermal aging of Cu-Beta for ammonia SCR," Appl. Catal. B Environ., 111-112(3), pp. 58–66.

31 Kamasamudram, K., Currier, N. W., Chen, X., and Yezerets, A., 2010, "Overview of the practically important behaviors of zeolite-based urea-SCR catalysts, using compact experimental protocol," Catal. Today, 151(3-4), pp. 212–222.

32 Voltz, S. E., Morgan, C. R., Liederman, D., and Jacob, S. M., 1973, "Kinetic Study of Carbon Monoxide and Propylene Oxidation on Platinum Catalysts," Ind. Eng. Chem. Prod. Res. Dev., 12(4), pp. 294–301.

33 Dubien, C., Schweich, D., Mabilon, G., Martin, B., & Prigent, M. (1998), "Three-way catalytic converter modelling: fast-and slow-oxidizing hydrocarbons, inhibiting species, and steam-reforming reaction", Chemical Engineering Science, 53(3), 471-481.

www.manaraa.com

34 Shamim, T., Shen, H., Sengupta, S., Son, S., and Adamczyk, a. a., 2002, “A Comprehensive Model to Predict Three-Way Catalytic Converter Performance,” J. Eng. Gas Turbines Power, 124(2), p. 421.

35 Pontikakis, G. N., Konstantas, G. S., and Stamatelos, a. M., 2004, “Three-Way Catalytic Converter Modeling as a Modern Engineering Design Tool,” J. Eng. Gas Turbines Power, 126(4), p. 906.

36 Botas, J. a, Gutiérrez-Ortiz, M. a, González-Marcos, M. P., González-Marcos, J. a, and González-Velasco, J. R., 2001, “Kinetic considerations of three-way catalysis in automobile exhaust converters,” Appl. Catal. B Environ., 32(4), pp. 243–256.

37 Kaspar J., Fornasiero P., and Graziani M., “Use of CeO 2 -based oxides in the three-way catalysis,” Catalysis Today, 50, pp. 285-298, 1999.

38 Koltsakis, G. C., Konstantinidis, P. a., and Stamatelos, a. M., 1997, “Development and application range of mathematical models for 3-way catalytic converters,” Appl. Catal. B Environ., 12(2-3), pp. 161–191.

39 Odaka, M., Koike, N., and Suzuki, H., "Deterioration Effect of Three-way Catalyst on Nitrous Oxide Emission," SAE Technical Paper 980676, 1998, doi:10.4271/980676.

40 Takei, M., Matsuda, H., Itaya, Y., Deguchi, S., Nakano, K., Nagahashi, K., Yoshino, M., Shibata, J., and Hasatani, M., 1998, “NO reduction and the formation of nitrogen compounds over a metal-supported three-way catalyst,” Fuel, 77(9-10), pp. 1027–1031.

41 Li, W., Perry, K., Narayanaswamy, K., Kim, C. et al., "Passive Ammonia SCR System for Lean-burn SIDI Engines," *SAE Int. J. Fuels Lubr.* 3(1):99-106, 2010, doi:10.4271/2010-01-0366.

42 Kim, C., Perry, K., Viola, M., Li, W. et al., "Three-Way Catalyst Design for Urealess Passive Ammonia SCR: Lean-Burn SIDI Aftertreatment System," SAE Technical Paper 2011-01-0306, 2011, doi:10.4271/2011-01-0306.

43 Lindholm, A.; Currier, N.; Yezerets, A.; Olsson, L., “A kinetic study of NO_x reduction over Pt/SiO_2 model catalysts with hydrogen as the reducing agent”. Topics in Catalysis, 42-43 (1), 83–89, 2007

44 Pihl, J., Parks, J., Daw, C., and Root, T., "Product Selectivity During Regeneration of Lean NO_x Trap Catalysts," SAE Technical Paper 2006-01-3441, 2006, doi:10.4271/2006-01-3441.

www.manaraa.com

45 Clayton, R. D.; Harold, M. P.; Balakotaiah, V. "NO_x storage and reduction with H_2 on Pt/BaO/Al2O3 monolith: Spatio-temporal resolution of product distribution", Appl. Catal., B, 84(3-4), 616–630, 2008.

46 Mulla S. S., Chaugule S. S., Yezerets A., Currier N. W., Delgass W. N., and Ribeiro F. H., "Regeneration mechanism of Pt/BaO/Al2O3 lean NO_x trap catalyst with H_2," Catalysis Today, 136(1-2), pp. 136-145, 2008.

47 Kocí, P.; Plat, F.; Stepanek, J.; Bartova, S.; Marek, M.; Kubícek, M.; Schmeißer, V.; Chatterjee, D.; Weibel, M. "Global kinetic model for the regeneration of NO_x storage catalyst with CO, H_2, and C3H6 in the presence of CO_2 andH_2O", Catalysis Today, 147S, S257–S264,2009.

48 Lietti, L.; Nova, I.; Forzatti, P., "Role of ammonia in the reduction by hydrogen of NO_x stored over Pt-Ba/Al_2O_3 lean NO_x trap catalysts", Journal of Catalysis, 257 (2), 270–282,2008.

49 DiGiulio, C. D., Pihl, J. a., Ii, J. E. P., Amiridis, M. D., and Toops, T. J., 2014, "Passive-ammonia selective catalytic reduction (SCR): Understanding NH3 formation over close-coupled three way catalysts (TWC)," Catal. Today, 231(X), pp. 33–45.

50 Graham L. A., Belisle S. L., and Rieger P., "Nitrous oxide emissions from light duty vehicles," Atmospheric Environment, 43(12), pp. 2031-2044, 2009.

51 Kamasamudram, K., Henry, C., Currier, N. and Yezerets, A., "N_2O Formation and Mitigation in Diesel Aftertreatment Systems," SAE Int. J. Engines 5: doi:10.4271/2012-01-1085

52 Cant N. W., Angove D. E., and Chambers D. C., "Nitrous oxide formation during the reaction of simulated exhaust streams over rhodium , platinum and palladium catalysts," Applied Catalysis, 17, pp. 63-73, 1998.

53 Mejía-Centeno, I., and Fuentes, G. a., 2009, "Nitrous Oxide Formation During Light-Off Over a Commercial Pd-Containing Three-Way Catalytic Converter: the Effect of Low-Sulfur Gasoline," Chem. Eng. Commun., 196(10), pp. 1140–1151.

54 Mejía-Centeno, I., Castillo, S., and Fuentes, G. a., 2012, "Enhanced emissions of NH3, N2O and H2 from a Pd-only TWC and supported Pd model catalysts: Light-off and sulfur level studies," Appl. Catal. B Environ., 119-120, pp. 234–240.

55 Epling W. S., Campbell L. E., Yezerets A., Currier N. W., and Parks II J. E., "Overview of the Fundamental Reactions and Degradation Mechanisms of NO_x Storage/Reduction Catalysts," Catalysis Reviews, 46(2), pp. 163-245, 2004.

www.manaraa.com

56 Kodama, Y. and Wong, V., "Study of On-Board Ammonia (NH3) Generation for SCR Operation," *SAE Int. J. Fuels Lubr.* 3(1):537-555, 2010, doi:10.4271/2010-01-1071.

57 Lindholm A., Currier N. W., Li J., Yezerets A., and Olsson L., "Detailed kinetic modeling of NO_x storage and reduction with hydrogen as the reducing agent and in the presence of CO_2 and H_2O over a Pt/Ba/Al catalyst," Journal of Catalysis, 258, pp. 273-288, 2008.

58 Lindholm, a, Currier, N., Li, J., Yezerets, a, and Olsson, L., 2008, "Detailed kinetic modeling of NOx storage and reduction with hydrogen as the reducing agent and in the presence of CO2 and H2O over a Pt/Ba/Al catalyst," J. Catal., 258(1), pp. 273–288.

59 Votsmeier M., Scheuer A., Drochner A., Vogel H., and Gieshoff J., "Simulation of automotive NH3 oxidation catalysts based on pre-computed rate data from mechanistic surface kinetics," Catalysis Today, 151(3-4), pp. 271-277,2010. 151 (34), 271–277.

60 Kocí, P.; Plat, F.; Stepanek, J.; Kubícek, M.; Marek, M. "Dynamics and selectivity of NO_x reduction in NO_x storage catalytic monolith", Catalysis Today 137 (2-4), 253–260, 2008.

61 Kocí, P.; Plat, F.; Stepanek, J.; Bartova, S.; Marek, M.; Kubícek, M.; Schmeißer, V.; Chatterjee, D.; Weibel, M. "Global kinetic model for the regeneration of NO_x storage catalyst with CO, H_2, and C3H6 in the presence of CO_2 andH_2O", Catalysis Today, 147S, S257–S264,2009

62 Chatterjee, D.; Kocí, P.; Schmeißer, V.; Marek, M.; Weibel, M.; Krutzsch, B., "Modelling of a combined NO_x storage and NH_3-SCR catalytic system for Diesel exhaust gas aftertreatment", Catalysis Today, 151 (3-4), 395–409, 2010

63 Olsson L., Persson H., Fridell E., Skoglundh M., and Andersson B., "A Kinetic Study of NO Oxidation and NO_x Storage on Pt/Al2O3 and Pt/BaO/Al2O3," Journal of Physical Chemistry B, 105(29), pp. 6895-6906, 2001.

64 Colombo, M., Koltsakis, G., Nova, I., and Tronconi, E., 2012, "Modelling the ammonia adsorption–desorption process over an Fe–zeolite catalyst for SCR automotive applications," Catal. Today, 188(1), pp. 42–52.

65 Olsson, L., Sjövall, H., and Blint, R. J., 2009, "Detailed kinetic modeling of NOx adsorption and NO oxidation over Cu-ZSM-5," Appl. Catal. B Environ., 87(3-4), pp. 200–210.

66 Blint, R. J., Gopinath, A., and Olsson, L., 2010, "A Kinetic Model for the Selective Catalytic Reduction of NO x with NH 3 over an Fe - zeolite Catalyst," (x), pp. 39–52.

67 Cavataio, G., Jen, H., Warner, J., Girard, J. et al.,"Enhanced Durability of a Cu/Zeolite Based SCR Catalyst,"*SAE Int. J. Fuels Lubr.* 1(1):477-487, 2009, doi:10.4271/2008-01-1025.

www.manaraa.com

68 Schmieg, S. and Lee, J., “Evaluation of Supplier Catalyst Formulations for the Selective Catalytic Reduction of NOx With Ammonia,” SAE Technical Paper 2005-01-3881, 2005, doi:10.4271/2005-01-3881.

69 Kwak, J. H., Tran, D., Burton, S. D., Szanyi, J., Lee, J. H., and Peden, C. H. F., 2012, “Effects of hydrothermal aging on NH3-SCR reaction over Cu/zeolites,” J. Catal., 287(3), pp. 203–209.

70 Zhdanov, V.P., “Elementary Physicochemical Processes on Solid Surfaces”, plenum press, New York, 1991

71 Olsson L., and Andersson B., “Kinetics modeling in automotive catalysis,” Topics in Catalysis, 28(1-4), pp. 89-98, 2004.

72 Kwon H. J., Baik J. H., Kwon Y. T., Nam I.-sik, and Oh S. H., “Detailed reaction kinetics over commercial three-way catalysts,” Chemical Engineering Science, 62(2), pp. 5042 - 5047, 2007.

73 Kwon H. J., Baik J. H., Kang S. B., Nam I.-sik, and Yoon B. J., “Simulation of a Nonisothermal Modern Three-Way Catalyst Converter,” Industrial & Engineering Chemistry Research, 49, pp. 7039-7051, 2010.

74 Larson R. S., Pihl J. A., Chakravarthy V. K., Toops T. J., and Daw C. S., “Microkinetic modeling of lean NO_x trap chemistry under reducing conditions,” Catalysis Today, 136, pp. 104-120,2008.

75 Lindholm A., Currier N. W., Li J., Yezerets A., and Olsson L., “Detailed kinetic modeling of NO_x storage and reduction with hydrogen as the reducing agent and in the presence of CO_2 and H_2O over a Pt/Ba/Al catalyst,” Journal of Catalysis, 258, pp. 273-288, 2008.

76 Xu J., Harold M. P., and Balakotaiah V., “Microkinetic modeling of steady-state $NO/H_2/O_2$ on $Pt/BaO/Al_2O_3$ NO_x storage and reduction monolith catalysts,” Applied Catalysis B : Environmental, 89, pp. 73-86, 2009.

77 Olsson, L., Sjövall, H., and Blint, R. J., 2008, “A kinetic model for ammonia selective catalytic reduction over Cu-ZSM-5,” Appl. Catal. B Environ., 81(3-4), pp. 203–217.

78 Olsson, L., Fridell, E., Skoglundh, M., and Andersson, B., 2002, “Mean field modelling of NO x storage on Pt / BaO / Al 2 O 3,” 73(x), pp. 263–270.

79 Konstandopoulos, A. and Johnson, J., "Wall-Flow Diesel Particulate Filters—Their Pressure Drop and Collection Efficiency," SAE Technical Paper 890405, 1989, doi:10.4271/890405.

www.manaraa.com

80 Konstandopoulos, A., Kostoglou, M., Skaperdas, E., Papaioannou, E. et al., "Fundamental Studies of Diesel Particulate Filters: Transient Loading, Regeneration and Aging," SAE Technical Paper 2000-01-1016, 2000, doi:10.4271/2000-01-1016

81 Konstandopoulos A. G., Kostoglou M., and Vlachos N. , "The multiscale nature of diesel particulate filter simulation," International Journal of Vechicle Design, 41, pp. 256-284, 2006.

82 Zhan, R., Huang, Y., and Khair, M., "Methodologies to Control DPF Uncontrolled Regenerations," SAE Technical Paper 2006-01-1090, 2006, doi:10.4271/2006-01-1090.

83 Gong, J. and Rutland, C., "Study the DPF Regeneration at Transient Operating Conditions Using Integrated System-Level Model," SAE Technical Paper 2010-01-0892, 2010, doi:10.4271/2010-01-0892.

84 Gong, J. and Rutland, C., "Pulsed Regeneration for DPF Aftertreatment Devices," SAE Technical Paper 2011-24-0182, 10th International Conference on Engines & Vehicles ICE2011, Sept.11-15, Naples, Italy.

85 England, S., Rutland, C., Foster, D., and He, Y., "Investigation of the Effect of DPF Loading and Passive Regeneration on Engine Performance and Emissions Using an Integrated System Simulation," SAE Technical Paper 2006-01-0263, 2006, doi:10.4271/2006-01-0263.

86 Singh, N., Rutland, C., Foster, D., Narayanaswamy, K. et al., "Investigation into Different DPF Regeneration Strategies Based on Fuel Economy Using Integrated System Simulation," SAE Technical Paper 2009-01-1275, 2009, doi:10.4271/2009-01-1275.

87 Lee, K., Seong, H., Sakai, S., Hageman, M. et al., "Detailed Morphological Properties of Nanoparticles from Gasoline Direct Injection Engine Combustion of Ethanol Blends," SAE Technical Paper 2013-24-0185, 2013, doi:10.4271/2013-24-0185.

88 Storey, J., Barone, T., Norman, K., and Lewis, S., "Ethanol Blend Effects On Direct Injection Spark-Ignition Gasoline Vehicle Particulate Matter Emissions," SAE Int. J. Fuels Lubr. 3(2):650-659, 2010, doi:10.4271/2010-01-2129.

89 Gaddam, C.K., and Vander Wal, R.L., “Emissions from Ethanol-Gasoline Blends: Physical & Chemical Characterization of SIDI Particulates,” 2012 DOE Crosscut Workshop on Lean Emissions Reduction Simulation (CLEERS), Dearborn (MI, USA).

www.manaraa.com

90 Kokjohn, S.L., Hanson, R.M., Splitter, D.A., and Reitz, R.D., "Experiments and Modeling of Dual Fuel HCCI and PCCI Combustion Using In-Cylinder Fuel Blending," SAE Int. J. Engines, 2(2):24-39, 2009.

91 Prikhodko, V., Curran, S., Barone, T., Lewis, S. et al., "Emission Characteristics of a Diesel Engine Operating with In-Cylinder Gasoline and Diesel Fuel Blending," SAE Int. J. Fuels Lubr. 3(2):946-955, 2010, doi:10.4271/2010-01-2266.

92 Richter, J., Klingmann, R., Spiess, S. and Wong, K., "Application of Catalyzed Gasoline Particulate Filters to GDI Vehicles," SAE Int. J. Engines 5(3):2012, doi:10.4271/2012-01-1244

93 Chan, T., Meloche, E., Kubsh, J., Rosenblatt, D. et al., "Evaluation of a Gasoline Particulate Filter to Reduce Particle Emissions from a Gasoline Direct Injection Vehicle," SAE Int. J. Fuels Lubr. 5(3):1277-1290, 2012, doi:10.4271/2012-01-1727.

94 Shimoda, T., Ito, Y., Saito, C., Nakatani, T. et al., "Potential of a Low Pressure Drop Filter Concept for Direct Injection Gasoline Engines to Reduce Particulate Number Emission," SAE Technical Paper 2012-01-1241, 2012, doi:10.4271/2012-01-1241

95 Rubino, L., Crane, R., Shrimpton, J., and Arcoumanis, C., "Experimental Evaluation of a Wall-Flow Filter for Gasoline Engine Particulate Emission Control," SAE Technical Paper 2001-24-0072, 2001, doi:10.4271/2001-24-0072.

96 Saito, C., Nakatani, T., Miyairi, Y., Yuuki, K. et al., "New Particulate Filter Concept to Reduce Particle Number Emissions," SAE Technical Paper 2011-01-0814, 2011, doi:10.4271/2011-01-0814.

97 Chan, T., Meloche, E., Kubsh, J., Brezny, R. et al., "Impact of Ambient Temperature on Gaseous and Particle Emissions from a Direct Injection Gasoline Vehicle and its Implications on Particle Filtration," SAE Int. J. Fuels Lubr. 6(2):2013, doi:10.4271/2013-01-0527.

98 Matteson, M. J. and. Orr, C., “Filtration: Principles and Practices,” second edition, Marcel Dekker, New York, 1987

99 Kuwabara S., “The Forces Experienced by Randomly Distributed Parallel Circular Cylinders or Spheres in a Viscous Flow at Small Reynolds Number,” Journal of The Physical Society of Japan, 14(4), pp. 527-532,1959.

100 Happel J., “Viscous Flow Relative to Arrays of Cylinders,” AIChE Journal, 5(2), pp. 174-177, 1959.

www.manaraa.com

101 Friedlander, S. K. (1957). Mass and heat transfer to single spheres and cylinders at low Reynolds numbers. *AIChE Journal*, *3*(1), 43–48. doi:10.1002/aic.690030109

102 Lee K. W., and Gieseke J. A., "Collection of aerosol particles by packed beds," Environmental Science & Technology, 13(4), pp. 466-470, 1979

103 Konstandopoulos, A. and Johnson, J., "Wall-Flow Diesel Particulate Filters—Their Pressure Drop and Collection Efficiency," SAE Technical Paper 890405, 1989, doi:10.4271/890405.

104 Konstandopoulos A. G., "Fundamental Studies of Diesel Particulate Filters : Transient Loading , Regeneration and Aging," SAE Paper No. 2000-01-1016, 2000

105 Kato, H., Ito, K., Suda, H., Kusaka, J., Mori, T., Tsurumi, F., Masaki, N., Hirata, K., and Akagawa, H. Development of a Quasi-Two-Dimensional Model for Analysing Continuous Regeneration—Diesel Particulate Filter States during Continuous and Active Regeneration. *Int. J. Engine Res. 12*, 1–13, 2011.

106 Rajagopalan, R.; Tien, C. Trajectory Analysis of Deep-Bed Filtration with the Sphere-in-Cell Porous Media Model. 1976, *22*, 523–533.

107 Tufenkji, N.; Elimelech, M. Correlation Equation for Predicting Single-Collector Efficiency in Physicochemical Filtration in Saturated Porous Media. *Environ. Sci. Technol.* 2004, *38*, 529–536.

108 Filippova O., and Hanel D., "Lattice-Boltzmann simulation of gas-particle flow in filters," Computers & Fluids Vol., 26(7), pp. 697-712, 1997.

109 Dillon, H., Stewart, M., Maupin, G., Gallant, T. et al., "Optimizing the Advanced Ceramic Material for Diesel Particulate Filter Applications," SAE Technical Paper 2007-01-1124, 2007, doi:10.4271/2007-01-1124.

110 Hayashi H., and Kubo S., "Computer simulation study on filtration of soot particles in diesel particulate filter," Computers and Mathematics with Applications, 55, pp. 1450-1460, 2008.

111 Long, W.; Hilpert, M. A Correlation for the Collector Efficiency of Brownian Particles in Clean-Bed Filtration in Sphere Packings by a Lattice-Boltzmann Method. *Environ. Sci. Technol.* 2009, *43*, 4419–4424.

112 Long, W.; Huang, H.; Serlemitsos, J.; Liu, E.; Reed, A. H.; Hilpert, M. Pore-Scale Study of the Collector Efficiency of Nanoparticles in Packings of Nonspherical Collectors. *Colloids Surfaces A Physicochem. Eng. Asp.* 2010, *358*, 163–171.

www.manaraa.com

113 Gong, J. and Rutland, C., *"Filtration Characteristics of Fuel Neutral Particulates Using a Heterogeneous Multi-scale Filtration (HMF) Model"*, submitted to ASME 2014 Internal Combustion Engine Division Fall Technical Conference, Columbus, Indiana, USA

114 Kim C. S., Bao L., Okuyama K., Shimada M., and Niinuma H., "Filtration efficiency of a fibrous filter for nanoparticles," Journal of Nanoparticle Research, 8(2), pp. 215-221,2006.

115 Wang H.-C., and Kasper G., "Filtration efficiency of nanometer-size aerosol particles," J. Aerosol Sci, 22(1), pp. 31-41,1991.

116 Davies, C. N., "Air Filtration", Academic Press, London, 1973

117 Kapparos, D., Brahma, I., Strzelec, A., Rutland, C. et al., "Integration of Diesel Engine, Exhaust System, Engine Emissions and Aftertreatment Device Models," SAE Technical Paper 2005-01-0947, 2005, doi:10.4271/2005-01-0947.

118 Brahma, I., Rutland, C., Foster, D., and He, Y., "A New Approach to System Level Soot Modeling," SAE Technical Paper 2005-01-1122, 2005, doi:10.4271/2005-01-1122.

119 Bagal, N., Rutland, C., Foster, D., Narayanaswamy, K. et al., "CO Emission Model for an Integrated Diesel Engine, Emissions, and Exhaust Aftertreatment System Level Model," SAE Int. J. Engines 2(1):1460-1472, 2009, doi:10.4271/2009-01-1511

120 Ramanathan K. and Sharma C. S., "Kinetic Parameters Estimation for Three Way Catalyst Modeling", Industrial & Engineering Chemistry Research, 50 (17), p. 9960:9979, 2011.

121 Incropera, F. P., Lavine, A. S., & DeWitt, D. P. (2011). Fundamentals of heat and mass transfer. John Wiley & Sons.

122 Keenan, M. and Thomson, J., "The Challenges of Meeting Future Emissions Legislation with a Novel Low Precious Metal TWC," SAE Technical Paper 2004-01-2984, 2004, doi:10.4271/2004-01-2984.

123 Parks, J., Prikhodko, V., Partridge, W., Choi, J. et al., "Lean Gasoline Engine Reductant Chemistry During Lean NOx Trap Regeneration," SAE Int. J. Fuels Lubr. 3(2):956-962, 2010, doi:10.4271/2010-01-2267

124 Partridge, W., Storey, J., Lewis, S., Smithwick, R. et al., "Time-Resolved Measurements of Emission Transients By Mass Spectrometry," SAE Technical Paper 2000-01-2952, 2000, doi:10.4271/2000-01-2952.

125 Olsson, L., Blint, R. J., and Fridell, E., 2005, "Global Kinetic Model for Lean NOx Traps," Ind. Eng. Chem. Res., 44(x), pp. 3021–3032.

www.manaraa.com

126 Olsson, L., Monroe, D., and Blint, R. J., 2006, "Global Kinetic Modelling of a Supplier Barium- and Potassium-Containing Lean NO x Trap," Ind. Eng. Chem. Res., 45(26), pp. 8883–8890.

127 Ramanathan, K., Sharma, C. S., & Kim, C. H. (2012). Global Kinetics for Ammonia Formation and Oxidation Reactions in a Commercial Three-Way Catalyst. *Industrial & Engineering Chemistry Research*, *51*(3), 1198-1208.

128 Holder, R., Bollig, M., Anderson, D. R., & Hochmuth, J. K. (2006). A discussion on transport phenomena and three-way kinetics of monolithic converters.*Chemical engineering science*, *61*(24), 8010-8027.

129 Gong, J. and Rutland, C., "Three Way Catalyst Modeling with Ammonia and Nitrous Oxide Kinetics for a Lean Burn Spark Ignition Direct Injection (SIDI) Gasoline Engine," SAE Technical Paper 2013-01-1572, 2013

130 Schmieg, S. J., Oh, S. H., Kim, C. H., Brown, D. B., Lee, J. H., Peden, C. H. F., and Kim, D. H., 2012, "Thermal durability of Cu-CHA NH3-SCR catalysts for diesel NOx reduction," Catal. Today, 184(1), pp. 252–261.

131 Wang, T. J., Baek, S. W., Kwon, H. J., Kim, Y. J., Nam, I.-S., Cha, M.-S., and Yeo, G. K., 2011, "Kinetic Parameter Estimation of a Commercial Fe-Zeolite SCR," Ind. Eng. Chem. Res., 50(5), pp. 2850–2864.

132 Tronconi, E., Nova, I., Ciardelli, C., Chatterjee, D., Bandl-Konrad, B., and Burkhardt, T., 2005, "Modelling of an SCR catalytic converter for diesel exhaust after treatment: Dynamic effects at low temperature," Catal. Today, 105(3-4), pp. 529–536.

133 Malmberg, S., Votsmeier, M., Gieshoff, J., Söger, N., Mußmann, L., Schuler, A., & Drochner, A, (2007). "Dynamic phenomena of SCR-catalysts containing Fe-exchanged zeolites–experiments and computer simulations", *Topics in Catalysis*, *42*(1), 33-36.

134 Pant, A., & Schmieg, S. J. (2011). Kinetic Model of NOx SCR Using Urea on Commercial Cu− Zeolite Catalyst. *Industrial & Engineering Chemistry Research*, *50*(9), 5490-5498.

135 Sjövall, H., Fridell, E., Blint, R. J., & Olsson, L. (2007), "Identification of adsorbed species on Cu-ZSM-5 under NH3 SCR conditions", *Topics in Catalysis*, *42*(1-4), 113-117.

136 Wilken, N., Kamasamudram, K., Currier, N. W., Li, J., Yezerets, A., and Olsson, L., 2010, "Heat of adsorption for NH3, NO2 and NO on Cu-Beta zeolite using microcalorimeter for NH3 SCR applications," Catal. Today, **151**(3-4), pp. 237–243.

www.manaraa.com

137 Sonia Marre, John Palmeri, André Larbot, Marielle Bertrand, “Modeling of submicrometer aerosol penetration through sintered granular membrane filters”, Journal of Colloid and Interface Science, Volume 274, Issue 1, Pages 167-182, 2004

138 Mark Stewart, “Fuel Neutral Particulates FY13 Planning Discussion”, CLEERS Tele-conf, September 12,2012

139 Ohara, E., Mizuno, Y., Miyairi, Y., Mizutani, T. et al., "Filtration Behavior of Diesel Particulate Filters (1)," SAE Technical Paper 2007-01-0921, 2007.

140 Viswanathan, S., Sakai, S., and Rothamer, D., "Design & Evaluation of an Exhaust Filtration Analysis (EFA) System," SAE Technical Paper 2014-01-1558, 2014, doi:10.4271/2014-01-1558.

141 Bissett, E. J., “Mathematical model of the thermal regeneration of a wall-flow monolith diesel particulate filter,” Chem. Eng. Sci., 39(7/8), pp. 1233–1244,1984.

142 Opris, C. and Johnson, J., "A 2-D Computational Model Describing the Flow and Filtration Characteristics of a Ceramic Diesel Particulate Trap," SAE Technical Paper 980545, 1998, doi:10.4271/980545.

143 Kato H., Ito K., Suda H., Kusaka J., Mori T., Tsurumi F., Masaki N., Hirata K., and Akagawa H., “Development of a Quasi-Two-Dimensional Model for Analysing Continuous Regeneration—Diesel Particulate Filter States during Continuous and Active Regeneration,” International Journal of Engine Research, 12(1), pp. 1-13, 2011.

144 Hwang, G. J., Cheng, Y. C., Ng, M. L., “Developing laminar flow and heat transfer in a square duce with one-walled injection and suction”, Int. J. Heat Mass Transfer 36,2429-2440, 1993

145 Huynh, C., Johnson, J., Yang, S., Bagley, S. et al., "A One-Dimensional Computational Model for Studying the Filtration and Regeneration Characteristics of a Catalyzed Wall-Flow Diesel Particulate Filter," SAE Technical Paper 2003-01-0841, 2003, doi:10.4271/2003-01-0841.

146 Giesche, H., 2006, “Mercury Porosimetry: A General (Practical) Overview,” Part. Part. Syst. Charact., 23(1), pp. 9–19.

147 Wirojsakunchai, E., Kolodziej, C., Yapaulo, R., and Foster, D., "Development of the Diesel Exhaust Filtration Analysis System (DEFA)," *SAE Int. J. Fuels Lubr.* 1(1):265-273, 2009, doi:10.4271/2008-01-0486.

www.manaraa.com

148 Merkel, G., Beall, D., Hickman, D., and Vernacotola, M., "Effects of Microstructure and Cell Geometry on Performance of Cordierite Diesel Particulate Filters," SAE Technical Paper 2001-01-0193, 2001, doi:10.4271/2001-01-0193.

149 Fukushima, S., Ohno, K., Vlachos, N., and Konstandopoulos, A., "New Approach for Pore Structure and Filtration Efficiency Characterization," SAE Technical Paper 2007-01-1918, 2007, doi:10.4271/2007-01-1918

150 Mizuno, Y., Miyairi, Y., Katsube, F., Ohara, E. et al., "Study on Wall Pore Structure for Next Generation Diesel Particulate Filter," SAE Technical Paper 2008-01-0618, 2008, doi:10.4271/2008-01-0618.

151 Ogyu, K., Ogasawara, T., Sato, H., Yamada, K. et al., "Development of High Porosity SiC-DPF Which is Compatible with High Robustness and Catalyst Coating Capability for SCR Coated DPF Application," SAE Technical Paper 2013-01-0840, 2013, doi:10.4271/2013-01-0840

152 Personal communication with Dr. Tim Johnson at Corning and Prof. David Rothamer at University of Wisconsin-Madison

153 Skjetne, E.; Auriault, J. L. New Insights on Steady, Non-Linear Flow in Porous Media. *Eur. J. Mech. - B/Fluids* 1999, *18*, 131–145.

154 Lee, S. L.; Yang, J. H. Modeling of Darcy-Forchheimer Drag for Fluid Flow Across a Bank of Circular Cylinders. *Int. J. Heat Mass Transf.* 1997, *40*, 3149–3155.

155 Tandon, P., Heibel, A., Whitmore, J., Kekre, N., and Chithapragada, K. (2010) Measurement and prediction of filtration efficiency evolution of soot loaded diesel particulate filters. *Chem. Eng. Sci. 65*, 4751–4760.

156 Lee K. W., and Gieseke J. A., "Note on the approximation of interceptional collection efficiencies," Journal of Aerosol Science, 11, pp. 335-341,1980

157 Ted D'Ottavio & Simon L. Goren (1982): Aerosol Capture in Granular Beds in the Impaction Dominated Regime, Aerosol Science and Technology, 2:2, 91-108

158 Gal, E., Tardos, G., & Pfeffer, R. (1985). A study of inertial effects in granular bed filtration. *AIChE Journal*, *31*(7), 1093–1104. doi:10.1002/aic.690310707

159 Yoshio Otani, Chikao Kanaoka & Hitoshi Emi (1989): Experimental Study of Aerosol Filtration by the Granular Bed Over a Wide Range of Reynolds Numbers, Aerosol Science and Technology, 10:3, 463-474

www.manaraa.com

160 Spielman L. A., “Particle capture from low-speed laminar flows,” Annual. Rev. Fluid Mech, 9, pp. 297-319,1977.

161 Liati, A., and Dimopoulos Eggenschwiler, P., 2010, “Characterization of particulate matter deposited in diesel particulate filters: Visual and analytical approach in macro-, micro- and nano-scales,” Combust. Flame, 157(9), pp. 1658–1670.

162 Sonia Marre, John Palmeri, André Larbot, Marielle Bertrand, “Modeling of submicrometer aerosol penetration through sintered granular membrane filters”, Journal of Colloid and Interface Science, Volume 274, Issue 1, Pages 167-182, 2004

163 Ohara, E., Mizuno, Y., Miyairi, Y., Mizutani, T. et al., "Filtration Behavior of Diesel Particulate Filters (1)," SAE Technical Paper 2007-01-0921, 2007.

164 Mark Stewart, “Fuel Neutral Particulates FY13 Planning Discussion”, CLEERS Tele-conf, September 12,2012

Davies, C. N., “Air Filtration”, Academic Press, London, 1973

165 Dillon, H., Stewart, M., Maupin, G., Gallant, T. et al., "Optimizing the Advanced Ceramic Material for Diesel Particulate Filter Applications," SAE Technical Paper 2007-01-1124, 2007, doi:10.4271/2007-01-1124.

166 Mark Stewart, “Fuel Neutral Particulates FY13 Planning Discussion”, CLEERS Tele-conf, September 12,2012

167 Karin, P., Cui, L., Rubio, P., Tsuruta, T. et al., "Microscopic Visualization of PM Trapping and Regeneration in Micro-Structural Pores of a DPF Wall," SAE Int. J. Fuels Lubr. 2(1):661-669, 2009, doi:10.4271/2009-01-1476.

168 Wirojsakunchai, E., Kolodziej, C., Yapaulo, R., and Foster, D., "Development of the Diesel Exhaust Filtration Analysis System (DEFA)," SAE Int. J. Fuels Lubr. 1(1):265-273, 2009, doi:10.4271/2008-01-0486.

169 Rakovec, N., Viswanathan, S., and Foster, D., "Micro-scale Study of DPF Permeability as a Function of PM Loading," SAE Int. J. Engines 4(1):913-921, 2011, doi:10.4271/2011-01-0815.

170 Sakai, S., Hageman, M., and Rothamer, D., "Effect of Equivalence Ratio on the Particulate Emissions from a Spark-Ignited, Direct-Injected Gasoline Engine," SAE Technical Paper 2013-01-1560, 2013, doi:10.4271/2013-01-1560.

www.manaraa.com

171 Zhang, Yizhou, Ghandhi J. and Rothamer, D., “Comparison of Particulate Size Distributions from Advanced and Conventional Combustion – Part I: CDC, HCCI, and RCCI”, SAE Technical Paper 2014-01-1296

172 Kokjohn, S.L., Hanson, R.M., Splitter, D.A., Kaddatz, J., and Reitz, R.D., "Fuel Reactivity Controlled Compression Ignition (RCCI) Combustion in Light- and Heavy-duty Engines," *SAE Int. J. Engines* 4(1):360-374, 2011

173 Viswanathan, S., Sakai, S., Hageman, M., Foster, D. E., Fansler, T., Andrie, M., and Rothamer, D., "Effect of Particle Size Distribution on the Deep-Bed Capture Efficiency of an Exhaust Particulate Filter," presented at the ASME 2014 Internal Combustion Engine Division Fall Technical Conference, October 19-22, 2014, Columbus, IN, USA.

174 Lee K. W., and Gieseke J. A., “Collection of aerosol particles by packed beds,” Environmental Science & Technology, 13(4), pp. 466-470, 1979

175 Konstandopoulos A. G., “Fundamental Studies of Diesel Particulate Filters : Transient Loading , Regeneration and Aging,” SAE Paper No. 2000-01-1016, 2000

176 Lee, K., Seong, H., Sakai, S., Hageman, M. et al., "Detailed Morphological Properties of Nanoparticles from Gasoline Direct Injection Engine Combustion of Ethanol Blends," SAE Technical Paper 2013-24-0185, 2013, doi:10.4271/2013-24-0185.

177 Storey, J., Barone, T., Norman, K., and Lewis, S., "Ethanol Blend Effects On Direct Injection Spark-Ignition Gasoline Vehicle Particulate Matter Emissions," *SAE Int. J. Fuels Lubr.* 3(2):650-659, 2010, doi:10.4271/2010-01-2129.

178 Gaddam, C.K., and Vander Wal, R.L., “Emissions from Ethanol-Gasoline Blends: Physical & Chemical Characterization of SIDI Particulates,” 2012 DOE Crosscut Workshop on Lean Emissions Reduction Simulation (CLEERS), Dearborn (MI, USA).

179 K. Park, D. B. Kittelson, and P. H. McMurry, “Structural Properties of Diesel Exhaust Particles Measured by Transmission Electron Microscopy (TEM): Relationships to Particle Mass and Mobility,” *Aerosol Sci. Technol.*, vol. 38, no. 9, pp. 881–889, Sep. 2004.

www.manaraa.com